Influence of cavitation on the dynamic response of hydrofoils

Doctoral Thesis

Presented in the Fluid Mechanics Department of the

Technical University of Catalonia

To obtain the grade of Doctor in Industrial Engineering

Presented by

Oscar de la Torre Rodríguez

Under the Direction of

Dr. Eng. Francesc Xavier Escaler Puigoriol

Barcelona, January 2013

A los bambinos, por no desfallecer…o casi

Acknowledgements/Agradecimientos

Quiero aprovechar estas líneas para expresar mi gratitud a todos los que de una forma u otra han contribuido a la realización de esta tesis, sois muchos y espero no dejarme a nadie:

Mi más sincero agradecimiento y admiración a mi director de tesis, Xavier Escaler. El trabajo diario y el modo de llevarlo a cabo han sido básicos para que la presente tesis vea la luz. Es nuestra primera tesis, cada uno en su rol, y no parece haber salido tan mal…

I want to express my sincere gratitude to Dr. Mohamed Farhat for letting me use the LMH facilities and for doing all that he could- and way beyond it- to ease my stages in Lausanne.

To all the reviewers and colleagues who read the thesis: Prof. Young, Prof. Torbjørn K. Nielsen, Dr. Liang Quanwei, Dr. Alfredo Guardo, Dr. Cristian Rodríguez, Dr. Morten Kjeldsen, Dr.Roberto Castilla and Dr. Miquel Casafont . Thank you for your comments and suggestions to improve the quality of this work.

A todos los miembros del CDIF, Eduard, Paloma, Esteve, Carme y Alex, por cuatro años de trabajo muy entretenido. A David, mi compi de despacho, por compartir sesiones musicales sin queja alguna, merci.

A mi editora, María, por el formato final del libro y aguantarme las sugerencias fuera de plazo.

Al Col·legi d'Enginyers Industrials de Catalunya por la ayuda aportada para la realización de este doctorado.

A la tropa: Gon, Agua, Luis, Alex, Buddy, Chechi, Hector, Marçal, Colli, Edu, Osito y Artus, por aguantarme durante cuatro años con el Cobayatron. Si de aquí sale algo, seréis los primeros en enteraros.

A mis anfitriones lausaneses, Cesar, Xavi, Luis y Rafa. Gracias por tener un colchón siempre preparado y por vuestra compañía en la legendariamente inhóspita Suiza.

Finalmente, agradecer a mi gente, Bambinos, Mon, Judit, Aina y familia en general. Ha costado pero ya se acabó, sentíos participes.

Abstract

The dynamic response of any structure submerged in water is significantly modified by the effect of added mass. The inertia of the fluid that the body must accelerate during its vibrational motion decreases its natural frequencies. This frequency shift between the air and still water conditions must be taken into account during the design phase to foresee any resonance problems.

However, if cavitation takes place, which is a rather common phenomenon when dealing with submerged systems or machinery, the variability in the structural response remains unknown.

This thesis presents an experimental study of the influence of sheet cavitation and supercavitation on the added mass effects experienced by a 2-D NACA0009 hydrofoil. A High Speed Cavitation Tunnel was used to generate and control the cavitation, and an innovative non-intrusive excitation and measuring system based on piezoelectric patches mounted on the hydrofoil surface was used to determine the natural frequencies of the fluid-structure system. The appropriate hydrodynamic conditions were selected to generate a range of stable partial cavities of various sizes and to minimize the effects of other sources of flow-induced noise and vibrations. The main tests were performed for different sigma values under a constant flow velocity of 14 m/s and for incidence angles of both 1° and 2°.

Additionally, a series of complementary experiments and numerical simulations were performed to assure the validity of the results and to clearly separate the effects of cavitation from other factors that may also affect the hydrofoil's natural frequencies. In this context, mode shape visualization was performed under different flow conditions to

guarantee the equivalence among the tests. In addition, the effects of the lateral wall in the test section and the pressure distribution over the hydrofoil surface were also studied.

The obtained results indicate that the maximum added mass effect occurs under conditions of still water. When cavitation occurs, the added mass decreases as the cavity length is increased. Consequently, the added mass reaches a minimum under supercavitation conditions. This behavior is well characterized by the linear correlation found between the added mass coefficient and the entrained mass of fluid that accounts for the mean density of the cavity, its dimensions and its location relative to the specific mode shape deformation.

Contents

Nomenclature

f- Frequency

f_1- First bending natural frequency; First bending mode shape

f_2- First torsion natural frequency; First torsion mode shape

f_3- Second bending natural frequency; Second bending mode shape

t- Time

a- Length; Generic coefficient

b- Span; Generic coefficient

T- Period

A- Maximum amplitude; Cross sectional area; Constant

A_{fluid} - Added mass

B_{fluid}- Added damping

n- Integer

D- Characteristic lenght

M- Mass matrix

m- Mass; Integer

K- Stiffness matrix

k- Stiffness; Integer; Increase frequency factor

C- Damping matrix; Coefficient

c- Coefficient of viscous damping: chord; sonic velocity

F- Force

C_M - Added mass coefficient

E- Young's modulus

I- Moment of inertia; Intensity

y- Displacement; Volume

$\dot{y}$-Lineal velocity

$\ddot{y}$- Lineal acceleration

L- Length; Length of signal

l- Length; Longitudinal dimension

V(x)- Generic function

T(t)- Generic function

x- Variable; longitudinal degree of freedom

v-Velocity

C_1, C_2, C_3, C_4- General coefficients

s- Roots, longitudinal degree of freedom`; Longitudinal dimension

X_o-Amplitude of vibration

h_1, h_2- Longitudinal degree of freedom

p_V- Vapor pressure

p_∞- Infinite medium pressure

R- Bubble radius

$\dot{R}$-Interphase velocity

p_g-Partial gas pressure

p- Pressure

u- Velocity

$\mathcal{F}$-Froude number

St- Strouhal number

w- Weight

h- Longitudinal dimension

P- Pressure

Greek symbols

ρ- Density

ω_n-Natural angular frequency

ω_d- Damped angular frequency

α- Incidence angle; Void ratio

ω- Angular frequency

δ- Logarithmic decrement

λ- Wavelength; Eigenvalue

σ- Thoma coefficient or cavitation number

θ- Angular displacement

φ- Phase

ϵ- Damping ratio

$\ddot{\theta}$-Angular acceleration

ϑ-Kinematic viscosity

ν- Poisson's modulus

Subscripts

o- Initial condition

e- External; Elemental matrix

max- Maximum value

static- Static condition

n- n^{th} repetition

k- k^{th} repetition

i- i^{th} repetition; Point i

fluid- Relative to fluid domain

θ- Angular magnitude

v- Volume phase

vacuum- Vacuum condition

l- Liquid phase

p- Fluid matrix

Abbreviations

ADC- Analog Digital Converter

CAE- Computer-Aided Engineering

CFD- Computational Fluid Dynamics

CSR- Cavity Surface Ratio

DFT- Discrete Fourier Transform

EM- Entrained Mass

EPFL- Ecole Polytechnique Fédérale de Lausanne

FEM- Finite Element Method

FFT- Fast Fourier Transform

FIR-Finite Impulse Response

FSI- Fluid Structure Interaction

IEPE- Integrated Electronics Piezo Electric

JTFA- Joint Time Frequency Analysis

LDV-Laser-Doppler Vibrometer

LE- Leading edge

LMH- Laboratory of Hydraulic Machinery

NACA- National Advisory Committee for Aeronautics

PZT- Lead Zirconate Titanate

STFT- Short Time Fourier Transform

TE- Trailing edge

List of Figures

List of Tables

PART I: INTRODUCTION

In this first section, the reasons for and the scope of this work are detailed. Additionally, a complete background summary and a literature review are presented to assist the reader in contextualizing the problem.

Motivation and objective

A deep understanding of the fluid-structure interaction of submerged bodies is fundamental for the design of a large variety of systems. This problem, although not new, has undergone a recent growth in popularity due to the large number of applications for fluids. As in any engineering process, a solid knowledge of the phenomenon will lead to a more efficient and, consequently, more competitive system. However, any lack of understanding will eventually produce a limit or barrier to future development and performance.

The current general interest among structural designers lies in seeking the limits of new materials or new structural configurations that offer improved, and more suitable, qualities to create thinner, lighter and more flexible structures. At the same time, the concentration of power and the off-design operation of fluid machinery results in an increase in the hydrodynamic loads applied to these structures. This general trend leads to more frequent material fatigue or resonance failures due to undesirable vibrations.

Figure 1.1- Cavitation can take different forms and affect many structures (from Franc and Michel 2004).

With an increasing energy demand throughout the world, society is turning to water (i.e., tides, waves, vortices, etc) as a potential renewable energy solution. In this context, a large number of systems currently exist that exploit different fluid properties to produce energy, but many more are expected in the near future. However, problems may arise in the design of long-term submerged structures and machinery because their environment is much more demanding and uncertain. Additionally, because they are rather inaccessible, these systems must be even more reliable than the current examples.

Engineering development currently approaches complex problems from a global perspective. A "coupled" phenomenon is one that lies between two or more apparently unrelated disciplines; in this particular case, the two disciplines are structural dynamics and hydrodynamics. The inner nature of these phenomena makes it impossible to treat them separately; in other words, the outputs of one field can be viewed as inputs of the

other(s) and vice versa, leading the system to a solution if, and only if, an overall equilibrium is reached.

Understanding and predicting the response of a structure under any type of dynamic load has become a key factor in design. Nevertheless, this response depends significantly on its boundary conditions; a body submerged in a dense fluid exhibits different dynamic behavior than one surrounded by air due to the so-called "added mass effect". If a net flow also exists around the body, hydrodynamic cavitation can take place, which could add additional uncertainties to the system because the new boundary conditions are not fully understood.

From a structural point of view, the interest in cavitation stems from the fact that many submerged bodies suffer from this phenomenon. The mixture of liquid and vapor water phases that forms the macroscopic hydrodynamic cavities can create averaged properties that are difficult to quantify and that vary from the expected effects of pure liquid water flow. Moreover, the complex structure and morphology of such a two-phase flow enhances its scientific interest.

Therefore, the aim of the current research project is to experimentally determine the effect of cavitation on the dynamic response of a hydrofoil in a high-speed cavitation tunnel.

Background

The basic physical phenomena relevant to the current research work are presented in this section to assist the reader in understanding the procedure that has been followed. These phenomena represent the core of this entire document and also act as the starting point for building a solid understanding of what and why has been done. The background information is presented in the order of relative importance to this work. First, typical

vibrational motions are described, the dynamic response of a structure is presented for simple load cases, and the resonance condition is introduced. Additionally, the topics of modal analysis theory and practice for detection of natural frequencies are also summarized. Next, the effects of a surrounding fluid on the natural frequencies of the structure are explained, and the added mass is defined. Finally, a brief description of cavitation and its different forms within a flowing fluid are also given.

II.I- Structural dynamic response

Structural dynamics is a key component of structural analysis when dynamic loads are applied to a body. To understand several concepts important to the following chapters, a detailed review of the theory is given in this section, beginning with the kinematics of a vibrating structure and following with the dynamics. A brief description of the main concepts is summarized; for a more extensive description, please refer to Moliner (1995) and Den Hartog (1985). Additionally, Appendix A presents a detailed explanation of the case of a cantilever beam due to its similarity to our studied system.

Different types of motion can approximate the structural vibration under certain constraints. A vibration is a periodic motion or a motion that repeats itself after a determined period of time.

II.I.I- Simple harmonic motion

The simple harmonic motion is described by equation (2.1):

$$y = A \cdot \cos(\omega_n \cdot t + \varphi) \qquad (2.1)$$

where y is the displacement at time t, A is the maximum amplitude of the motion, ω_n is the angular frequency and φ is the phase.

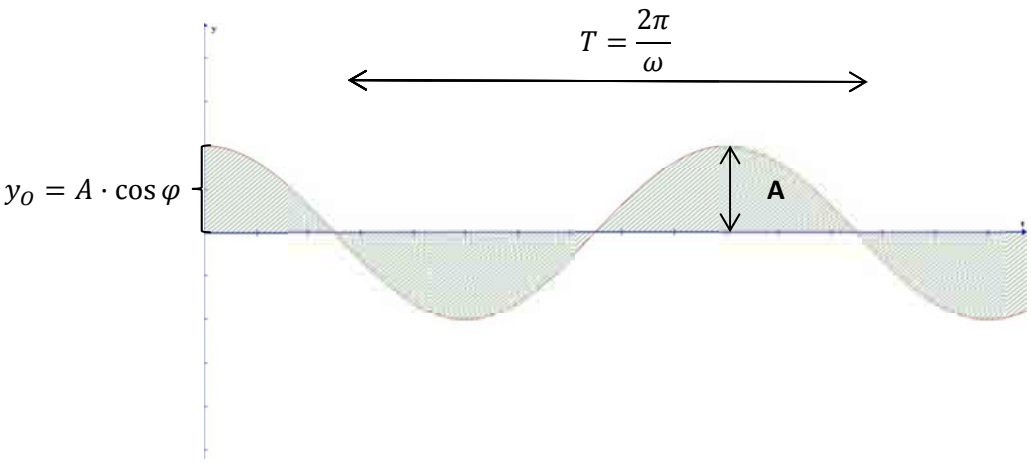

Figure 2.1- Simple harmonic motion.

The angular frequency, ω, determines the period of oscillation, T (measured in seconds). The entire motion consists of infinite repetitions of the movement of one period T (Figure 2.1). The phase (measured in radians) gives the initial angle of the motion, and the initial displacement is represented by y_O.

II.I.II- Damped simple harmonic motion

This type of motion is characterized by a continuously decreasing amplitude due to the exponential term. The general equation (2.2) is:

$$y = e^{-\epsilon\omega_n t} A\cos(\omega_d t + \varphi) \quad (2.2)$$

The damped harmonic motion is also periodic with a lower angular frequency than the undamped case, as shown in equation (2.3):

$$\omega_d = \omega_n\sqrt{1-\epsilon^2} \quad (2.3)$$

where ϵ is the damping ratio and ω_d is the damped angular frequency.

Depending of the value of the damping ratio, the motion can be classified as:

I. Overdamped ($\epsilon > 1$)

II. Critically damped ($\epsilon = 1$)

III. Underdamped ($\epsilon < 1$)

In the current document most of the systems analyzed will be underdamped. A typical profile of such motion is showed in Figure 2.2

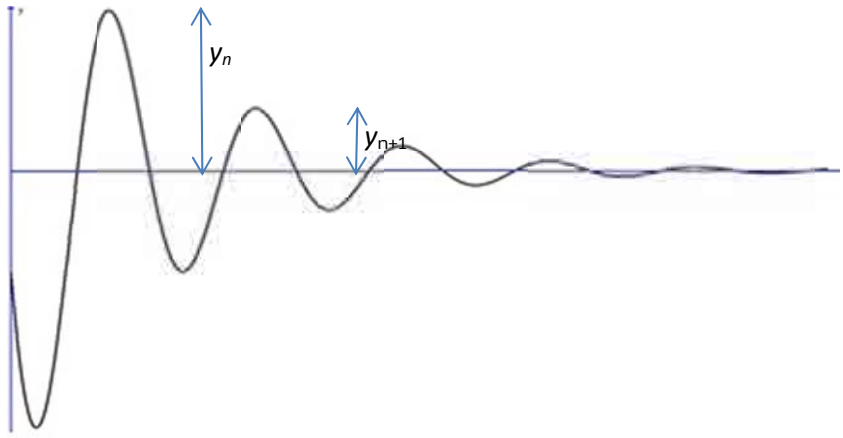

Figure 2.2- Underdamped simple harmonic motion.

where y_n and y_{n+1} are the amplitudes of two consecutive peaks.

Taking note of the logarithmic decrement, δ, the damping ratio can be used to obtain equation (2.4):

$$\delta = \ln\frac{y_n}{y_{n+1}} = \frac{2\pi\epsilon}{\sqrt{1-\epsilon^2}} \quad (2.4)$$

II.I.III- Response of a single degree of freedom system

Any mechanical or structural system whose time-dependent position can be determined by a unique coordinate is referred to as a single-degree-of-freedom system. Three different terms are required to characterize such a system. In a general form, these terms

include the mass, the spring, which determines the elastic behavior, and a damping or energy-dissipating term.

The simplest case of an undamped system with free vibration is expressed by equation (2.5):

$$m\ddot{y} + ky = 0 \quad (2.5)$$

where m is the system mass and k is the stiffness.

The general solution of equation (2.5) is given by:

$$y = y_o \cos \omega t + \frac{\dot{y}_o}{\omega} \sin \omega t \quad (2.6)$$

where y_o and $\dot{y}_o$ are the initial conditions for the displacement and velocity, and the natural angular frequency is:

$$\omega = \sqrt{\frac{k}{m}} \quad (2.7)$$

II.I.III.I- Angular vibrations

The comparison of the general case to angular displacements, which result from torsional motion, is interesting. This particular system is analogous to the linear case (equation 2.5) by taking into account that the degree-of-freedom is now an angular magnitude:

$$I\ddot{\theta} + k_\theta \theta = 0 \quad (2.8)$$

where I is the moment of inertia and k_θ is the angular stiffness, which is different from the linear stiffness, in general. Here, the angular frequency, ω_θ, is given by:

$$\omega_\theta = \sqrt{\frac{k_\theta}{I}} \quad (2.9)$$

II.I.III.II- Spring mass damper system

As previously stated, the general mechanical system contains three different components: a mass, a spring and a damper. The governing equation is expressed in equation (2.10):

$$m\ddot{y} + c\dot{y} + ky = 0 \quad (2.10)$$

where c is the coefficient of viscous damping. From this general case, the natural angular frequency of the system, ω_d, is obtained by:

$$\omega_d = \sqrt{\frac{k}{m} - \frac{c^2}{4m^2}} \quad (2.11)$$

which is analogous to equation (2.3), accounting for the damping coefficient:

$$\epsilon = \frac{c}{2m\omega_n} \quad (2.12)$$

If this system is excited by an external force (assumed to be periodic), the following differential equation of motion is applied:

$$m\ddot{y} + c\dot{y} + ky = F_o \cos(\omega_e t + \varphi_e) \quad (2.13)$$

where F_o is the amplitude of the external force, ω_e its angular frequency and φ_e is its phase. Equation (2.13) is known as the differential equation of motion of a forced single-degree-of-freedom system.

The general solution for equation (2.13) is a superposition of two different motions, i.e., a forced motion that persists as long as the external force is applied to the system and a transient motion that will die over a certain time due to the damping. Therefore, after a sufficiently long time, only the first term of equation (2.14) will drive the motion of the system.

$$y = \frac{F_o}{\sqrt{(k - m\omega^2)^2 + (c\omega)^2}} \cos(\omega t + \varphi) + e^{-\frac{c}{2m}t}(C_1 \cos(\omega_d t) + C_2 \cos(\omega_d t)) \quad (2.14)$$

where C_1 and C_2 are two general coefficients.

II.I.III.III- Resonance

For a certain external force, the amplitude of the motion and the phase depends on the frequency. In the case of an undamped system:

$$y = \frac{F}{k - m\omega^2} \quad (2.15)$$

In Figure 2.3, the resulting displacement has been plotted as a function of the frequency, ω, and it can be observed that at $\omega = \omega_n$, a response of infinite amplitude is achieved that represents the so-called "resonance phenomenon". Consequently, when the forced frequency coincides with the system's natural frequency, small amplitude forces can produce notably large motion amplitudes because the external force is applied at exactly the right direction at the right time.

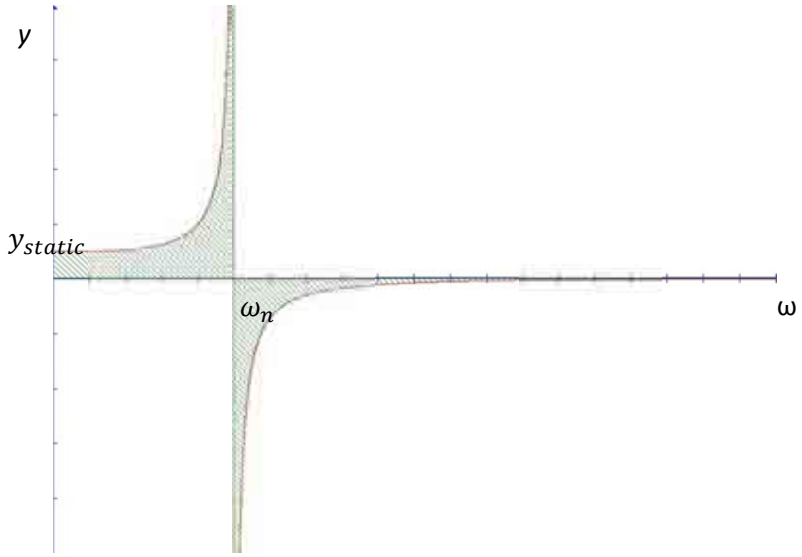

Figure 2.3 - Amplitude of displacement plotted against the external force frequency for an undamped system.

For the damped case, the displacement shown in equation (2.14) can be expressed as:

$$y = \frac{F}{\sqrt{(k - m\omega^2)^2 + (c\omega)^2}} \quad (2.16)$$

In this case, the existence of damping in the system prevents the motion from becoming infinitely amplified under resonance conditions, as observed in Figure 2.4. The maximum displacement predicted by the theory, y_{max}, can be calculated with equation (2.17).

$$y_{max} = \frac{F}{c\omega_d} \quad (2.17)$$

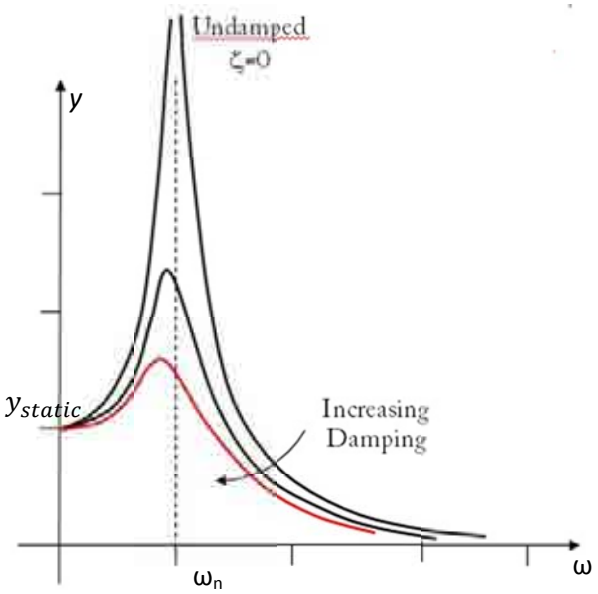

Figure 2.4 - Amplitude of displacement plotted against the external force frequency for different damping values systems.

From a practical point of view, it is necessary to anticipate the resonance conditions because they may be responsible for undesirable vibration levels and fatigue problems that may lead to system failure. In this context, modal analysis is used to study the dynamic properties of the structure under vibrational excitation and to permit identification of the natural frequencies of the system.

II.I.IV- Modal analysis

The simplification of a body into an n-degree-of-freedom system depends on the geometry of the system and the scope of the study. Nevertheless, a few structural configurations exist whose simplicity of geometry and boundary conditions allow the study of them as discrete systems. A system that requires an infinite number of degrees of freedom to fully characterize its motion because its mass, elasticity and damping are distributed along the entire system is known as a continuous system.

The modal analysis approach is frequently used to solve the dynamic properties of such systems. This analytic method is focused on systems whose motion can be expressed by means of non-homogeneous linear partial differential equations of second or higher order and that are subject to boundary and initial conditions. A two-step approach is required to solve these equations. In the first step, the non-homogeneous portion of the equation is neglected, and the homogenous portion is solved using a separation-of-variables technique. The solution consists of a set of infinite eigenvalues (λ_i) and eigenfunctions ($W_i(\bar{y})$). To proceed to the next step, it is important to note that the eigenfunctions are orthogonal and form a basis in the space. Therefore, any function can be expressed as a linear combination of the eigenfunctions. In the second step, we make use of this property and assume that the solution of the non-homogeneous equation is a linear combination of the eigenfunctions and the time-dependent generalized coordinates. Finally, these equations are solved using the initial conditions.

It is important to state that the eigenvalues of a system are related to the natural frequencies, as expressed in equation (2.18):

$$\lambda_i = \omega_i^2 \quad (2.18)$$

The eigenfunctions are also referred to as the *mode shapes,* which determine the motion of the system. In fact, each mode shape governs the motion of the entire system vibrating at a particular natural frequency.

II.II- Added mass

II.II.I- Definition

The effect of a surrounding dense fluid on the natural frequencies and mode shapes of a structure can be of paramount importance. The physical phenomenon involved in these problems is that of inertial coupling. The natural frequencies and mode shapes of a

structure within a fluid must be determined from a coupled fluid-structural analysis. Strictly speaking, these natural frequencies and modes of vibration do not originate from the structure but from the fluid-structure system. In general, the fluid inertia can be modeled as an added mass operating on the degrees of freedom of the structure. Therefore, the fluid adds no additional degrees of freedom to the system. The added mass is conservative in nature and is highly directional and sensitive to the boundary conditions.

When a structure vibrates in a dense fluid, the surface of the structure is loaded by the oscillating pressure that exists within the fluid, and at the same time, the fluid is loaded by the motion of the walls. Assuming a relatively small amplitude of vibration, the system is linear, and therefore, the pressure field is proportional to the normal acceleration of the wall.

In a general form, the added mass of a structure vibrating in a still fluid, $A_{still\ fluid}$, is essentially a function of the geometry of its surface, its position relative to the boundary conditions, the amplitude and direction of its vibration and a Reynolds-like coefficient, as shown in the following formula proposed by Blevins (1979):

$$A_{\text{still fluid}} = \rho g \left(\text{geometry}, \frac{X_o}{D}, \frac{f D^2}{\vartheta} \right) \quad (2.19)$$

where X_o is the amplitude of vibration in a given direction, D is the characteristic length, f is the frequency of vibration and ϑ is the kinematic viscosity of the fluid.

As presented in equation (2.13), the general equation of motion in matrix form for a body vibrating in a still fluid is:

$$M\ddot{X} + C\dot{X} + KX = F \quad (2.20)$$

where M, C and K are the system mass matrix, damping matrix and stiffness matrix, respectively, and F is the force applied to the body by the entrained fluid. Assuming that the fluid force takes the form:

$$F = a\,sin\,\omega t + b\,cos\,\omega t \quad (2.21)$$

then, the general equation of motion for a body vibrating in a fluid may be written as:

$$\left(M + A_{fluid}\right)\ddot{X} + \left(C + B_{fluid}\right)\dot{X} + KX = 0 \quad (2.22)$$

where A_{fluid} and B_{fluid} are the added mass and the added damping matrices, respectively. As shown in equation (2.22), the added mass is in phase with the acceleration of the structure and the added damping is in phase with the velocity.

In general, the A_{fluid} is a 6x6 matrix that relates the three rectilinear and the three angular accelerations to produce the six inertial force components of the fluid. Because the system is conservative, the added mass matrix is symmetric, and therefore, it consists of 21 unknown coefficients. Further reductions can come only from geometric symmetries, which will be explained in detail in section II.II.IV.

The natural frequency of an undamped system vibrating in vacuum conditions was expressed in equation (2.7). When submerged in a fluid, the dynamic response of a solid body is altered by the effect of the added mass of the fluid. Consequently, the ratio between the natural frequency of a given mode of vibration in water, $\mathrm{f_{fluid_i}}$, and the natural frequency in air, $\mathrm{f_{vacuum_i}}$, is approximately:

$$\frac{f_{\mathrm{fluid}_i}}{f_{\mathrm{vacuum}_i}} \cong \sqrt{\frac{1}{\left(1 + \frac{A_{\mathrm{fluid}_i}}{m_i}\right)}} \quad (2.23)$$

where i subscript denotes each particular mode shape, and m is the modal mass. Consequently, the natural frequencies of vibration are lowered with respect to those in air (considered as a vacuum). If the added mass matrix is diagonal, the system mode shapes are equivalent to those of the structure vibrating in air.

From equation (2.23), an added mass coefficient can be defined with equation (2.24). This coefficient will be of special interest throughout the present work because it can be used to quantify the added mass effects.

$$C_{M_i} = \left(\frac{f_{vacuum_i}}{f_{fluid_i}}\right)^2 - 1 \quad (2.24)$$

II.II.II- Wall effect

As previously mentioned, the added mass is highly sensitive to the boundary conditions of the fluid-structure system. One particularly interesting boundary condition is presented by a rigid wall located near the vibrating structure. In this situation, the added mass matrix can be simplified with geometric symmetries if, and only if, the symmetries are applied to both the structure under study and the solid wall.

The presence of a solid wall near a vibrating structure can cause a substantial increase in the added mass (Schiller 1971 and Yamamoto et al. 1973). In the region between the structure and the boundary, the fluid experiences an acceleration increase, which enhances the inertial forces exerted on the wetted surfaces. As the structure moves away from the boundary, the added mass rapidly decreases asymptotically to the value of an isolated body.

II.II.III- Free surface effect

Another highly important boundary is the presence of a free surface, which refers to a water-air interphase in the present work. Unfortunately, a free surface boundary confers

large calculation difficulties and behaves differently depending on the geometry of the body and its relative movement. In fact, in certain cases, a free surface enhances the added mass effect, whereas a free surface reduces the added mass effect in other cases. Free surfaces are by definition nonlinear.

Seldom do structure geometries allow us to numerically calculate the added mass value in the presence of a nearby free surface. Even in simplified situations, one can observe different behaviors in the added mass trend (Chung 1994). The effects of any boundary can usually be ignored if the boundary is located at a distance of a few characteristic lengths of the vibrating body. This length is related to the specific mode shape under study.

Another effect involving free surfaces has been commonly neglected during these added mass quantifications (Blevins 1979 and Kennard 1967). When a floating body or a submerged body vibrates near a free surface, its movement produces surface waves in the interphase. These "gravitational waves" (to distinguish them from capillary waves) and their coupling are controlled by the Froude number, defined by:

$$\mathcal{F} = \frac{\omega^2 L}{g} \qquad (2.25)$$

This issue has been of paramount importance for the naval industry for a long time (Ogilvie 1964). By means of potential flow theory, accurate approaches have been devised that can explain the train of waves produced by an oscillating body in a free surface.

II.II.IV- Plate cases

As an interesting limiting case, the added mass of plates is reviewed in this section, including a free plate immersed in a liquid with boundaries and a cantilever plate. Most of

these results are part of a more extensive list, which are shown in publications such as Blevins (1979) and Axisa and Antunes (2007).

II.II.IV.I- Cantilever plates

Several simple geometries allow the numerical calculation of the values of added mass. A large body of literature exists on this analytical approach. If we sufficiently reduce the thickness of the cantilever beam, we can consider it as a plate and calculate the added mass values for any particular mode shape of interest. Table 2.1 indicates the theoretical added mass values for the first mode shapes of a plate of length L and width c. These geometrical configurations assume an infinite fluid surrounding the unbounded structure.

Mode shape	Theoretical added mass value
First bending mode	$A_{\text{fluid}} = \frac{\pi}{4}\rho L c^2$
First torsion mode	$A_{\text{fluid}} = \frac{3}{32}\pi\rho L c^2$
Second bending mode	$A_{\text{fluid}} = \frac{\pi}{4}\rho L c^2$

Table 2.1 - Theoretical expressions for the calculation of the added mass of a cantilever beam.

II.II.IV.II- Free plates with boundaries

In this case, the plate is located at a distance h_2 from a lower fixed wall and at a distance h_1 from an upper free surface, as plotted in Figure 2.5.

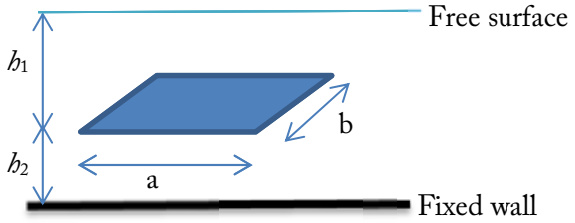

Figure 2.5 - Submerged plate surrounded by different boundary conditions.

The fluid-structure problem is split into two different domains because each of the plate faces sees a different boundary. Applying the boundary conditions and solving the coupled problem, the added mass coefficient can be obtained by equation (2.26):

$$A_{\text{fluid}}(m,n) = \frac{\rho(ab)^2\left[\tanh\left(\frac{h_1\pi\sqrt{(bn)^2+(am)^2}}{ab}\right)+\coth\left(\frac{h_2\pi\sqrt{(bn)^2+(am)^2}}{ab}\right)\right]}{4\pi\sqrt{(bn)^2+(am)^2}} \quad (2.26)$$

where m and n identify the mode shape and must be associated to the number of half-waves in each direction of the plate. Therefore, the first bending mode would be denoted as (1,1), the first torsion mode as (1,2) and the second bending mode as (2,1).

Using equation (2.26), one can examine several cases of interest. The case of a plate surrounded by an infinite fluid medium is obtained by h_1 and h_2 tending to infinity, such that equation (2.27) is obtained.

$$A_{\text{fluid}}(m,n) = \frac{\rho(ab)^2}{2\pi\sqrt{(bn)^2+(am)^2}} \quad (2.27)$$

For the opposite case, a plate surrounded by a thin layer of fluid is obtained by h_1 and h_2 tending to 0. In this particular case, the mass of the upper fluid is neglected, but the lower part becomes quite important due to a confinement effect, and the following equation (2.28) is considered:

$$A_{fluid}(m,n) = \frac{\rho(ab)^2}{4\pi^2\sqrt{(bn)^2+(am)^2}}\left(\frac{ab}{h_2}\right) \quad (2.28)$$

It is important to mention that for a plate of such dimensions, the characteristic length is expressed as:

$$L(m,n) = \frac{ab}{\pi\sqrt{(bn)^2+(am)^2}} \quad (2.29)$$

II.III- Cavitation

II.III.I- Definition

Cavitation is the appearance of vapor cavities inside an initially homogeneous liquid when the pressure is decreased to a sufficiently low value at constant temperature (Knapp et al. 1970). Therefore, this phenomenon intrinsically represents a liquid-vapor phase change, as shown in Figure 2.6.

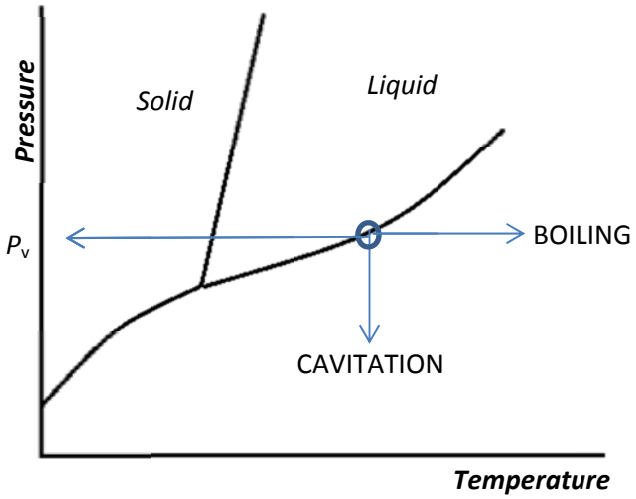

Figure 2.6 - Phase diagram in which boiling (isobaric phenomenon) and cavitation (isothermal phenomenon) are represented.

The phase diagram of Figure 2.6 introduces an important concept, "vapor pressure" (p_v). Because cavitation can be represented as an isothermal decrease of pressure, a pressure threshold may exist beneath which a vapor phase generally appears. Such a threshold, which obviously depends on the temperature of the fluid, is the "vapor pressure".

Different types of cavitation exist depending on how it is produced. In the present work, we focus on hydrodynamic cavitation, which is produced in flowing liquids by pressure variations due to the geometry of the system. Nevertheless, it is first necessary to introduce the growth of a single bubble of vapor inside a liquid due to a pressure reduction. Next, the various forms of macroscopic types of cavitation around hydrofoils will be addressed.

II.III.II- Bubble basic equations

Cavitation is inherently related to bubble dynamics. Inside the liquid, bubbles are subjected to growth and collapse processes due to the sign of the pressure variation. In

Figure 2.7, a single bubble is indicated with an internal radius, R(t), that changes with the radial velocity of its interphase, $u(r,t)$, as the infinite medium pressure is changed, $p_\infty(t)$.

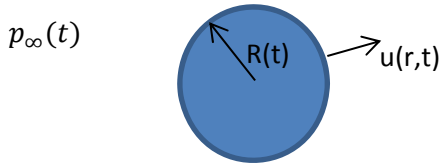

Figure 2.7- Bubble diagram.

For a Newtonian and incompressible liquid, the growth of a bubble is governed by the Rayleigh-Plesset equation (2.30).

$$\rho\left[R\ddot{R}+\frac{3}{2}\dot{R}^2\right]=p_v-p_\infty(t)+p_{g0}\left(\frac{R_0}{R}\right)^{3\gamma}-\frac{2S}{R}-4\mu\frac{\dot{R}}{R} \qquad (2.30)$$

where $\dot{R}$ is the bubble interface velocity, $\ddot{R}$ is the acceleration, p_{g0} is the initial partial gas pressure inside the bubble, γ is the ratio of the heat capacities and S is the surface tension of the liquid. This equation yields the temporal evolution of a bubble radius. The bubble collapse can be estimated by differentiating the radius expression and forcing it to 0. Pressures in thousands of bar, surface velocities close to sonic velocities and temperatures of thousands of Kelvin have been experimentally measured during this phenomenon (Dopazo 2008).

II.III.III- Hydrodynamic cavitation

In a flowing system, the liquid particles can be subjected to positive local accelerations that will lead to static pressure reductions, as stated by Bernoulli's equation (2.31), in which p_i is the particle pressure, u_i is its velocity and C is a constant value. This equation assumes that at any point *i* of the same streamline, the sum of the static term and the dynamic term are constant when the differences in the geometric head are negligible.

$$p_i + \frac{1}{2}\rho u_i^2 = C \qquad (2.31)$$

The cavitation number, σ_{THOMA} (also known as the Thoma number), is a dimensionless parameter that relates both variables (pressure and velocity) and described the flow from the cavitation point of view. In fact, the lower the cavitation number, the more prone the system is to cavitation.

$$\sigma_{THOMA} = \frac{p_i - p_v}{\frac{1}{2}\rho u^2} \qquad (2.32)$$

Hydrodynamic cavitation around hydrofoils can appear with different shapes, morphologies and behaviors. Usually, when one refers to large-scale cavitation structures, they are divided into travelling bubble cavitation, vortex cavitation and attached cavitation categories (Franc and Michel 2004).

Travelling bubble cavitation: This type of cavitation corresponds to the formation of single bubbles with their origin in solid nuclei or uncondensed microbubbles of gas that grow to a visible size when convected by the main flow. When the density of cavitation within the flow increases, these bubbles tend to merge together to form bubble cavitation (see photograph on Figure 2.8).

Figure 2.8 - Travelling bubble cavitation (from University of Tokyo).

Vortex cavitation: High vorticity flows present notably low pressures in the core of the vortexes. As a result, filaments of vapor appear in these cores and are also convected downstream by the flow. This type of cavitation usually appears inside the von Karman vortexes generated in the wake of a body, as observed in the photograph of Figure 2.9.

Figure 2.9 - Vortex cavitation (from Brennen 1995).

Attached cavitation: This cavitation type appears when a region of separated flow is filled with a macroscopic vapor structure. Consequently, the cavitation is usually attached to the suction side of a solid body, as observed in Figure 2.10. This particular type of cavitation is of paramount interest in our investigation because it provides adequate conditions under which to develop the current thesis work.

Figure 2.10 - Attached cavitation on a NACA0009 profile at the LMH.

II.III.III.I- Attached cavitation

As mentioned above, this type of cavitation is attached to solid surfaces. When dealing with submerged hydrofoils, attached cavitation also refers to sheet cavitation due to its shape. Usually, this type of cavitation detaches close to the leading edge of the profile and extends downstream as the cavitation number is lowered. The closure region produces u-shaped vortices that collapse on the surface of the structure.

There are several different methods used to classify sheet cavities. If the length of the sheet is increased (which is usually expressed by the ratio of the cavity length, *l*, to the hydrofoil chord, *c*), the behavior of the sheet tends to become unstable. This instability typically takes place for *l/c* ratios between 0.75 and 1 and is characterized by a periodical fluctuation of its length, which sheds macroscopic cavities that can turn into u-shaped vortices and collapse quite violently. This unstable cavitation is usually referred to as cloud cavitation. The unsteadiness is originated at the cavity closure region by the so-called re-entrant jet. This water jet advances upstream towards the leading edge and cuts a portion of the cavity. This process results in a type of periodic shedding process of bubble clouds that are convected by the flow to the pressure recovery region, where they collapse violently. The shedding frequency is expressed by a dimensionless parameter known as the Strouhal number and is defined by equation (2.33):

$$\mathrm{St} = \frac{fl}{u_\infty} \quad (2.33)$$

where l is the characteristic length of the cavity, u_∞ is the free stream flow velocity and f is the shedding frequency.

Another interesting distinction exists for sheet cavities that depends on the *l/c* ratio. If the cavity closure occurs on the suction side of the profile, it is referred to as "partial

cavitation". In contrast, if the closure takes place downstream of the trailing edge and therefore covers the entire suction surface of the hydrofoil, it is known as "supercavitation". Typical partial cavitation and supercavitation conditions are shown on the top and bottom photographs of Figure 2.11, respectively.

Figure 2.11 - Partial sheet cavitation (above) and supercavitation (below) on a NACA0009 profile.

In fact, this sheet is not a pure vapor phase body but a mix of liquid and gas. A biphasic structure may require an average density for characterization, and therefore, Ischii (1975) proposed a definition of the cavity mean density, $\bar{\rho}$, represented by equation (2.34):

$$\bar{\rho} = \alpha\rho_v + (1-\alpha)\rho_l \quad (2.34)$$

where ρ_l is the density of the liquid phase water, ρ_v is the density of the vapor phase water and α is a parameter known as the void ratio, which determines the sonic velocity within the cavity. It is expressed as:

$$\alpha = \frac{y_v}{y_v + y_l} \quad (2.35)$$

where y_v and y_l are the volumes of the cavity in the gas and liquid phases, respectively. There is a lack of knowledge of the internal composition of such macrocavities. Void ratios and internal cavity morphology in general have recently become important topics of research due to the impressive improvement in X-rays and endoscopes. (Stutz and Legoupil 2003 and Aeschlimann et al. 2011)

State of the art

Prediction of the dynamic behavior of a structure during its design phase is a key issue. The calculation of modal parameters such as natural frequencies and mode shapes is necessary to predict the structural response to an external dynamic load. An extensive body of academic literature addresses the topics of theoretical, experimental and computational approximations to the dynamic response of solid bodies with multiple configurations. Blevins (1979) summarized many of the most important formulas and principles used in this field.

As detailed in a preceding section, when a solid structure is partially or completely submerged in a high-density fluid, its dynamic response will differ from its response in a vacuum due to the added mass effect, which is the result of the inertia of the surrounding fluid entrained by the accelerating structure. Kirchhoff (1869) set the mathematical basis for treatment of the solid-fluid system, and Lamb (1945) used it to study the motion of one or more solids in a frictionless liquid. Patton (1965), Blevins (1979) and Kennard (1967) numerically determined the added mass coefficient of an extensive quantity of 2D and 3D solid configurations under different boundary conditions.

Due to their particular geometry (which greatly simplifies the added mass tensor), spheres and cylinders have been widely studied both theoretically and experimentally. Starting from unbounded solids, special attention has been focused on the interaction of several bodies. In this context, Jeffrey (1973) studied heat conduction through a stationary

random suspension of spheres with an original method known as the twin spherical expansion. This method inspired Van Wijngaarden (1976) to study the forces generated on a sphere by a near sphere in an impulsively accelerated fluid and to extract the added mass values for two different sphere distributions. If the sphere center plane was perpendicular to the velocity of the fluid, the added mass was increased, and if it was parallel, the added mass was reduced. Ragazzo (2002) calculated the hydrodynamic force and torque that a small amplitude/rapidly oscillating body induces on another body able to freely move in its vicinity in an ideal fluid. He stated that if the free body is located sufficiently far from the oscillating body, then the averaged interaction force is attractive if, and only if, the density of the free body is larger than the density of the fluid. The study of cylinders (which if sufficiently long can be treated as 2D bodies) allowed the development of Strip theory (Salvesen et al. 1970) for slender bodies partially or completely submerged in a fluid. With this tool, the solution to the three-dimensional problem is approximated by solving a series of two-dimensional problems in the cross-flow plane.

As previously discussed, the effect of surface waves has been commonly neglected in the currently available compilations of added mass coefficients for different body configurations (Patton 1965, Blevins 1979 and Kennard 1967). However, this particular field has been widely treated by those authors related to the navy industry, including Ursell (1948a, 1948b, 1953), Porter (1961), Frank (1967) and Kaplan and Kotik (1963). In their studies, the importance of surface waves to the added mass of bodies floating or submerged near a free surface was clearly demonstrated. These researchers together determined the importance of the vibration frequency using the Strouhal number.

Using potential flow theory, the system of a solid wall near a body has also been studied by Lamb (1945) and Milne-Thomson (1968), who modified the kinetic energy of an

unbounded sphere to take into account the energy increase produced by the wall effect. This approach, which consists of truncating an infinite polynomial series of the non-dimensional wall distance, has been widely accepted but produces great divergences when the sphere-wall gap drops to below half the radius of the sphere. For low Reynolds numbers, a new approach has been developed by Yang (2010) with significantly improved results. Recently, Motley et al. (2012) investigated the effects of surrounding boundaries on the response of cantilever composite beams by means of numerical simulation. They specifically studied the effects of the free surface in partially submerged structures as well as the effects of solid boundaries near the beam.

Most of the referenced works attempt to numerically determine the added mass coefficients with what can be considered a direct approach. Nevertheless, another approach exists to study the added mass behavior of submerged bodies. Using structural dynamics theory, one can easily observe the relationship between the added mass and the natural frequencies of submerged bodies (equation 2.48); this is what we call an indirect method. Many of the following references use this type of approach to study the added mass. A systematic and detailed study was performed by Lindholm et al. (1965) on cantilever beams in air and submerged in water. Experimental results with natural frequencies showed reasonably good agreement with plate theory approximations. Consequently, empirical correction factors were obtained for the added mass by taking into account the beam aspect and thickness ratios. Sewall et al. (1983) successfully compared experimental and analytical data related to the vibration frequency of the fundamental mode of a three-sided membrane in air. They also found that the added mass effect on a cylinder was overestimated using the same analytical method. More recently, Kimber et al. (2009) studied the interaction between two cantilever structures

vibrating in air in various configurations. They verified that the resonance frequencies and aerodynamic damping depend on the vibrating phase difference between the plates.
Furthermore, several analytical models have been also built to carefully analyze the dependency of the added mass effect on various parameters. Amabili (1996) presented a model to estimate the natural frequencies and mode shapes of partially filled shells. Conca et al. (1997) showed that the added mass matrix for a mechanical structure vibrating in an incompressible fluid does not depend on the viscosity. Yadykin et al. (2003) found that for a flexible plate oscillating in a fluid, either an increase of the order of the mode of vibration or a decrease of the aspect ratio leads to a decrease of the added mass effect.

In the field of hydraulic machinery, fluid-structure interaction (FSI) phenomena involving hydrofoils are a major concern, and several investigations have been performed on this topic. Ducoin et al. (2010a) experimentally studied the vibrations induced in a hydrofoil by the laminar to turbulent boundary layer transition and determined their significance and dependence on the vortex shedding frequency. Olofsson (1996) experimentally studied the dynamic performance of partially submerged propellers. Using numerical simulations, Moussou (2005) developed methods and solutions for two coaxial cylinders with quiescent fluid between them. Additionally, Münch et al. (2010) developed numerical simulations for an oscillating hydrofoil under incompressible turbulent flow.

The introduction of cavitation into the fluid-structure system greatly increases the complexity of the problem; however, FSI phenomena under cavitating flows have not yet been extensively studied. Previous studies have been mainly focused on analyzing the hydrofoil response. For example, Amromin and Kovinskaya (2000) analyzed the vibration of an elastic wing with an attached cavity in a perturbed flow. They found that two different frequency bands were excited: a low band associated with cavity oscillations and a high band associated with wing resonances. Numerical investigations have been also

performed on this particular topic. For example, Young (2007) performed a coupled 3D simulation to analyze the time-dependent hydroelastic response of cavitating propellers, and Young et al. (2011) compared the mechanical efficiency and the hydrodynamic and structural performance of various surface-piercing propeller designs. Finally, Ducoin et al. (2010b) presented a method to simulate FSI problems under cavitating flows.

Although several effects caused by cavitation have been extensively reviewed, such as the modification of lift and drag (Amromin et al., 2003) and the risk of cavitation erosion (Escaler et al., 2007), few references addressing experimental studies on the effect of cavitation on the added mass or the hydrofoil natural frequencies were found by the author. Recently, Ducoin et al. (2012) experimentally studied the structural response of a flexible hydrofoil under cavitating flows and provided certain remarks on its effect on the natural frequencies of a profile. Nevertheless, his work was aimed at analyzing the displacement of the structure and the vibration levels rather than examining the effect on the added mass. However, a few numerical examinations of added mass effects under cavitating flows have been reported as well, such as that of Fine et al. (2001). A work closely related to the present study was presented by Benaouicha and Astolfi (2012). This group developed an extensive theoretical study on the added mass of different body configurations under cavitating flows. In their work, the authors analytically observed that the natural frequencies should increase with the length of the cavity.

Understanding the morphology and the inner properties of cavitation is a fundamental step in this field. This research topic has recently experienced a great increase in interest due to the advances and improvements in available measuring equipment. In this context, Stutz and Reboud (1997), Stutz and Legoupil (2003), Coutier-Delgosha et al. (2006) and Aeschlimann et al. (2011) have performed experimental measurements on different types of cavitation to better characterize its inner structure.

The presence of cavitation and the associated added mass effects are relevant to applications in water turbines and pumps. Currently, only the effects of still water surrounding turbine runners have been investigated both experimentally and numerically, but these investigations have not considered the presence of cavitation on the blades (see, for example, the work of Rodriguez et al., 2006, and of Liang et al., 2007). It should be noted that the current trend of regular operation of these hydraulic machines beyond their design specifications renders them more prone to cavitation problems. It is therefore necessary to estimate their dynamic responses under such extreme conditions to reduce the damage suffered from material fatigue.

In summary, the literature addressing the dynamic response of a structure under cavitating flows is clearly insufficient for carefully study of the effects of cavitation on the added mass of a body. This work is focused on the dynamic response of a hydrofoil under cavitating flows. In this context, the present thesis aims to produce valid experimental data that can be used to characterize the FSI under such conditions. In addition, because a bounded solid is studied, the effects of different boundary conditions are also studied. In fact, this work is the logical previous step to a study of the effect of similar conditions on an entire machine model or on a more complex configuration body in which the great quantity of independent variables would make its analysis unapproachable.

Working plan

To accomplish the main objective of the present investigation, a detailed plan was constructed. The goal was to determine the influence of cavitation on the natural frequencies of a NACA0009 hydrofoil, but to reach this goal, a preliminary path was required to address the necessary stages.

To extract the natural frequencies of a structure, one usually performs a modal analysis by means of an impact test, but because the hydrofoil was intended for installation in a closed test section, an alternative excitation system was required. Consequently, the first task consisted of developing and testing a suitable excitation and measuring system for submerged structures that could be used in a test section of a high-speed cavitation tunnel.

Given that the air condition (assumed equivalent to "in vacuum") would be taken as the reference used to quantify the effects on the natural frequencies, and taking into account that there exists a slight difference between the in-vacuum and submerged-in-water mode shapes, an important complementary step was required to verify the equivalence of the mode shapes. Therefore, mode shape visualization under different flow conditions was carried out.

Because the test section is a confined space, one cannot assume that the hydrofoil is an unbounded body. In addition, the installation of the NACA0009 profile within the test section as a cantilever beam resulted in the existence of a small gap between its tip and the lateral wall, which could enhance the effect of the boundary. It was also decided to study the effects of the lateral walls on the natural frequencies of the hydrofoil to identify and separate them from the cavitation effects. In addition to the experimental tests, a numerical model was also built to further investigate this phenomenon and to understand it more deeply.

Pressure loads can vary the natural frequencies of a body by altering its stiffness, and it is well known that the pressure within a hydrodynamic macro-cavity drops to a value close to the vapor pressure at that temperature. The effect of this load change should also be

considered. Therefore, a series of tests was designed to observe the effects of pressure distribution on the natural frequencies of the hydrofoil.

As a consequence of the analysis and discussion of the main results, additional tests were required. Therefore, the natural frequencies of a partially submerged hydrofoil were experimentally and numerically investigated.

Thesis organization

The current document is organized in four parts:

The first section or "Introduction" states the motivation and main objectives of the present work and also presents the main theoretical concepts dealt with in this thesis: the structural dynamic response, added mass and cavitation. Additionally, a detailed review of the published literature on such topics is presented, and finally, the last section is devoted to a description of the working plan.

The second part, titled "Experimental set up, methodology and numerical model", describes all of the applicable experimental procedures with special attention given to the facilities required for the tests and the equipment used. The different performed tests are described, and a detailed explanation of the post-processing methods used to obtain the experimental data is presented. The last section describes the numerical simulation.

The third part, "Results and discussions", summarizes the main results of the different experiments as well as the numerical simulation performed during the present work. The last section discusses, relates and compares these results.

The thesis ends with part four, "Conclusions". This section is devoted to summarizing the main conclusions and also presenting the reasoning behind them. In this section, future research directions are also proposed.

PART II: EXPERIMENTAL SET-UP, METHODOLOGY AND NUMERICAL MODEL

Starting from an innovative excitation system and a series of preliminary tests to proof its reliability, in this part a detailed explanation of the equipment and facilities used during the experimental tests is given. Besides, a description of the tests performed and a step-by-step comment of the post processing tools used to obtain the desirable results are made. At the end of the current part, a numerical model is presented along with the platform and the physical assumptions required to simulate all the scenarios.

PZT Patches

VI.I- Specifications

Chronologically, the first but also the most important task of this work was to think, choose and proof a suitable excitation system which could be used to excite a hydrofoil installed in a cavitation tunnel and to measure its dynamic response. The main requirements it must have to fulfill are summarized in Table 6.1.

Requirements	Reasons
- Enough excitation energy	- Noisy environment, flow-induced vibrations
- Adequate frequency range excitation	- Unknown frequencies
- On board system	- Structure located inside a tunnel test section
- The flow must not be perturbed	- Flow conditions must be stable and known, cavitation cannot be affected

Table 6.1- Requirements of the ideal excitation system for an installed hydrofoil in the LMH High speed cavitation tunnel.

Plumbum (lead) Zirconate Titanate (PZT) patches were chosen as an excitation system. These patches are made of polycrystalline ceramic material with piezoelectric properties. The piezoelectric effect was discovered with quartz crystals in 1880 by Pierre and Marie Curie and refers to the electric potential that certain materials spontaneously generate when a pressure is applied to them. The inverse piezoelectric effect also occurs, in which a material changes its shape when exposed to an electric potential. Since the piezo effect exhibited by natural materials is very small, PZT with improved properties have been developed. (Figure 6.1)

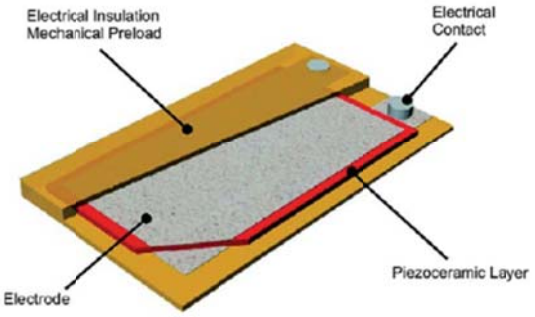

Figure 6.1- Sectional view of the conforming parts of a PI piezoelectric patch (from PI Ceramic GmbH).

Taking advantage of this duality, these patches may be used as either sensors or actuators. In excitation mode, a voltage is applied to the metallized surfaces that surround the ceramic material. The resulting electric field causes a contraction of the material perpendicular to the direction of the electric field. If glued to a solid substrate, the contraction of the patch exerts a force on the substrate through its contact surface. In sensing mode, the patches generate an electric voltage output as a response to a change in their shape.

Among all the piezoelectric materials configurations, patches were chosen because they are flexible and allow us installing them on non-flat surfaces. Also their small thickness dimension would make easier to embed them on the structure and therefore do not affect the flow. The patch model PI P-876 DuraAct was finally chosen, its main characteristics are summarized in Table 6.2.

PZT specifications	
Piezoelectric material	PIC 255
Operating voltage	-100 to +400V
Dimensions	61 x 35 x 0.5 mm
Blocking Force	265 N

Table 6.2- PI Ceramic PZT patches specifications.

Since the operating voltage is rather high and signal generators usually provides lower voltage, a signal amplifier with a gain factor of 25 was used to feed these patches.

VI.II- Preliminary tests

Different tests were performed to check PZT patches suitability to be used as an excitation system. As stated in previous sections, this technology can be used as either sensors or actuators. The following proofs were made:

a) A natural frequencies identification of a cantilever beam in air and submerged in water using a patch as an exciter.
b) A comparison between the response signals of the patch and an accelerometer.

VI.II.I- Natural frequencies identification of a cantilever beam

When used as an actuator, the patch must be able to sufficiently excite the structure to obtain measurable response signals. In this particular test, a patch was glue on the surface of a stainless steel beam which was clamped to a lateral wall of a plexiglass pool. The main objective of this test was to identify several mode shapes of the beam, bending and torsion modes. To do so, three accelerometers were installed in the positions indicated in Figure 6.3 to measure the beam response. Besides, a signal generator fed the patch

through the amplifier. By exciting a wide frequency band and measuring the response with the accelerometers, it was expected to identify the response amplification under resonance conditions. In order to excite a frequency band, a chirp signal was used. Chirps are a type of signals in which its driving frequency varies with time. The two main ones are linear and exponential chirps. In the present work, a sinusoidal linear chirp was used as it produced good results and was easier to interpret in the time domain. A linear chirp function can be expressed as:

$$f(t) = A\sin((f_0 + kt)t) \qquad (6.1)$$

Where f_0 is the frequency at time 0 and k is the increase factor in Hz/s. Figure 6.2 shows a typical sinusoidal linear chirp.

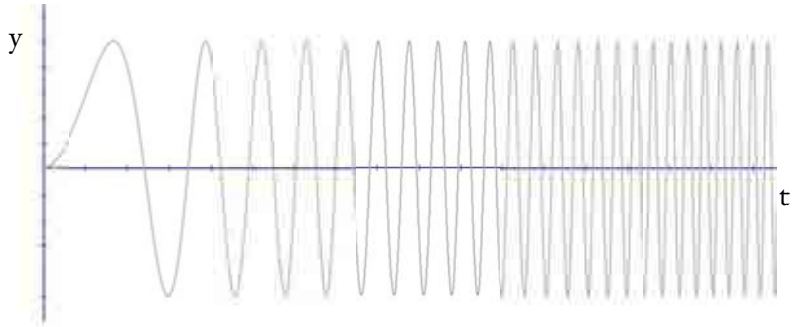

Figure 6.2- A typical linear chirp signal.

The location of the accelerometers (see Figure 6.3) helped us assigning each natural frequency to a specific mode shape; the response magnitude and phase was analyzed for each one. As a result, first and second bending mode and first torsion mode were easily identified in air. When submerged in water, the electrical connectors of the patch and the accelerometers were isolated with silicone and the test was repeated with satisfactory results.

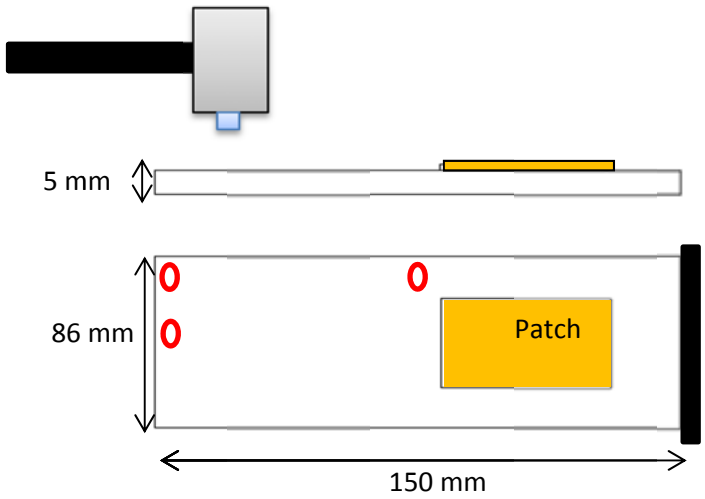

Figure 6.3- Sketch of the preliminary tests. Red circles represent the location of the accelerometers.

VI.II.II- Accelerometer and patch responses comparison

Once the patch suitability as an actuator was proved, a comparison between accelerometers and the patch responses signal was made. To do so, a conventional impact test was performed. An instrumented hammer was used to impact the structure in different positions (Figure 6.3) while the responses were acquired both with the accelerometers and the patch. As observed in Figure 6.4 where the accelerometer and the patch signals can be compared, it can be assumed that analogous results are obtained with the patch thus its validity as a sensor is also proved.

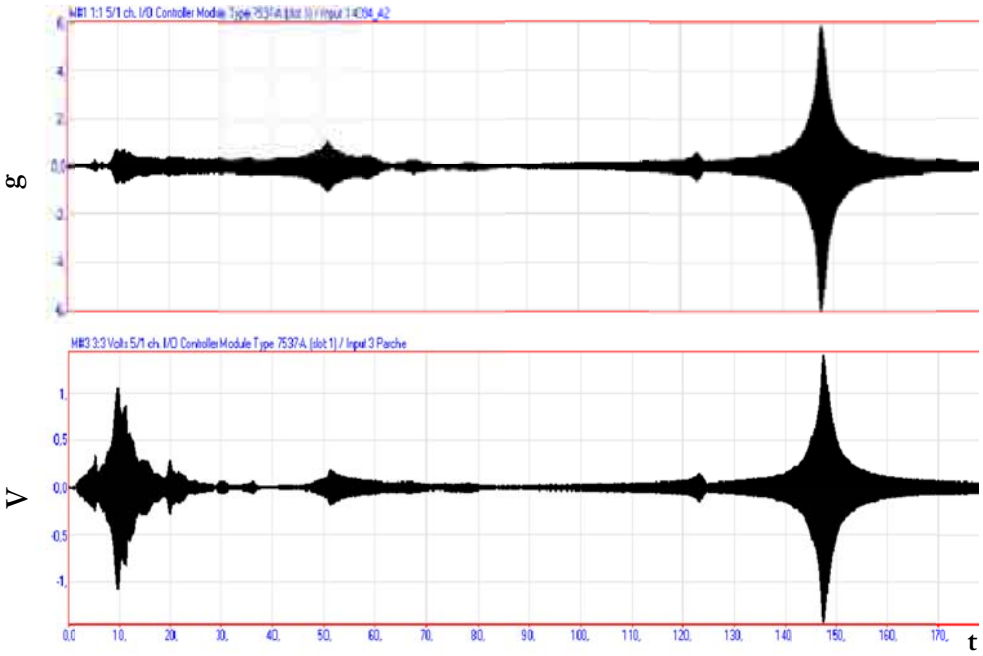

Figure 6.4- Comparison of time signals: accelerometer (above) and patch (below).

One can reach a very important conclusion with these preliminary tests. It is of capital importance to previously decide what modes of vibration one wants to excite or/and monitor to correctly locate the patch along the structure surface as they are stuck with a non-removable glue. The position of the patch can enhance or diminish the effectiveness of the excitation due to the presence of nodal lines. During these first tests, for instance, torsion modes were difficult to excite and monitor because the patch was located in the neutral axis of the beam.

On the other hand, the patch supplied enough energy to excite the beam working in the range from 0 to 125 V both in air and submerged in water. Special attention had to be given to "overload" situations as the response signals are cut by the acquisition system due to an excessive voltage input. Therefore, it is often necessary to adapt the excitation voltage level depending on the test conditions. In this case, the effects of water

surrounding the structure damped the vibration and required a higher excitation than in air.

Experimental set up

VII.I- Test facility and hydrofoil

VII.I.I- Cavitation tunnel

The main experimental tests were performed at the High Speed Cavitation Tunnel in the Laboratory for Hydraulic Machines (LMH) of the École Ploytechnique Fédérale de Lausanne (EPFL). This specific tunnel was described by Avellan et al. (1987) and it is shown in Figure 7.1. It consists of a closed loop circuit with a rectangular test section whose inner dimensions are 150 x 150 x 750 mm. In order to reduce the turbulence and the flow rotation, upstream of the test section a honeycomb, a screen and a contraction nozzle are installed.

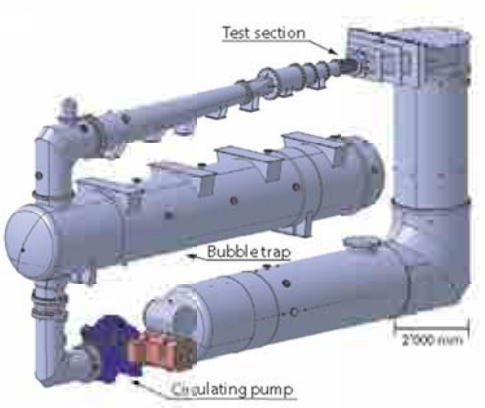

Figure 7.1-LMH High speed cavitation tunnel sketch.

The pumping system provides a total head of 36.5 m for 1.125 m^3/s at 885 rpm, which allows a maximum velocity at the test section of 50 m/s.

During the experiments the controlled flow parameters are the free stream velocity at the test section inlet, u_∞, and the cavitation number, $\sigma = \frac{(p_\infty - p_v)}{\frac{1}{2}\rho u_\infty^2}$, where p_∞ is the pressure at the test section inlet. The mean flow velocity value is derived from absolute pressure measurements at both ends of the contraction nozzle. The temperature is also measured upstream of the contraction nozzle. One can set the desired pressure by controlling the air pressure over the free surface in the pressure vessel; the maximum static pressure is 16 bar. The whole installation is controlled by a programmable automaton with a Labview user interface.

VII.I.II- Hydrofoil: NACA0009

Dynamic response of an aluminum NACA0009 profile was studied under different flow conditions. A NACA0009 shape is defined by equation (7.1) where *y* stands for half the local thickness, *x* is the local position and *c* is the chord or the profile. Besides NACA nomenclature give us additional information about the profile itself. The first two digits refer to the maximum camber and the distance to it from the leading edge. It is therefore a symmetric profile. Two last digits give us the maximum thickness as a chord percentage which, in this case, is located at 45 % of the chord. This particular hydrofoil was 100 mm chord-originally was 110 mm but the trailing edge was truncated- and spanned all the cavitation tunnel test section. The first model with the truncated trailing edge is shown in Figure 7.2.

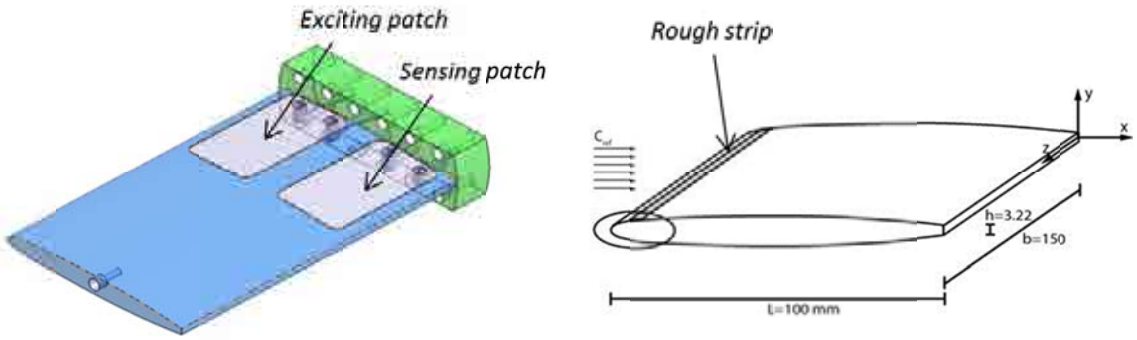

Figure 7.2- Different views of the NACA0009 profile Both PZT patches (left) and the roughness and trailing edge details (right).

The hydrofoil was finally mounted in the tunnel test section by clamping one side to a rigid subjection system as observed in Figure 7.3. Therefore, the hydrofoil resulted as a cantilever beam with a small gap (≅ 0.12 mm) between the tip section and the lateral plexiglass wall of the test section.

Figure 7.3- Hydrofoil installed on the rigid subjection system.

During preliminary test campaigns, different scenarios were tested to trigger the cavitation sheet in a definite position. At the end, an external roughness strip was placed in the leading edge of the profile suction side to obtain a more homogenous sheet along the span (see Figure 7.4). The strip consisted of a 2 mm band of sand glued next to the

stagnation point with a thickness of approximately 200 μm (see detail on the right side of Figure 7.2). During last test campaign, the trailing edge of the profile was modified to minimize flow induced vibrations. A 45° cut was mechanized as shown in Figure 7.5 and a considerable reduction of the flow induced vibration was obtained in agreement to Zobeiri (2012) results.

$$\frac{y}{c} = \begin{cases} 0.1737\left(\frac{x}{c}\right)^{1/2} - 0.2422\left(\frac{x}{c}\right) + 0.3046\left(\frac{x}{c}\right)^{2} - 0.2657\left(\frac{x}{c}\right)^{3}, & 0 \le x \le 0.5 \\ 0.0004 + 0.1737\left(1 - \frac{x}{c}\right) - 0.1898\left(1 - \frac{x}{c}\right)^{2} + 0.0387\left(1 - \frac{x}{c}\right)^{3}, & 0.5 < x \le 1 \end{cases} \quad (7.1)$$

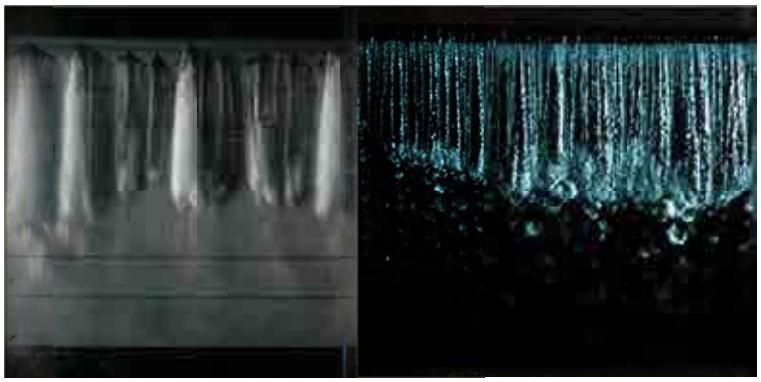

Figure 7.4- Photographs of the different morphology of the cavitation achieved without (left) and with (right) the roughness strip.

As previously stated, two PZT patches made of piezoelectric ceramic material were used as excitation and measuring systems. The patch closer to the leading edge was used as exciter and the other one closer to the leading edge was used as sensor. To keep the hydrofoil geometry and to avoid affecting the flow around the profile, the NACA0009 hydrofoil suction side was mechanized to embed the two patches (see the left side of Figure 7.2). They were electrically isolated with a layer of epoxy, and the connections were protected and hidden inside the structure.

Figure 7.5- 2D views of the different trailing edge solutions adopted. The lower sketch corresponds to the definitive configuration due to its improved performance reducing Von Karman vortexes.

VII.II- Equipment

In order to perform all the scheduled tests, different equipment is required. In this section, a brief description of the main devices used during experimental tests is made.

VII.II.I- Laser Doppler vibrometer (LDV)

Structural velocities were measured with a single point Laser Doppler Vibrometer, LDV Polytec 100. This kind of vibrometer is based on the "Doppler effect" which is the frequency shift of a wave due to the relative movement of the source. In this particular case, the frequency of the emitted laser is slightly shifted when reflected due to the structural vibration. This frequency shift, which is directly related to the velocity of the structure at the measuring point, is evaluated by means of an interferometer and converted to a voltage. The LDV interferometer structure is shown in Figure 7.6.

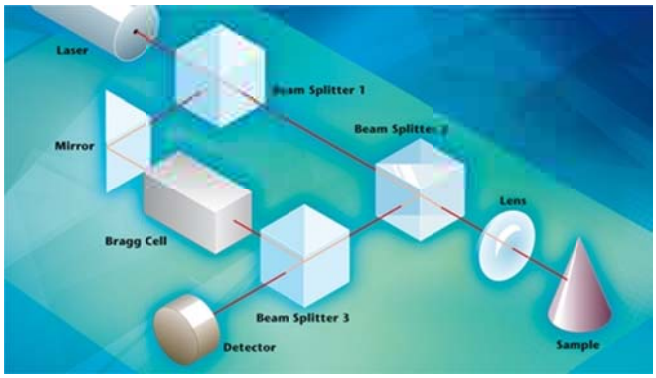

Figure 7.6- Sketch of the LDV interferometer and the laser beam paths (from Polytec GmbH).

An interferometer is basically an optical device which requires two coherent light beams and their respective light intensities I_1 and I_2 to overlap. The resulting intensity is expressed by:

$$I_{tot} = I_1 + I_2 + 2\sqrt{I_1 I_2 \cos\left(2\pi \frac{(r_1 - r_2)}{\lambda}\right)} \qquad (7.2)$$

with $(r_1 - r_2)$ being the "interference" term which relates to the path length difference between both beams and λ stands for the wavelength.

This non-intrusive device measures within a distance range of 0.2 m to 30 m. The specifications of this model are indicated in Table 7.1.

Laser vibrometer specification	
Laser Type	Visible HeNe, class II
Velocity ranges	20, 100, 500 mm/s
Velocity resolution	<0.05, <0.1, <0.3 μm/s
Frequency range	0 – 22 kHz

Low pass filter	1, 5, 22 kHz digital FIR
High pass filter	100 Hz analog
Working distance	0.2 - 30 m

Table 7.1- Polytec 100 LDV specifications.

A specific mounting and displacement system was used to locate and fix the laser beam on the desirable position of the upper surface of the hydrofoil. It is important to mention that the measurements obtained in water have to be "recalibrated" as the refraction index of water is 1.33 times the one in air. Consequently, the resulting measurement had to be divided by the refractive index to obtain the actual displacement.

The vibrometer set-up is straightforward as only the velocity ranges and the high and low pass filters had to be specified. In order to obtain the best possible resolution and decrease the signal-to-noise ratio it is important to set the velocity range as low as possible, checking that the actual measurements do not exceed that range.

VII.II.II- Sensors

VII.II.II.I- Accelerometers

Two different accelerometers were used during this work depending on the test facility. During the preliminary tests with the cantilever beam two to three miniature piezoelectric B&K accelerometers of the type 4394 were used -PZ 23 lead zirconate titanate-. Designed with an integral preamplifier, these IEPE sensors require an external constant-current power supply and operate as voltage sources. In the preliminary tests, the acquisition system itself could energize the accelerometers. This particular type of accelerometers is better suited for higher accelerations as can be seen in Table 7.2, even

though, their small dimensions and weight made them ideal for the purpose of the test as they minimize their effect on the response of the structure.

B&K accelerometer specification	
Acceleration range	±765 g
Sensitivity	9.807 mv/g ±2%
Resonant Frequency	52 kHz
Frequency range	1-25000 Hz
Mass	2.4 g

Table 7.2- B&K 4394 accelerometer specifications.

At the cavitation tunnel a piezoelectric accelerometer model Kistler K-shear 8702B25 was used with the specifications indicated in Table 7.3. This is a low impedance accelerometer, which utilizes a quartz shear sensing element and incorporates a miniaturized built-in charge-to-voltage converter. The main difference with those used in the preliminary tests is that this accelerometer type requires an external power supply coupler, Kistler Power Supply/Coupler 5134A, to energize it.

Kistler accelerometer specification	
Acceleration range	±25 g
Sensitivity	200 mv /g
Resonant Frequency	54 kHz
Frequency range	1-8000 Hz
Mass	8.7 g

Table 7.3- Kristler 8702B25 accelerometer specifications.

VII.II.II.II- Force transducer & Impact hammer

A B&K 8230 type force transducer was used during the preliminary tests to characterize the force exerted by the patch. This kind of transducers are used for measuring applied

forces in modal applications as they are designed for dynamic, short-duration static or impact forces measurements. The transducers work on the piezoelectric effect of quartz, which when stressed, in this case compressed, gives an electrical charge proportional to the compressing force. The specifications of the force transducer are shown in Table 7.4.

Force transducer specification	
Sensitivity	22 mV/N
Max Compression	900 N
Max Tension	900 N
Resonance Frequency	75 kHz
Mass	30.2 g

Table 7.4- B&K 8230 Force transducer specifications.

An instrumented hammer was also used during preliminary tests. As mentioned in a previous section, an impact test was carried out to compare the responses measured with the accelerometers and the PZT patch. A KISTLER 9722A2000 hammer with a steel impact tip-protected with a Delrin cap- was used. This model produced a sufficiently flat excitation band along the desired frequencies. The hammer specifications are indicated in Table 7.5.

Impact hammer specification	
Sensitivity	2 mV/N
Force range	0-2000 N
Max Force	10000 N
Resonance Frequency	27 kHz
Output voltage	±5 V
Mass	100 g

Table 7.5- Kistler 9722A2000 impact hammer specifications.

VII.II.III- Signal generator

In order to feed the PZT patches, a signal –function- generator was required. During all the tests performed at LMH a Wavetek 29 10MHz DDS function generator was used.

Standard and arbitrary functions can be generated and different operating modes are available. In this sense, the tests demanded the sweep mode which has the operating characteristics shown in Table 7.6 and could generate chirp signals.

Wavetek sweep mode specification	
Sweep mode	Linear / Logarithmic
Frequency range	100μHz-10MHz/100kHz depending function
Trigger source	External, Manual or Remote

Table 7.6- Wavetek signal generator sweep operating mode specifications.

The function generator output offers flexibility in terms of amplitude and shape as indicated in Table 7.7. Such flexibility allows us finding the best operating function with the more suitable parameters.

Wavetek output specification	
Output impedance	50/600Ω Switchable
Amplitude	2.5 mV_{pp}- 10 V_{pp} into 50/600 Ω
	5 mV_{pp}- 20 V_{pp} open circuit
DC Offset	±5 V (offset+signal peak) into 50/600 Ω
	±10 V (offset+signal peak) open circuit
Accuracy	3%+ 1 mV at 1 kHz
Resolution	3 digits (limited by 1 mV)

Table 7.7- Wavetek signal generator output specifications.

VI.II.IV- Data acquisition system

The acquisition system to digitize and record the time signals was a NI-PXI 1033 chassis with several PXI 4472 modules connected to it with the specifications indicated in Table 7.8. This particular module has 8 analog inputs with 24-bit resolution ADCs that are simultaneously sampled. In order to program the acquisition procedure a Labview

software routine had been previously implemented with a user-friendly environment which eases its use.

NI-PXI specification	
Analog inputs	8
Resolution	24 bits
Sampling rate	102.4 kS/s
Input range	±10 V
AC cutoff frequency	3.4 Hz

Table 7.8- NI-PXI acquisition system specifications.

During the acquisition of the desired signals and due to the large extensions of data recorded, the waveforms were stored as binary files. This format presents several advantages, namely, they have higher accuracy for floating point numbers, take up less space and perform faster than other types of files such as text-based.

VII.II.V- Multi analyzer system

In the preliminary tests the signal generator and the data acquisition system was substituted by an all-in-one analyzer. This type of multi analyzer with several output and input channels shows flexible configuration and can work as a signal generator and record simultaneously. In particular, it can produce different excitation types. Then, with a built in purpose software the signal processing is easily performed. This particular multi analyzer is the Pulse Multi analyzer system 3560D of Bruel and Kjaer. Its specifications are summarized in Table 7.9.

PULSE Multi channel analyzer			
Inputs		Output	
Freq. Range	0 to 25.6 kHz	Freq. Range	0 to 25.6 kHz
Voltage Range	7 ranges from 7.071mV to 7.071V	Voltage Range	7.07μV to 7.07V
		Impedance	50 Ω
High Pass Filter	DC; 0.7; 7; 22.4 Hz	Waveforms	Sine, Dual sine, Random, User-defined

Table 7.9- Pulse multi-channel analyzer specifications.

Experiments

A detailed description of the different experimental tests performed in the cavitation tunnel is given in this section. An extensive explanation of the post-processing methods and tools used to treat different data signals is also presented.

VIII.I- Methodology

VIII.I.I- Modal analysis of a cavitating hydrofoil

The aluminum NACA0009 was mounted at the LMH High Speed Cavitation Tunnel. Before filling the tunnel, a modal analysis was performed to obtain the reference natural frequencies which will be assumed to be "A*ir*" condition. Then, with the tunnel full of still water, the "*Still water*" conditions were also obtained

To simplify the post-processing routine and avoid the introduction of other noise sources, the best hydrodynamic conditions (in terms of flow velocity and incidence angle) had to be found. Therefore, a systematic search was conducted by tuning both variables. It was

observed that the cavities were unstable for flow velocities between 15 and 20 m/s, and large vibrations were induced in the hydrofoil. In the range from 5 to 10 m/s, the stable cavities were non-uniform along the entire span, and the two-phase mixture was not sufficiently homogeneous. A lock-in phenomenon occurred for flow velocities of approximately 11 m/s; for incidence angles of between 3° and 5°, the cavity was not attached to the hydrofoil suction side, and unstable shear cavitation took place instead. For incidence angles lower than 1°, the vortex shedding was significant, and cavitation also appeared on the pressure side. Consequently, the cavitation tunnel upstream velocity was ultimately fixed at 14 m/s, and two incidence angles of 1° and 2° were selected for the experiments.

Under these conditions, steady partial cavities were obtained by decreasing the value of sigma over lengths ranging from 2% to 44% of the chord for an incidence angle of 1° and from 2% to 75% for an incidence angle of 2°. Photographs were taken from the top and lateral sides of the test section during the tests, as shown in Figure 8.1. These images were obtained with a 50-μs duration flash lamp synchronized with a digital photo camera.

The supercavitation condition was also investigated for both incidence angles. This type of cavitation occurs when the cavity length extends beyond the hydrofoil's trailing edge. The bottom photograph in Figure 8.1 shows an example.

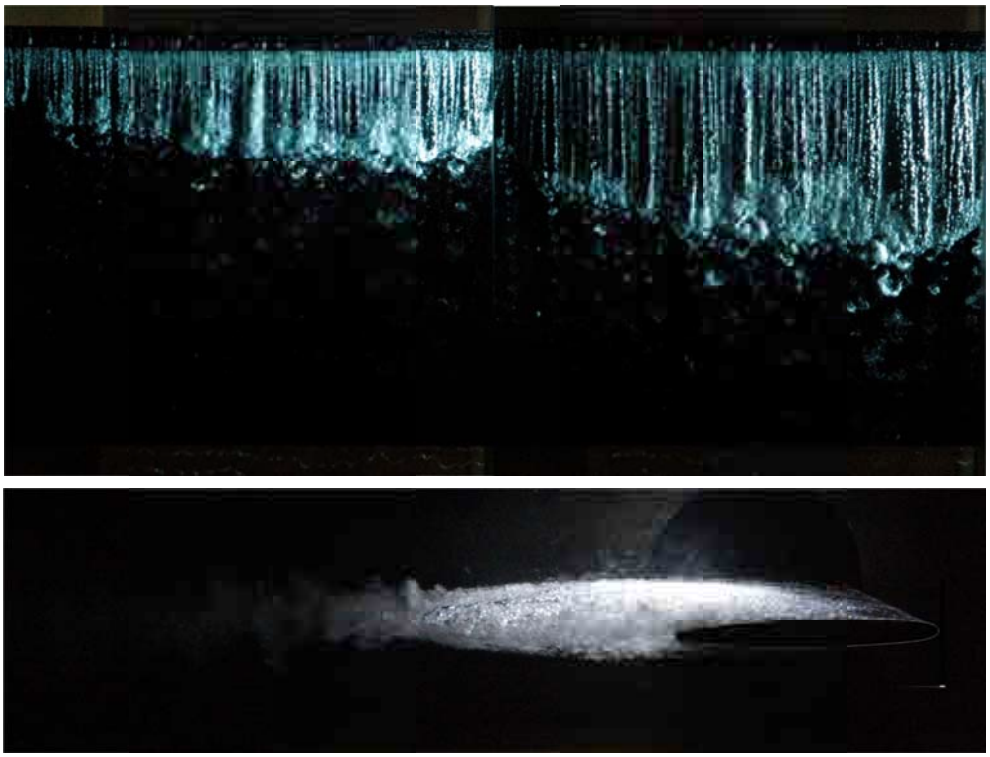

Figure 8.1 - Detail of different partial cavity lengths (above) and supercavitation (below).

The so-called modal analysis performed to determine the natural frequencies during this work requires a detailed explanation. As commented in the preliminary tests, the excitation of the natural frequencies of the profile was performed by means of PZT patches. A 120-second lineal chirp was sent to the leading edge patch to excite the structure. At the same time, the trailing edge patch measured the response of the profile. These chirps covered a frequency band of 240 Hz with a constant frequency increase factor of 2 Hz/s. It is obviously necessary to locate the unknown frequency within this range to detect the resonance. The frequency range excited in each chirp differed depending on the mode sought or the conditions in the test section, and several different chirps were required in certain cases to identify the natural frequency. The ranges investigated with the chirp signals for each flow condition are listed in Tables 8.1 and 8.2.

It should be mentioned that the voltage level input was also varied depending on the noise conditions of the test section.

Hz	Air	Water
f_1	140-380	0-240
f_2	880-1120	490-730
f_3	1500-1740	760-1000

Table 8.1 - Starting and ending chirp frequencies for tests with air and water in the absence of cavitation.

	Normalized cavity length (l/c)					
	0,02	**0,054**	**0,114**	**0,318**	**0,442**	**>1**
f_1 (Hz)	70-310	70-310	70-310	70-310	70-310	70-310
f_2 (Hz)	490-730	570-810	570-810	570-810	570-810	880-1120
f_3 (Hz)	760-1000	810-1050; 1050-1290	810-1050; 1050-1290	810-1050; 1050-1290; 1290-1530	810-1050; 1050-1290; 1290-1530	1500-1740

Table 8.2 - Starting and ending chirp frequencies for tests in the presence of cavitation.

VIII.I.II- Hydrofoil-lateral wall gap

Due to the existence of a small lateral gap between the NACA0009 and the plexiglass lateral wall of the tunnel, a detailed analysis of its influence on the natural frequencies of the hydrofoil was conducted because the published literature on the effects of solid boundaries on the added mass clearly indicates their significance.

Three different experimental conditions with the hydrofoil mounted in the tunnel test section were tested:

- Tunnel empty of water (*Air* condition).
- Tunnel full of still water (*Still water* condition)
- Tunnel with flowing water at 9 m/s (*9 m/s* condition).

In the last case, cavitation did not take place because the pressure within the test section was kept sufficiently high. The hydrofoil incidence angle was held at -2º to minimize vortex-shedding noise.

For all the cases, the lateral gap was increased from a minimum value of 0.12 mm to a maximum of 2.12 mm by means of different metallic plates of calibrated thickness, which were placed between the hydrofoil subjection system and the tunnel wall. In this way, the inside lateral gap was increased, and its influence could be studied. For each gap distance, modal analysis was performed following the same procedure explained in the preceding section.

VIII.I.III- Partially submerged hydrofoil

A reproduction of the work of Lindholm et al. (1965) was performed with the NACA0009 in place of rectangular beams. The idea behind this test was to study the effect of the relative location of the free surface of the water on the different modes of vibration of the hydrofoil.

The profile was located perpendicular to the free surface of the water, and the tunnel was filled in stages. A modal analysis was performed from 0% to 100% submergence for each 10% submergence variation. Additionally, because the profile is non-symmetric, the two different orientations were taken into account by analyzing the body with the leading edge or the trailing edge submerged, as observed in Figure 8.2.

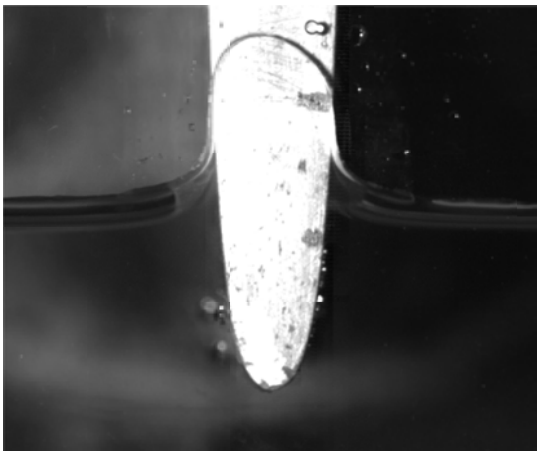

Figure 8.2 - Partially submerged hydrofoil. Orientation: leading edge.

This particular test was performed entirely under *still water* conditions. The methodology of the modal analyses is analogous to those explained above.

VIII.I.IV- Mode shapes visualization

One of the main uncertainties when added mass effects are determined by comparison of natural frequencies in different fluids (e.g., air-water) is related to the hypothesis that the mode shapes do not differ significantly. This behavior has been proven when the surrounding fluids are still (Rodriguez et al. 2006), but there is no published evidence for the case of flow conditions. Furthermore, in the case of two-phase flows with more complex boundary conditions, such an assumption is not trivial. The objective of this test was to visualize the hydrofoil mode shapes under different flow conditions for comparison and evaluation of their level of similarity.

First, 26 measuring points were chosen on the profile surface to characterize each mode shape (Figure 8.3) by means of displacement measurements under resonance conditions using the laser vibrometer. These points, which were required to be visually accessible

through the upper plexiglass window of the tunnel, were identified by means of a reflective tape that improved the intensity of the laser.

Four different conditions were tested:

- Tunnel empty of water (*Air* condition)
- Tunnel full of still water (*Still water* condition)
- Tunnel with flowing water at approximately 11.8 m/s and no cavitation (*Flowing* condition)
- Tunnel with cavitating flow at approximately 11.8 m/s (*Cavitating* condition).

The flow velocity was fixed at approximately 11.8 m/s because it resulted in the minimum velocity necessary to obtain a controllable and stable cavity of approximately 50% of the chord.

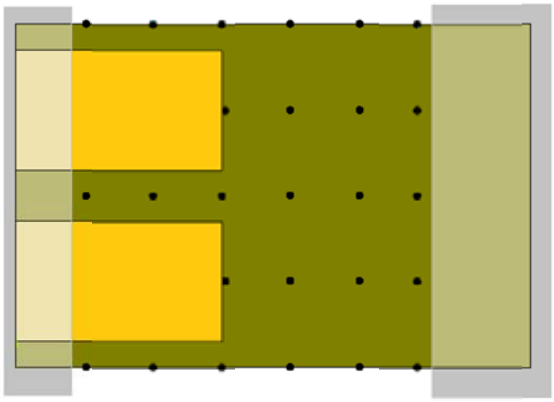

Figure 8.3 - Sketch of the different measurement points located over the hydrofoil surface for mode shape identification. The gray zones represent visually inaccessible regions.

The first step was to identify the first three natural frequencies of the hydrofoil for each condition. Frequency identification was performed by means of modal analysis. Once obtained, the profile was excited with the leading edge patch (or both patches, depending

the noise level inside the test section) for a 60-second duration at the particular frequencies for each point of the response acquisition. For each condition, the position of the LDV was adjusted to sweep the 26 different points along the surface of the profile, and the responses were acquired for each mode of vibration and flow condition.

The ME'ScopeVES, which stands for Mechanical Engineering Oscilloscope - Visual Engineering Series, is a post-processing tool that allows the user to analyze and visually observe the vibration data. The software is capable of working with multiple time- or frequency-domain channels and displaying spatially defined data such as mode shapes. As a result, the user can animate and observe the actual motion of the structure under study.

The shape of the profile was simplified to a 0.15 x 0.1 m plate and drawn in ME'ScopeVES (Figure 8.3). The 26 point locations were also imported together with the time data acquired by means of the LDV. An animation of the plate motion allowed identification of the mode shape and its characteristics.

VIII.I.V- Pressure distribution on the hydrofoil

This experiment consisted of a systematic modal analysis of the hydrofoil under different pressure distributions in a non-cavitating flow. Four different incidence angles and eight different flow velocities were tested. All of the studied scenarios are summarized in Table 8.3.

Incidence angle	Flow velocity
-1º	0, 5, 7, 10, 12, 15, 18, 20 m/s
-2º	0, 5, 7, 10, 12, 15, 18, 20 m/s
-5º	0, 5, 7, 10, 12, 15, 18 m/s
-7º	0, 5, 7, 10, 12, 15 m/s
-10º	0, 5, 7, 10, 12 m/s

Table 8.3 - Experimentally tested scenarios for the pressure distribution study.

To avoid cavitation in any of the scenarios, the test section pressure was increased to 5 bar and maintained as a constant during all of the test cases.

VIII.II- Post-processing of measured signals for natural frequency extraction

Most of the experimental tests explained in the previous section are based on a modal analysis from which one expects to extract the natural frequencies of the structure under all of the different conditions. The identification of the hydrofoil natural frequencies from the measured responses was performed using two different signal-processing methods. These techniques should be capable of addressing the inherently transient nature of the excitation signal and the induced structural response. Both methods consisted of identifying the excitation frequency that provoked the maximum amplitude of the hydrofoil response resulting from the resonance with a natural frequency. Interested readers can find a brief description of the signal processing techniques in Appendix B, which gives the theoretical basis of the following explanation.

With respect to our experience in the present work, under conditions with a still fluid, the response time signal alone is sufficient to find the maximum amplitude and

corresponding frequency by taking into account the chirp excitation parameters. For example, the measured response during a chirp excitation passing through the first bending mode of vibration (f_1) is shown in Figure 8.4.

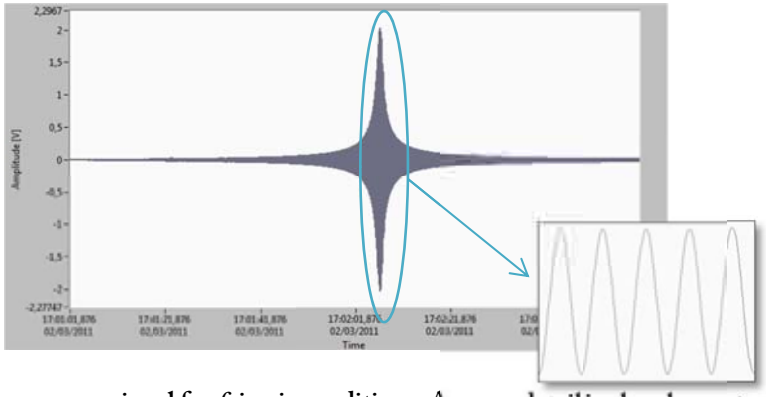

Figure 8.4- Time response signal for f_1 in air conditions. A zoom detail is also shown to visualize the sinusoidal nature of the response.

However, this procedure provides poor results when used during flow conditions because other hydrodynamic excitation sources (i.e., flow turbulence, vortex shedding and cavity collapse) also induce significant vibrations on the structure. Consequently, the amplified resonant response is masked by noise.

The averaged power spectra of the signal responses measured under no flow, flow without cavitation and cavitation conditions are compared in Figure 8.5 to demonstrate the different signal-to-noise ratios encountered with various flow types. These responses were generated with the same chirp excitation, in terms of the amplitude and frequency ranges, in a bandwidth without any resonance from 180 Hz to 200 Hz at a rate of 2 Hz/s. Each 10-second time signal was divided into five segments, and the averaged power spectrum was computed. The broadband peak resulting from the swept excitation was clearly detected in the absence of flow. When the fluid flowed without cavitation, the vibration levels clearly increased in the entire baseband, but the dominant response corresponding

to the mechanical excitation imposed by the patch was still observed. Finally, when cavitation occurred, an additional increase in noise was observed over the entire frequency range relative to the no-cavitation condition, indicating the presence of higher levels of induced vibrations.

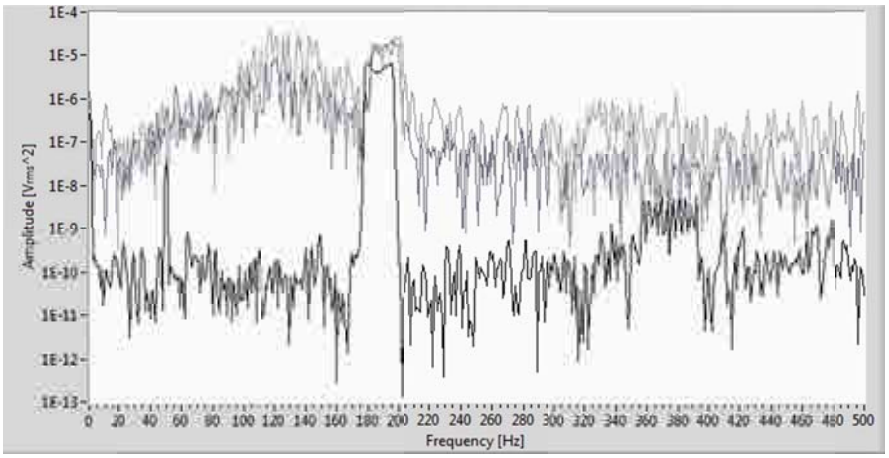

Figure 8.5- Averaged power spectra measured under no flow (black), flow without cavitation (dark grey) and sheet cavitation (light grey) conditions for an incidence angle of 2° showing the response of the hydrofoil under a chirp excitation from 180 Hz to 200 Hz.

As previously stated, two different signal processing techniques were used to improve the detection of the natural frequencies from such noisy signals.

In the first technique, a Labview routine was built in which the signal response and the excitation signal were split into different portions. Those portions were subsequently filtered into sliding frequency bands of constant bandwidth ranging from the starting to the ending chirp frequency. Finally, the filtered signals were windowed, and the cross-power spectrum was computed to measure their level of similarity. From the amplitude analysis of the resulting cross-power spectra at the chirp frequency, it was possible to visually identify the resonance conditions. Appendix C shows an example of such a routine in the Labview environment.

To prevent misinterpretation of the graphs, a mathematical tool was applied to approximate the real signal with a function. Several curve-fitting options were tested. In particular, an equally weighted third-degree spline showed good results for minimizing the residuals, as calculated by equation (8.1):

$$\text{Residue} = \frac{1}{L}\sum_{k=0}^{L-1} w_k \cdot [(x_k - x'_k)^2 + (y_k - y'_k)^2] \quad (8.1)$$

where L is the length of the signal, w_k is the k^{th} element of the weight, (x_k, y_k) is the signal k^{th} pair of elements and (x_k', y_k') are the spline k^{th} pair of elements. This particular routine is shown in Appendix C. As an example, Figure 8.6 shows several output plots generated by this routine with the third-degree spline approximation overlapped in red.

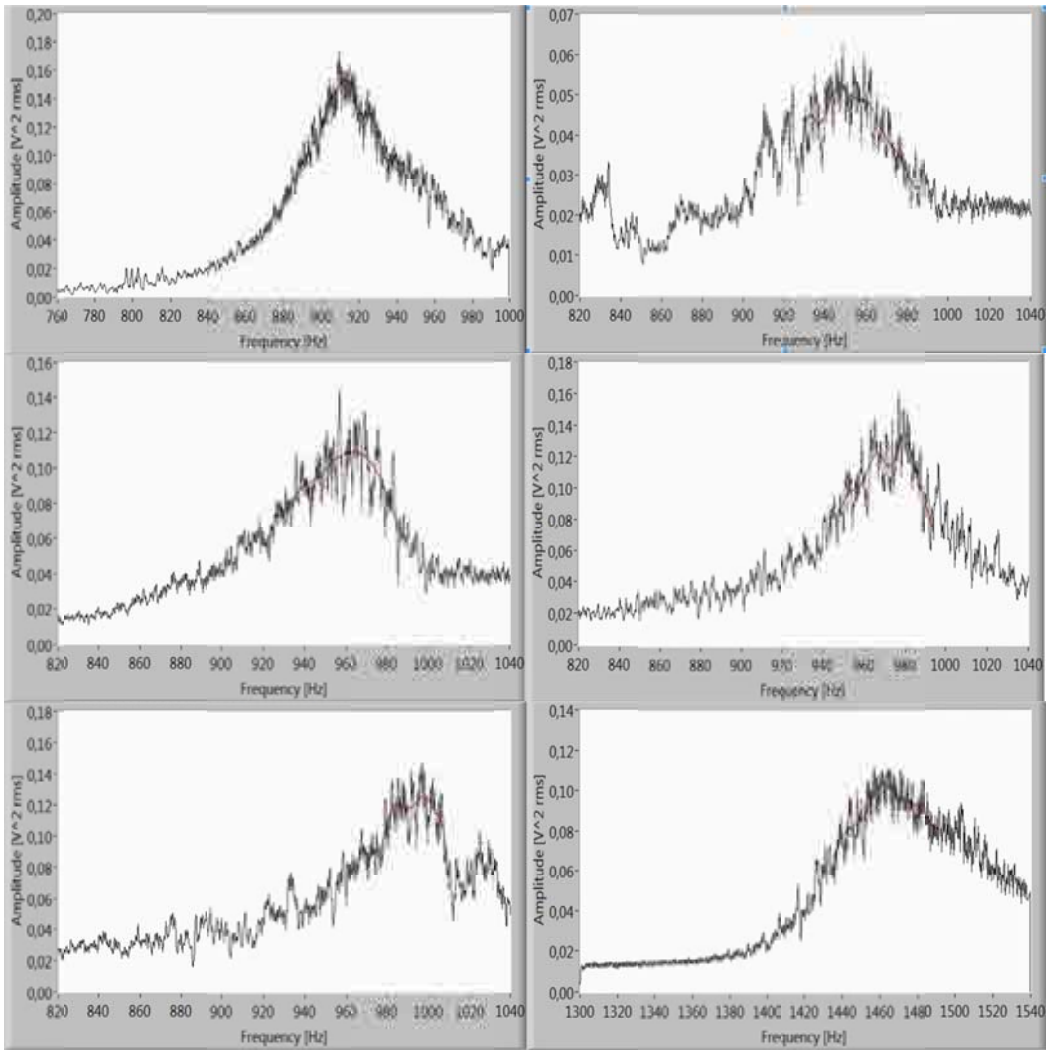

Figure 8.6- Response gains as a function of excitation frequency (grey) and spline approximations (red) used to identify f_3 at 1° for each sheet cavitation scenario.

For verification purposes, a second signal processing method was also applied, which consisted of a Joint Time Frequency Analysis (JTFA) based on the Short Time Fourier Transform (STFT) applied to low-pass filtered response signals to remove their high frequency noise. Using this technique, the Fast Fourier Transform (FFT) was consecutively applied to short segments of the time signal with an overlapping factor, and

a spectrogram was eventually generated. This type of 3D graph plots the amplitude of the response (color scale) against the frequency and the time (see Figure 8.7). Notably good agreement was found between both techniques.

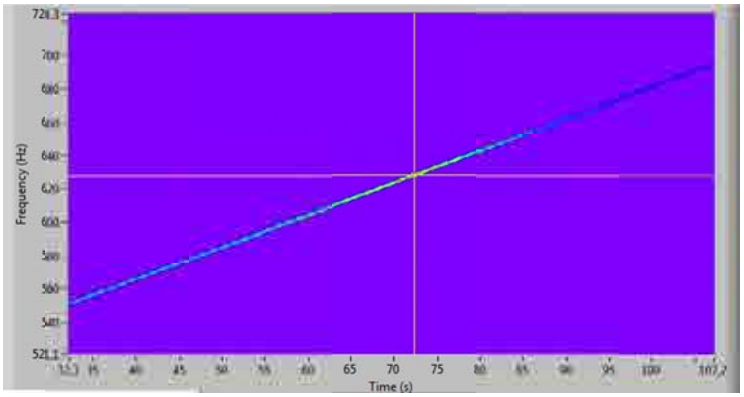

Figure 8.7 - A typical result obtained by the STFT post-processing method for a given signal.

Numerical simulation

A subset of the experimental tests described in the previous section were also numerically simulated by Ansys software. A brief explanation of the software environment and background is given in this section. The last section of this chapter explains the numerical model and the assumptions adopted in each case to approximate the model to our experimental conditions.

IX.I- Platform and approach

The Ansys simulation tool is a multi-physics software package that allows the resolution of coupled or uncoupled problems within different fields, including as structural mechanics, heat transfer, acoustics, and electromagnetism. These CAE (Computer-Aided Engineering) tools are useful because they avoid the time and other costs associated with experimental tests. The level of current development of these tools makes them reliable for most engineering fields.

The Ansys software is based on the finite element method (FEM) of problem resolution (Gupta and Meek 1996). This method, which is a rather effective approach to complex engineering problems, is based on the approximation of a continuous domain by discretization into simpler elements with specific properties. These elements are connected by nodes, which determine the size of the system that must be solved. Additionally, the required boundary conditions must be defined and applied. This method approximates differential equations (continuous problem) to an algebraic system of equations (discrete problem) delimited by the number of nodes of the model. Zienkiewicz and Taylor (2000) applied this methodology to a vast number of examples in different fields with good results.

Our particular case, the FSI problem, is defined as a coupled problem involving both the structural and fluid mechanics fields. Ansys allows us to model coupled problems, but several assumptions and approximations should be clearly explained in advance. Under the Acoustics field, as commented in previous sections, the structural dynamics equation must be considered together with the Navier-Stokes equations (White 1994). The fluid domain requires several assumptions that simplify the analysis:

I- The fluid is compressible (due to pressure variations).
II- The fluid is inviscid.
III- There is no mean fluid flow.
IV- The mean density and pressure are uniform throughout the fluid.

In this way, we obtain the acoustic wave equation:

$$\frac{1}{c^2}\frac{\partial^2 P}{\partial t^2} - \nabla^2 P = 0 \qquad (9.1)$$

where c is the speed of sound in the fluid, P is the pressure and t is the time. This equation and the structural dynamic equation (equation 2.14) constitute the FSI system

solved by Ansys. Because the fluid is modeled as inviscid, a dissipation term is added to account for the dissipation of energy due to the damping effect in the fluid boundary. Next, the structural dynamic equation (2.14) and equation (8.1) are discretized, leading to a FSI system such as the following:

$$\begin{bmatrix} M_e & 0 \\ M^{fs} & M_e^p \end{bmatrix} \begin{bmatrix} \ddot{u}_e \\ \ddot{P}_e \end{bmatrix} + \begin{bmatrix} C_e & 0 \\ 0 & C_e^p \end{bmatrix} \begin{bmatrix} \dot{u}_e \\ \dot{P}_e \end{bmatrix} + \begin{bmatrix} K_e & 0 \\ 0 & K_e^p \end{bmatrix} \begin{bmatrix} u_e \\ P_e \end{bmatrix} = \begin{bmatrix} F_e \\ 0 \end{bmatrix} \quad (9.2)$$

where M_e, C_e and K_e are the mass, damping and stiffness matrices, respectively, and F_e is the applied load vector. The super-index p denotes the fluid matrices, and the unknown variables are the displacement (u_e) and pressure (P_e).

The cases under study via numerical simulation are those involving still water, i.e., the lateral gap and the partially submerged hydrofoil tests. A numerical approach should allow us to analyze the effects of those boundaries on the added mass of a structure and therefore on the natural frequencies of the profile. If sufficiently accurate, the comparison of both results (numerical and experimental) should be able to extend the validity of the simulation to similar boundary conditions not yet experimentally tested.

IX.II- Model and mesh

Chronologically, the model setup was first performed to assure the validity of the results, and two different cases were subsequently simulated:

a) Lateral gap analysis.
b) Partially submerged hydrofoil.

IX.II.I- Model set-up

A NACA0009 profile of the same dimensions was modeled within the Ansys environment (Figure 9.1). The mesh, which determines the number of nodes of the model and hence the size of the system (equation 9.2), is an important parameter in any

numerical simulation. Obviously, a good solution to any problem must be mesh independent, which means that it should output the same solution regardless of the size of the mesh. For this reason, an important preliminary step was devoted to analysis of the model's mesh sensibility.

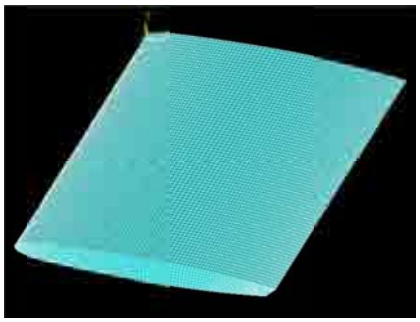

Figure 9.1 - "In vacuum" NACA0009 profile modeled in the Ansys environment.

A sensibility analysis of the solid domain mesh was performed to determine its optimal size. First, the number of elements in the profile chord direction was fixed by setting the number of partitions of the lines that enclose the lateral surface. Next, the number of partitions of the lines in the span-wise direction was varied to analyze its influence on the obtained natural frequencies.

Figure 9.2 shows the deviation in percentage of the natural frequencies plotted against the number of partitions, assuming that the results obtained with 300 partitions in the span-wise direction is the exact solution (see Appendix *D* for additional data on the mesh sensibility analysis). As shown, the solution under vacuum conditions (with no fluid domain yet defined) converges quickly, and only a coarse mesh is required to obtain a satisfactory solution.

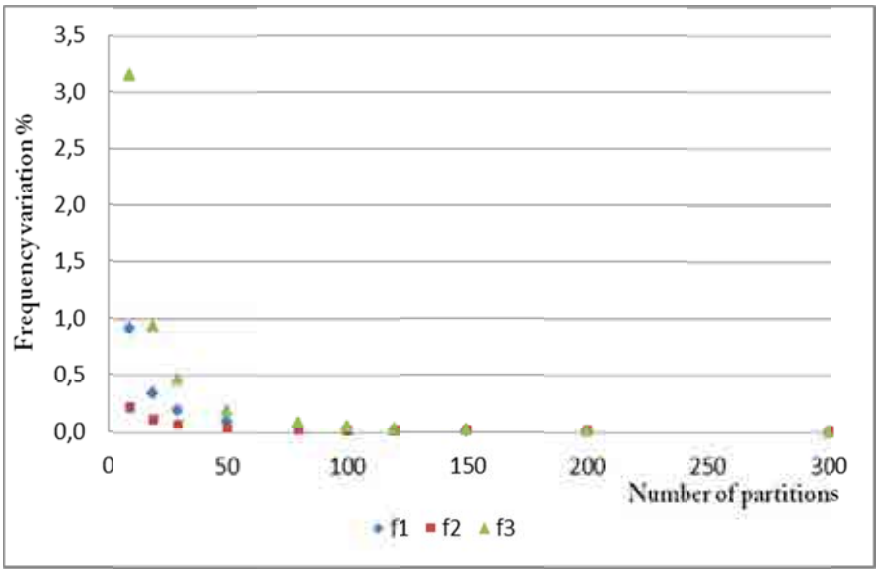

Figure 9.2 - Solution variation in % for the three modes plotted against the number of partitions in the span-wise direction.

A fluid domain was subsequently modeled around the profile (Figure 9.3). This domain can be changed from *Air* to *Water* by setting the elemental material properties depending on the conditions simulated (Table 9.1). A sensibility analysis was also performed.

Material	Sonic Velocity (m/s)	Density (kg/m^3)
Air	343	1.2
Water	1482	998

Table 9.1- Material properties set in Ansys model for air and water.

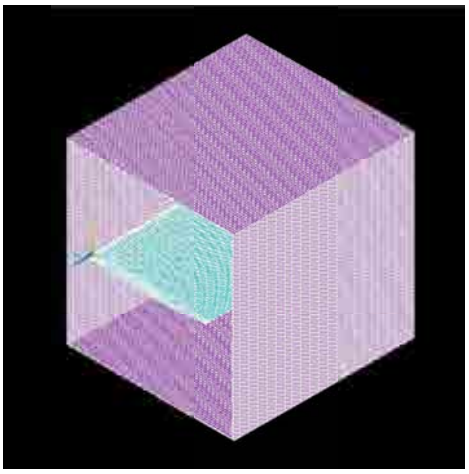

Figure 9.3 - NACA0009 profile (blue) and fluid domain (purple) in Ansys.

Taking into account the test section dimensions, one can model the fluid volume in two of the three axes of the problem. It is obvious that the length of the fluid domain in the horizontal axis, *h*, is not bounded by the test section (Figure 9.4). It is therefore mandatory to analyze the influence of this variable to carefully determine the final fluid domain volume.

Because the fluid boundaries were modeled as fully reflective, which means that they are capable of reflecting the wave pressure (equation 9.1) with no energy loss, the location of the walls with respect to the solid domain was expected to influence the numerical solution. Therefore, the size of the fluid volume was increased in its horizontal dimension, *h*, in a step-by-step manner, and the natural frequencies were obtained for each case. Figure 9.5 shows the natural frequency variation (%) with respect to the horizontal dimension. After examining the results, a horizontal dimension of h= 0.13 m was finally chosen.

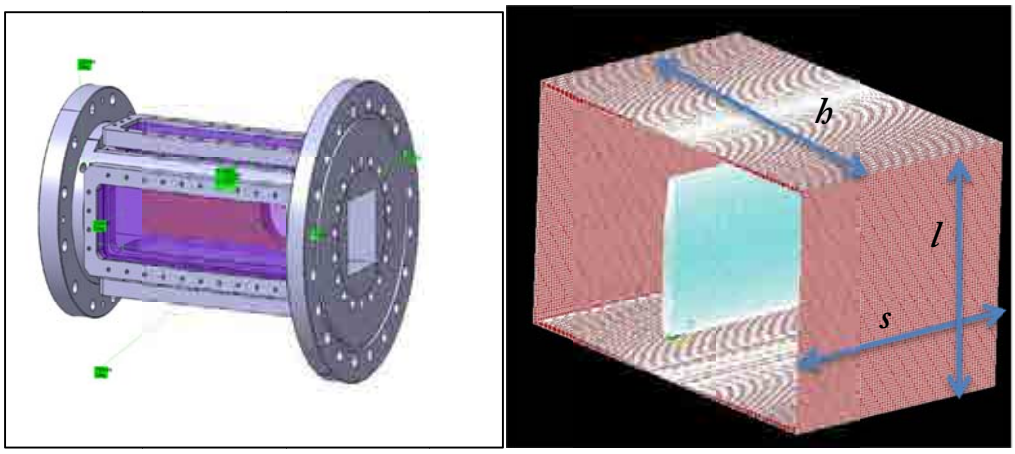

Figure 9.4 - Sketch of the LMH cavitation tunnel test section (left) and its model representation in Ansys (right) with corresponding dimensions.

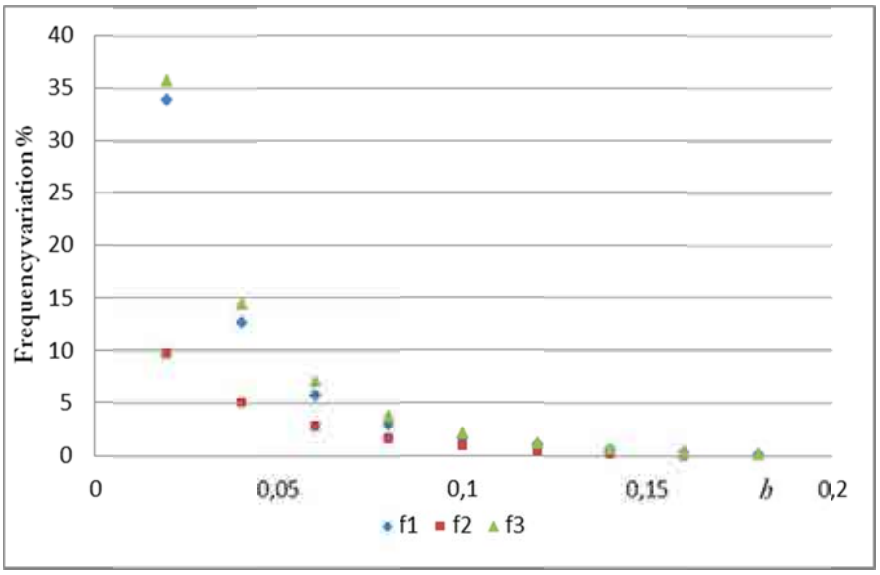

Figure 9.5 - Natural frequency variation in % as a function of the horizontal dimension of the fluid domain, *b*.

Because the profile was clamped in only one section, a small lateral gap existed between the hydrofoil and the tunnel wall. Under normal conditions, the size of this gap is approximately 0.12 mm. In this context, the gap was also modeled and the subsequent

fluid domain resulted in a cubic volume of dimensions 0.15012 (*s*) x 0.15 (*l*) x 0.13 (*h*) m (see Figure 9.4). Due to the small transversal size of the gap and to avoid degradation of the quality of the mesh, the number of fluid elements had to be substantially increased with respect to the previous sensibility analysis. In addition, another sensibility analysis was performed within the gap dimension.

To capture this phenomenon, the gap distance was meshed with different amounts of fluid elements. A simplified 2D model was used for this proof, and therefore, only the bending modes could be studied, which were expected to be those most sensitive to the gap effect. As observed in Figure 9.6, the difference in natural frequency (%) between meshing of the gap dimension with 10 elements or with 1 element falls below 0.1%. Therefore, under normal conditions (0.12 mm), one unique element was eventually used to mesh the gap distance.

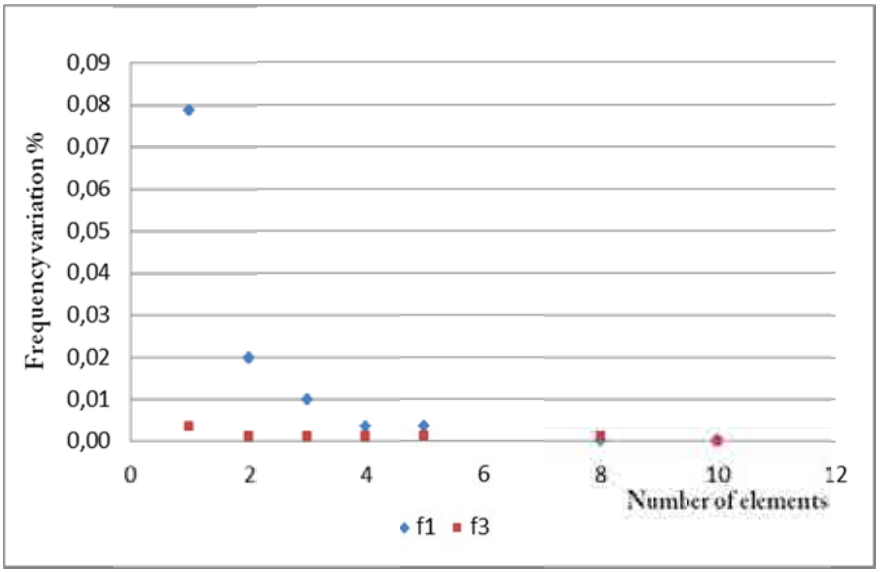

Figure 9.6 - Solution variation in % plotted against the number of elements in the gap direction for f_1 (blue) and f_3 (red).

Due to the mechanization of certain parts of the NACA0009 (i.e., locations of the PZT patches, drill holes to pass the wires and other sensors), the average structural properties of the material were modified. To force the results to converge to the experimental frequencies, the NACA0009 material was slightly modified by tuning its density, Young's Modulus and Poisson coefficient.

The selected structural elements were the SOLID45 type, which is an 8-node 3D element for solid structures with three degrees of freedom (displacements in the *x*, *y* and *z* directions). Different material properties are available, but in this particular study of modal analysis, only the density, the Young's modulus and the Poisson coefficient were required. Moreover, the element SOLID45 is able to admit pressure loads.

The selected fluid elements were the FLUID30 type, which is an 8-node 3D acoustic fluid element for modeling the fluid medium with four degrees of freedom (displacements in the *x*, *y* and *z* directions and pressure). For modal analysis, only the density and the sonic velocity are required as material properties to obtain equation (9.1). In addition, a special option is available to identify those fluid elements in contact with structural elements (interphase), producing an unsymmetrical element matrix. Surface loads (FSI) must also be applied at the interphase.

IX.II.II- Lateral gap analysis

The initial model dimensions for this case were 0.15012 x 0.15 x 0.13 m, and the definite mesh was composed of 53640 SOLID45 elements and 610406 FLUID30 elements.

Experimentally, the lateral gap was increased from 0.12 mm to 2.12 mm by moving the profile backwards. In Ansys, this procedure was simulated by increasing the fluid volume in the gap dimension from 0.15012 to 0.15212 m. Because the mesh sensibility in the gap dimension had been previously studied, each increase of the gap distance was modeled as

indicated in Table 9.2 by increasing the number of element layers according to the distance.

Gap distance (mm)	Number of elements in gap direction
0.12	1
0.22	1
0.32	2
0.42	3
0.62	5
0.72	6
0.82	6
1.12	9
2.12	17

Table 9.2 - Gap distances and fluid elements used to model them.

IX.II.III- Partially submerged hydrofoil

The fluid volume dimensions and mesh are the same as the initial conditions of the gap analysis.

Once the mesh had been verified, the numerical approach to simulating the step-by-step filling of the tunnel test section consisted of changing the material properties for a certain number of elements depending on the submergence level of the hydrofoil. In other words, if the profile was partially submerged in water, a modal analysis in Ansys was performed

with the assumption that the upper part of the fluid domain was *Air* and the lower part of the fluid domain was *Water* (Figure 9.6).

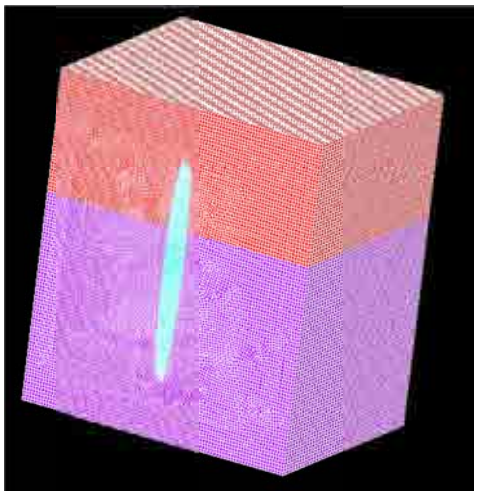

Figure 9.7 - Sectional view of the NACA0009 profile partially submerged in water (purple domain) and in contact with air (red domain).

For this simulation and to avoid modeling the free surface as a fully reflective boundary (which would lead to an overestimation of the added mass results), the pressure of the *Air* nodes was fixed to atmospheric pressure. This setting avoids allowing the wave pressure to be reflected by the free surface because the nodes in this boundary do not have any additional flexibility in their pressure degree-of-freedom.

PART III: RESULTS AND DISCUSSIONS

This part is devoted to an exposition and discussion of the experimental and numerical results. Because these topics are all deeply related, the analysis is best performed in conjunction. Therefore, we first present the main results and postpone their discussion and comparison to the last chapter of the present section.

Experiments

First, the measurements and visualization of all mode shapes are presented to verify their similarity among the different tested scenarios. Next, the main results are given for the added mass effect under cavitation conditions. Additionally, results for certain other factors that may influence the main test (i.e., the lateral gap distance and flow condition) are also presented.

X.I-Effects of experimental conditions on mode shapes

The first three hydrofoil mode shapes are presented in 3D graphs in which the geometry of the hydrofoil is simplified to a cantilevered plate. In these plots, the yellow color denotes maximum displacement and the dark blue color denotes the minimum. Each mode shape is plotted separately under the different conditions for better comparison. Moreover, two images indicate the maximum deflection of each studied scenario. The corresponding numerical values (relative amplitude magnitude and phase) are summarized in Tables E.1, E.2, E.3 and E.4 of Appendix E.

First bending mode (f_1)

The first bending mode is shown in Figure 10.1 under the four different tested conditions: *Air* (top two images), *Still water* (the following two images), *Flowing* conditions (next two images) and *Cavitating* conditions (bottom two images).

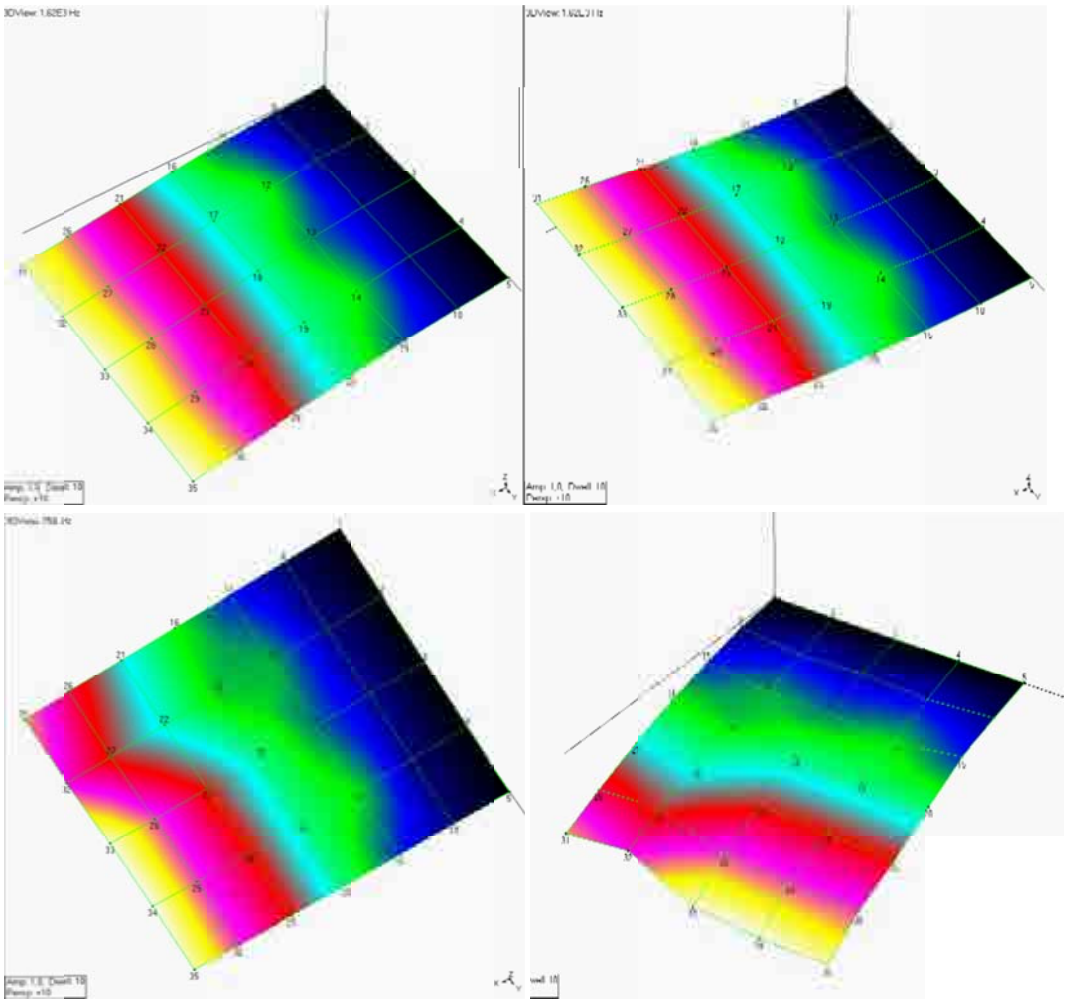

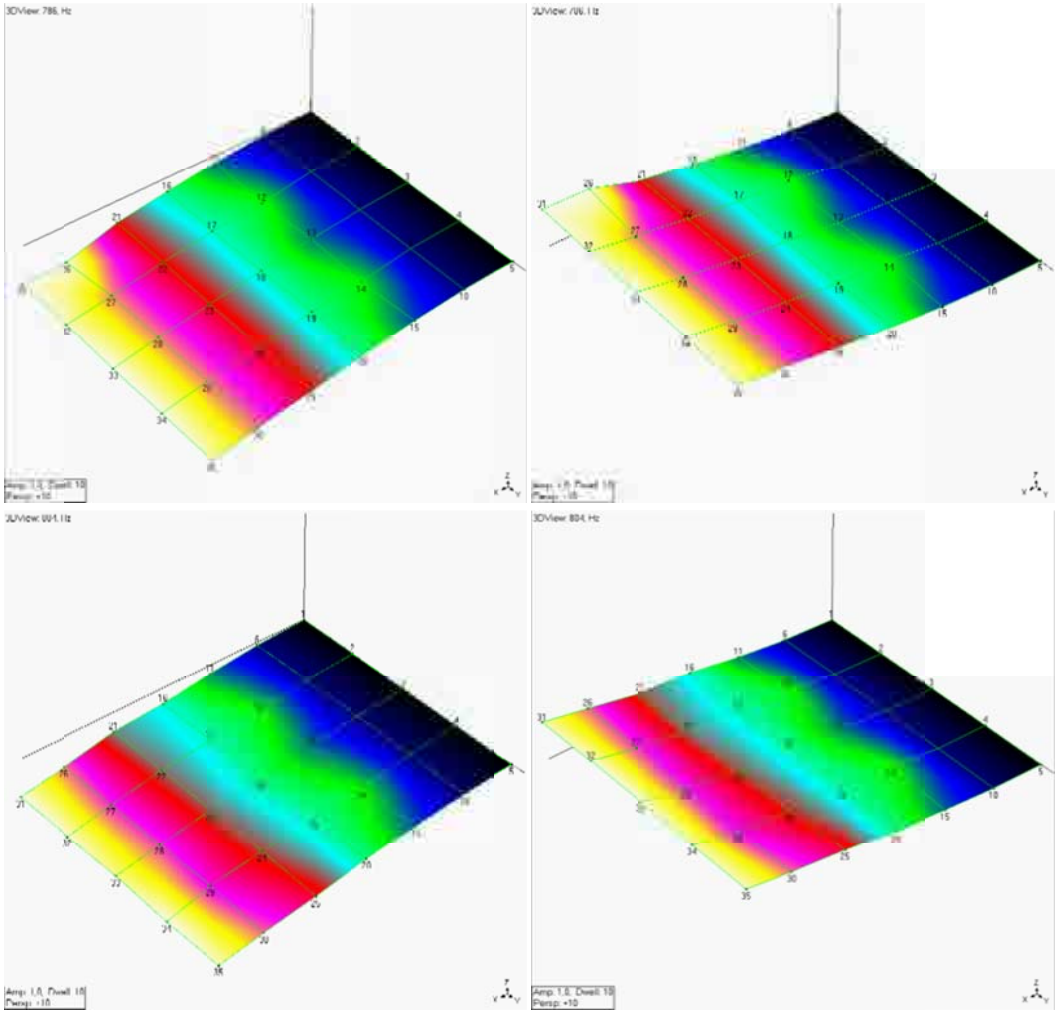

Figure 10.1 - First bending mode shape for different boundary conditions: *Air* (top two images), *Still water* (the following two images), *Flowing* (next two images) and *Cavitation* (bottom two images).

First torsion mode s (f_2)

The first torsion mode is shown in Figure 10.2. The order of the images is analogous to those of the first bending mode in Figure 10.1.

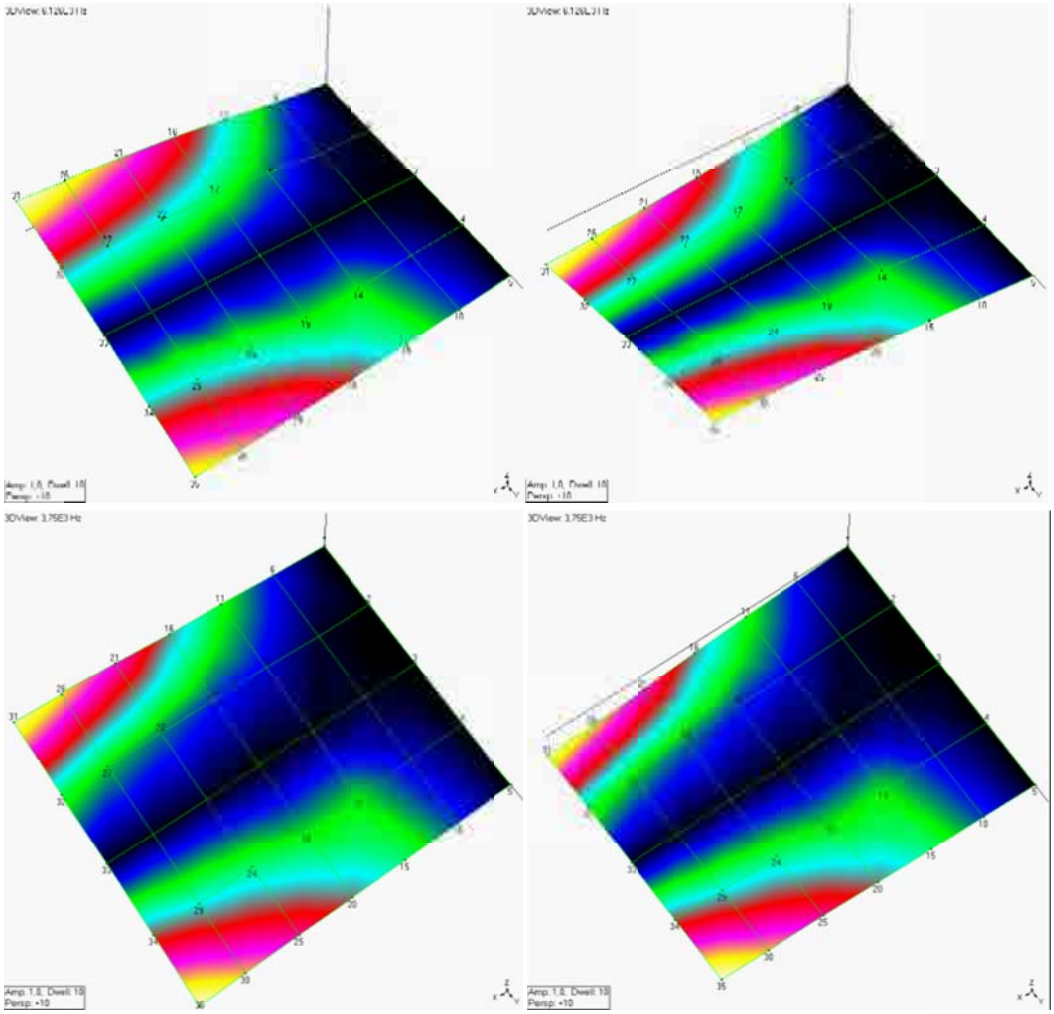

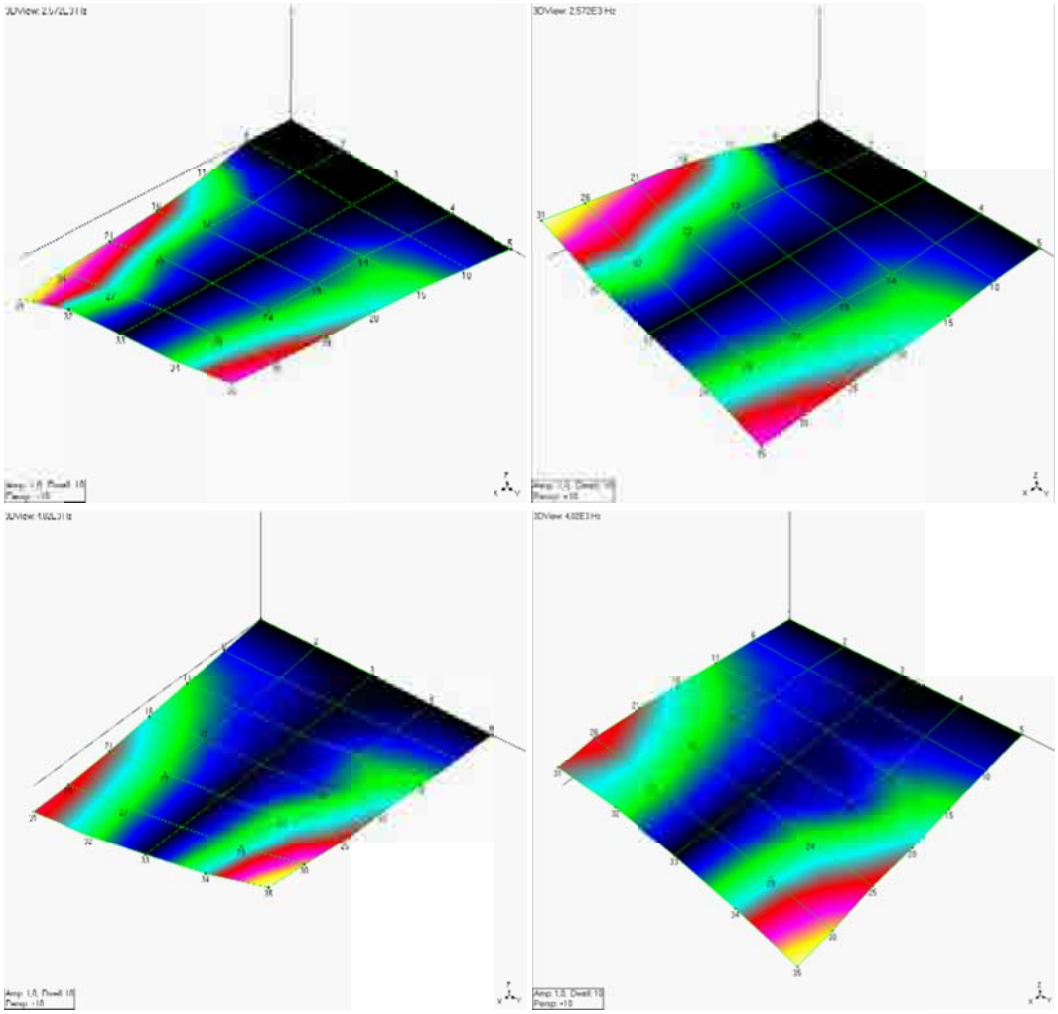

Figure 10.2 - First torsion mode shape for different boundary conditions: *Air* (top two images), *Still water* (the following two images), *Flowing* (next two images) and *Cavitation* (bottom two images).

Second bending mode (f_3)

The second bending mode is shown in Figure 10.3. The order of the images is analogous to the previous cases.

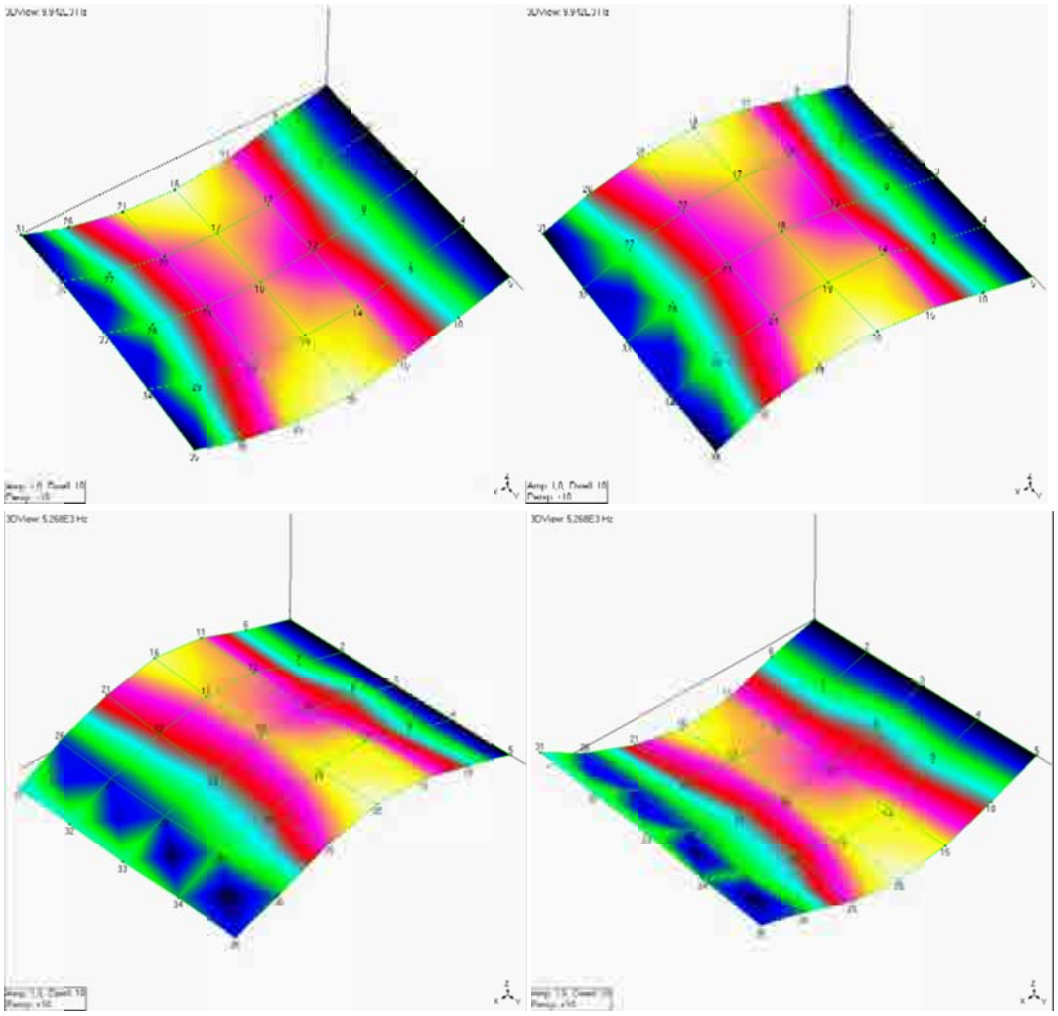

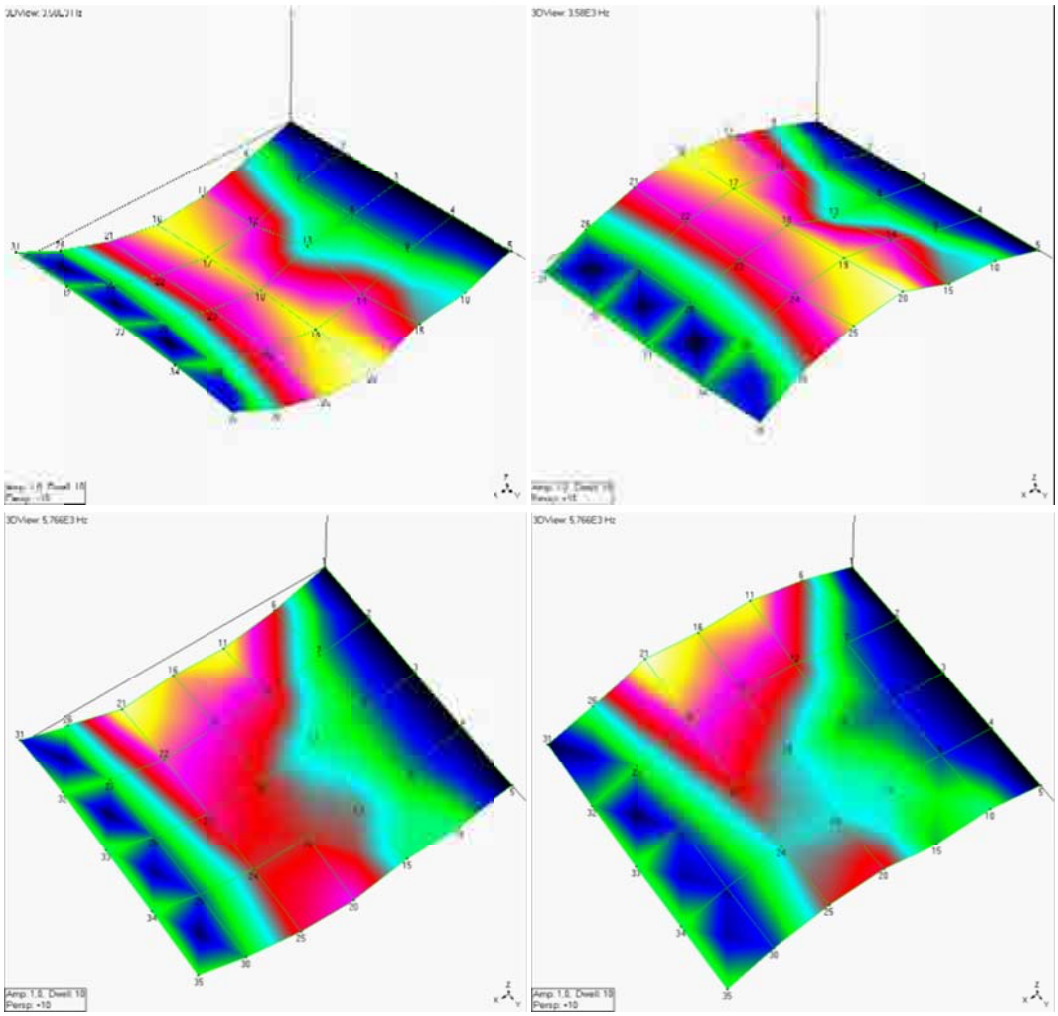

Figure 10.3 - Second bending mode shape for different boundary conditions: *Air* (top two images), *Still water* (the following two images), *Flowing* (next two images) and *Cavitation* (bottom two images).

The visualization of the mode shapes under different conditions permits their comparison.

For the first bending mode, the differences primarily lie in the amplitude of the motion. The simplicity of this mode shape in which no nodal line is present makes further analysis unnecessary.

Both the first torsion and second bending modes introduce a few additional differences among the tested conditions. For instance, for the static cases (*Air* and *Water*), a backwards displacement of the nodal line in the second bending mode was clearly observed, which is consistent with the findings of Lindholm et al. (1965). Figure 10.4 highlights this effect in which the nodal line moves towards the clamped hydrofoil section when submerged in still water.

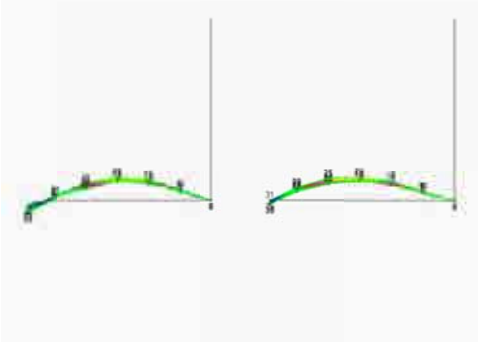

Figure 10.4 - Comparison between lateral views of still water (left) and air conditions (right).

For the first torsion mode, a slight displacement of the nodal line towards the trailing edge is also observed (see Figure 10.5) when submerged in still water. This effect could be due to the asymmetry of the hydrofoil with respect to this nodal line (Figure 7.5), which could also explain why it was not observed by Lindholm et al. (1969) in that all of their work was performed with rectangular beams.

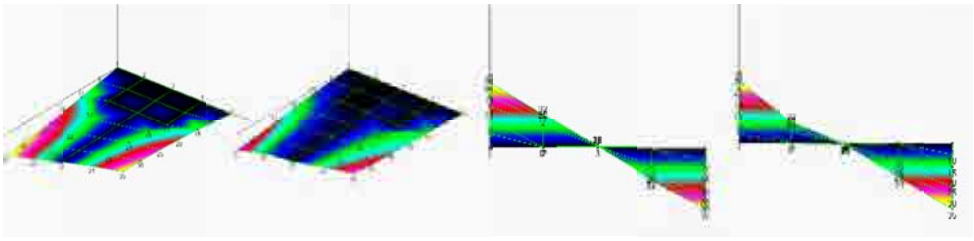

Figure 10.5 - Comparison for f_2 between air (left) and still water conditions (right) for two different views.

Under *Flowing* conditions, both the nodal lines in the torsion and second bending mode move but in the opposite direction, as shown in Figure 10.6, to build a similar shape to that observed in air.

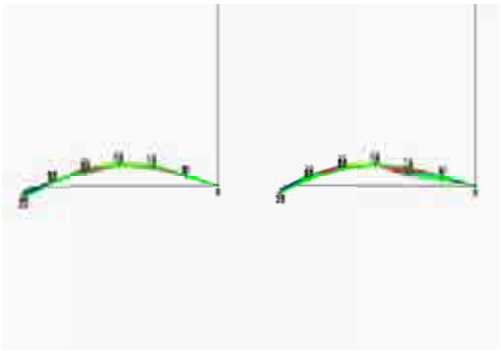

Figure 10.6 - Comparison between lateral views of *Still water* (left) and *Flowing* conditions (right) for the second bending mode.

Finally, the second bending mode shape under a cavitating flow (l/c=0.5) does not appear as clean as those under the other conditions (Figure 10.3), and instead, resembles a slightly coupled mode when animated. In particular, a bending-torsion mode starts to appear, but the bending motion is still recognizable and predominant.

Consequently, in general terms, the mode shapes are considered equivalent in all the experimented conditions, and therefore, the results of the various tests can be compared in terms of natural frequencies.

X.II-Added mass under cavitation conditions

The results of the natural frequency behavior under a cavitating flow are presented in this chapter. First, it is important to recall the added mass coefficient, C_M, obtained with equation (2.25). This coefficient allows us to represent the variation of the added mass due to the effects of other various parameters. The numerical values are summarized in Tables E.5 and E.6 of Appendix E.

To simplify the later discussion, several relationships are shown. Additionally, the natural frequencies of the hydrofoil under static conditions ("*Air*", "*Still water*" and "*Half wetted*") and under non-cavitating flows are also given in Table 10.1 for use as reference values during the comparison. It must be mentioned that the "Half wetted" condition refers to a hydrofoil located horizontally in a half-filled tunnel test section. In this situation, the free surface level reaches the symmetric plane of the profile.

It must be taken into account that the reference frequency, f_{vacuum}, corresponds to the "*Air*" values for all modes. Among all the cases presented in the table, the highest added mass effect is found for the first bending mode, and the lowest is found for the first torsion mode.

	σ	1st bending		1st torsion		2nd bending	
		f_1 [Hz]	C_{M1}	f_2 [Hz]	C_{M2}	f_3 [Hz]	C_{M3}
Air		270.2	0.00	1018.6	0.00	1671.0	0.00
Half Wetted		163.0	1.75	755.0	0.82	1113.6	1.25
Still Water		130.2	3.31	614.8	1.74	886.0	2.56
7 m/s, 1°	3.05	130.6	3.28	621.1	1.69	895.8	2.48
7 m/s, 2°	3.03	130.0	3.32	621.1	1.69	883.2	2.58
14 m/s, 1°	2.48	134.4	3.04	629.3	1.62	913.0	2.35
14 m/s, 2°	2.48	132.0	3.19	634.2	1.58	911.6	2.36

Table 10.1- Natural frequencies and C_M values of the hydrofoil in air, partially (half wetted) and completely submerged in still water, and with no cavitation flows at 7 and 14 m/s for incidence angles of 1º and 2º (in the latter cases the sigma is also indicated).

The added mass coefficients under cavitation conditions have been correlated with the non-dimensional parameter σ/2α in Figure 10.7. As stated previously, the highest added mass values were found for the first bending mode, and the lowest were found for the first torsion mode. This general trend is maintained between 1º and 2º, where we can clearly distinguish between two regions in the profile. For sufficiently high values of σ/2α (typically >0.3), the C_M is nearly constant. Meanwhile, for σ/2α values lower than 0.3, the C_M rapidly decreases.

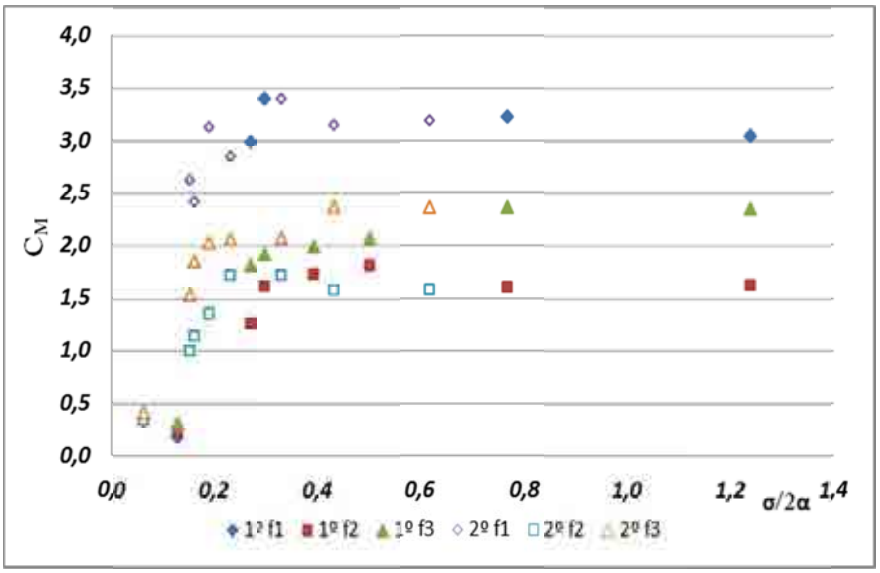

Figure 10.7- Added mass coefficient plotted against the σ/2α parameter for all mode shapes and both incidence angles.

The top view photos (as shown in Figure 7.4) were used to determine the length of the cavitation sheet in each scenario. Due to the 3D effects produced by the lateral walls of the test section, the length was not constant along the span of the profile (see photo sequence in Figure 10.8), and an equivalent constant length was used to compute the cavitation surface ratio (CSR). This equivalent length was the result of equating the real surface of the cavity sheet to a rectangular shape of constant length, $l_{\text{equivalent}}$, along the span.

$$\text{Cavity surface } = l_{equivalent} \cdot span \quad (10.1)$$

$$CSR = \frac{1}{2}\frac{l_{\text{equivalent}}}{c} \quad (10.2)$$

Figure 10.8- A series of pictures representing different cavity lengths at 14 m/s and a 1º incidence angle (above) and a 2º incidence angle (below).

The C_M is plotted against the CSR in Figure 10.9 in which a decreasing trend can be observed. However, the behavior does not show a clear pattern.

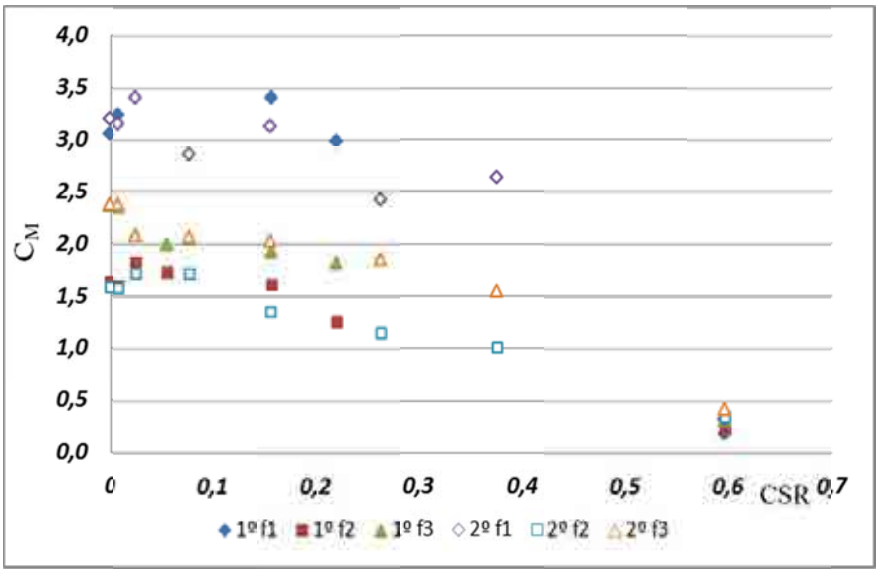

Figure 10.9 - Added mass coefficients plotted as a function of CSR for f_1, f_2 and f_3 at 1° and 2°.

For the results plotted in Figures 10.7 and 10.9, the behavior of the added mass seems difficult to fully explain by only the CSR and **σ/2α.** If we want to analyze the added mass of a hydrofoil under cavitation conditions in detail, we first need to isolate this effect from certain other effects that may influence the results shown in this section. Therefore, we should present certain other variables that could provide a better explanation.

X.III-Effects of lateral gap size on added mass

Because the presence of a near boundary is expected to alter the dynamic response of the hydrofoil, an analysis of the influence of the gap on the natural frequencies of the profile was performed under different conditions, i.e., in *Air*, *Still water* and *9 m/s* flowing water with no cavitation. The results are plotted in Figures 10.10, 10.11 and 10.12. The corresponding numerical values are summarized in Tables E.7, E.8 and E.9 of Appendix E.

Because no clear trend is apparent, no significant effects are expected under the Air condition, as observed in Figure 10.10, in which the C_M values are plotted against the gap size.

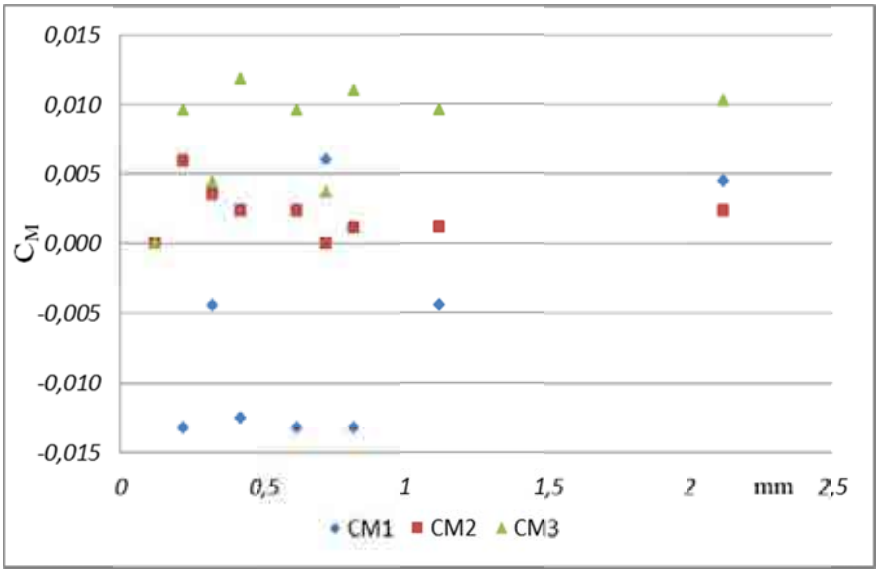

Figure 10.10 - Added mass coefficient plotted against the gap dimension in the *Air* conditions.

Furthermore, as shown in Figure 10.11, when the hydrofoil is submerged in still water, a decreasing trend in the added mass coefficient is apparent for all mode shapes as the lateral gap is increased.

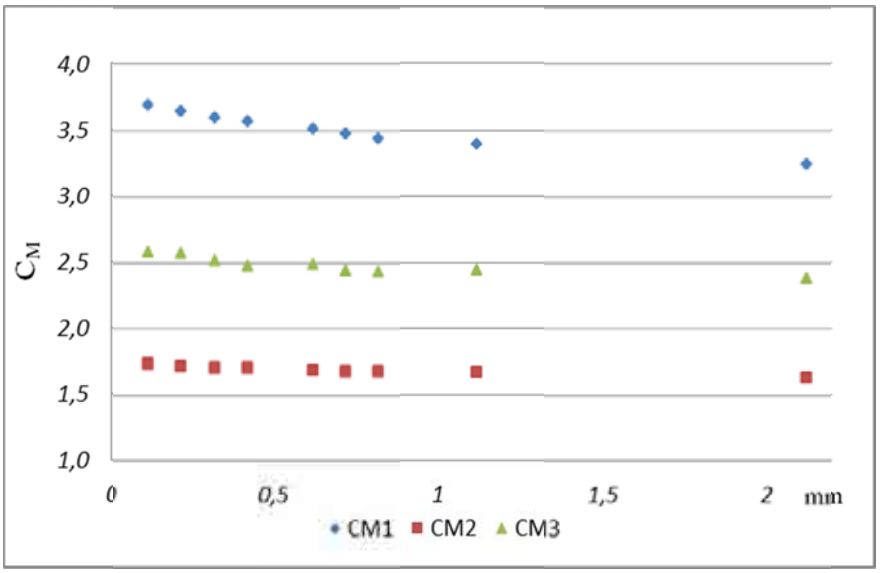

Figure 10.11 - Added mass coefficient plotted against the gap dimension in the *Still water* condition.

We can approximate the trend shown in Figure 10.11 by means of second-order polynomial laws. Table 10.2 summarizes these laws and the correlation coefficient (R^2) for each mode of vibration. A simple method used to analyze the steepness of a parabola is the calculation of the vertex-focus distance, which produces a sense of the zoom level at which the parabola is viewed. In this manner, the equation governing C_{M1} has the lowest distance (lower zoom), and the equation governing C_{M2} has the highest distance. Therefore, the C_{M1} equation represents a steeper parabola than that of C_{M2}. The last term of the equation gives us the limit value of C_M if the gap was infinitely small.

	Trend equation	R^2
C_{M1}	$0.0843x^2 - 0.4119x + 3.7327$	0.9965
C_{M2}	$0.0223x^2 - 0.0965x + 1.7376$	0.9838
C_{M3}	$0.0684x^2 - 0.245x + 2.6001$	0.8996

Table 10.2 - Obtained equations and correlation coefficients for the data points in Figure 10.11; *x* represents the gap size in mm.

The decreasing trend is also observed under the *9 m/s* flowing water condition (Figure 10.12). In this case, more dispersed results are obtained, which could be due to the flow-induced noise that complicates the frequency identification.

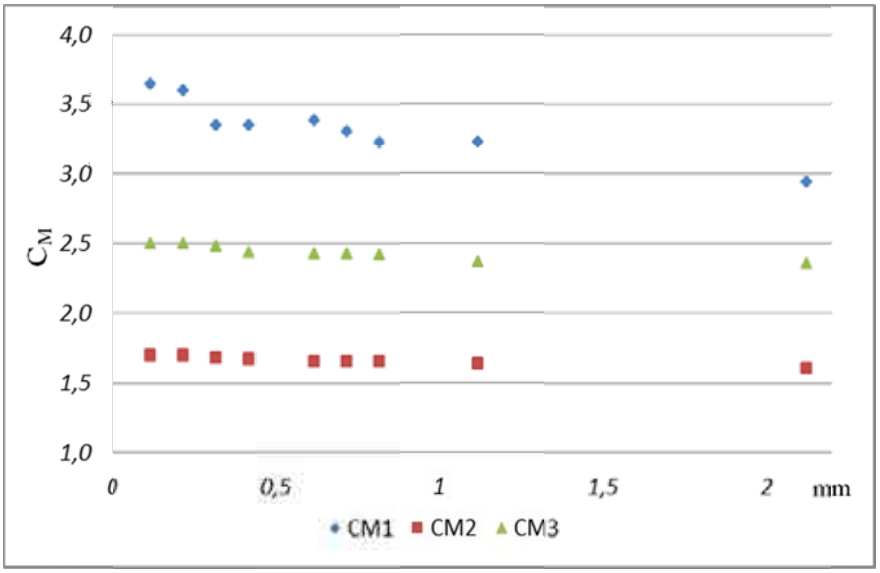

Figure 10.12 - Added mass coefficient plotted against the gap dimension at the *9 m/s* conditions.

These trends are approximated by second-order polynomial laws, as summarized in Table 10.3, which behave in a manner similar to the preceding case in terms of the vertex-focus distance.

	Trend equation	R^2
C_{M1}	$0.1053x^2 - 0.5488x + 3.6442$	0.8798
C_{M2}	$0.0225x^2 - 0.0941x + 1.7067$	0.9717
C_{M3}	$0.0547x^2 - 0.1958x + 2.5297$	0.9408

Table 10.3 - Obtained equations and correlation coefficients for the data in Figure 10.12; *x* represents the gap size in mm.

A comparison between the obtained results in *Still water* and *9 m/s* flowing water is shown in Figures 10.13, 10.14 and 10.15 for the f_1, f_2 and f_3 modes, respectively. As the figure shows, the added mass in the static fluid condition is higher for all mode shapes.

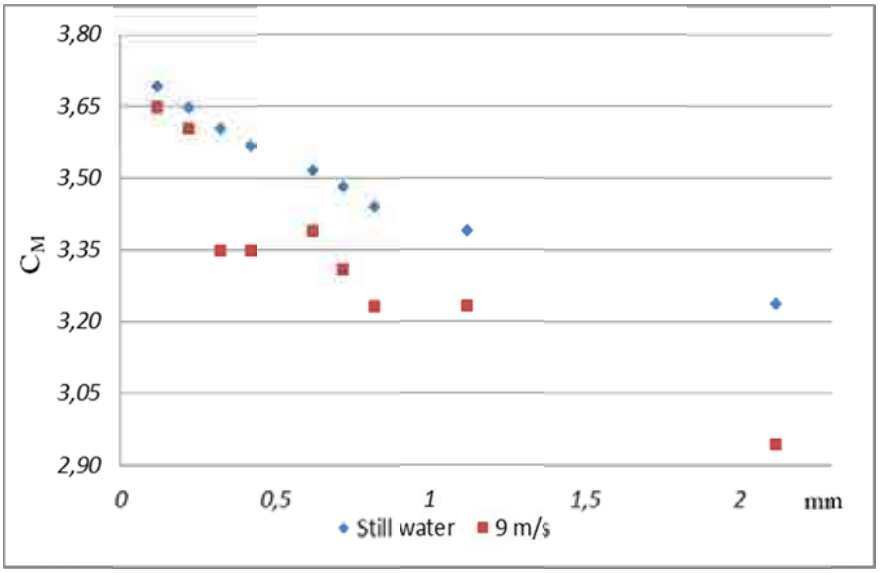

Figure 10.13- Comparison of the added mass results for f_1 in *Still water* and *9 m/s* flowing water.

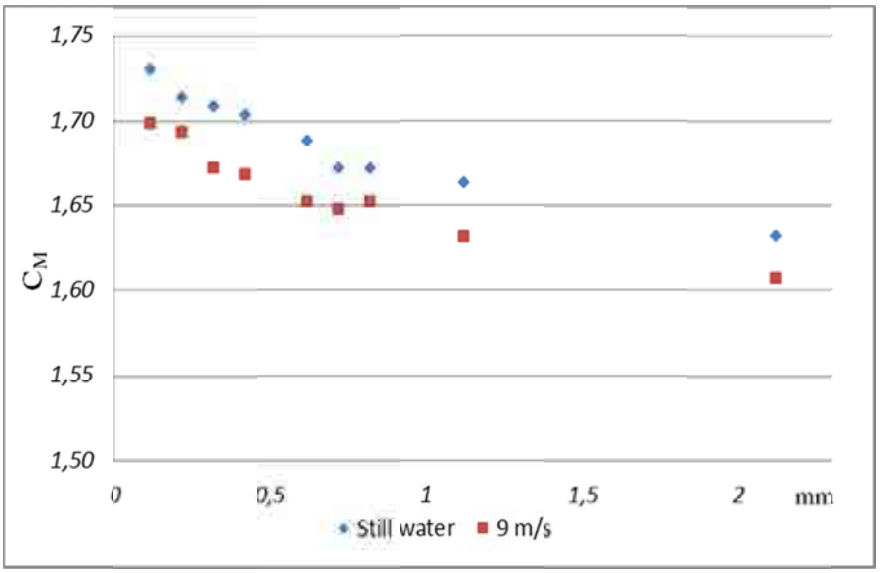

Figure 10.14- Comparison of the added mass results for f_2 in *Still water* and *9 m/s* flowing water.

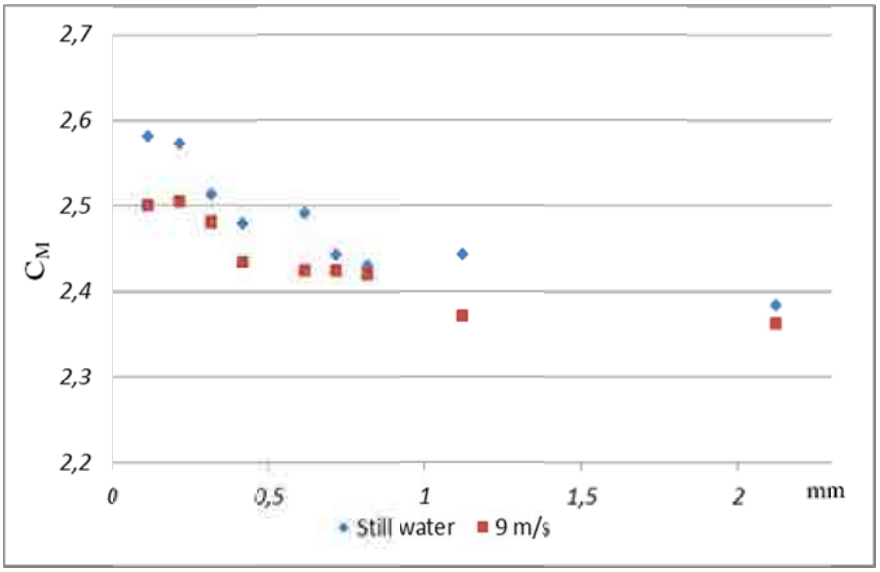

Figure 10.15 - Comparison of the added mass results for f_3 in *Still water* and *9 m/s* flowing water.

X.III.I-Numerical simulation of the lateral gap

To further study this effect and to validate the experimental results, a numerical model was built using Ansys. Figure 10.16 shows the comparison of the numerical and experimental results of the gap effects (as in previous cases, the numerical values are summarized in Appendix E, Table E.10). As shown, the trend of the experimental results is well captured in all the modes of vibration but C_{M3} is significantly underpredicted.

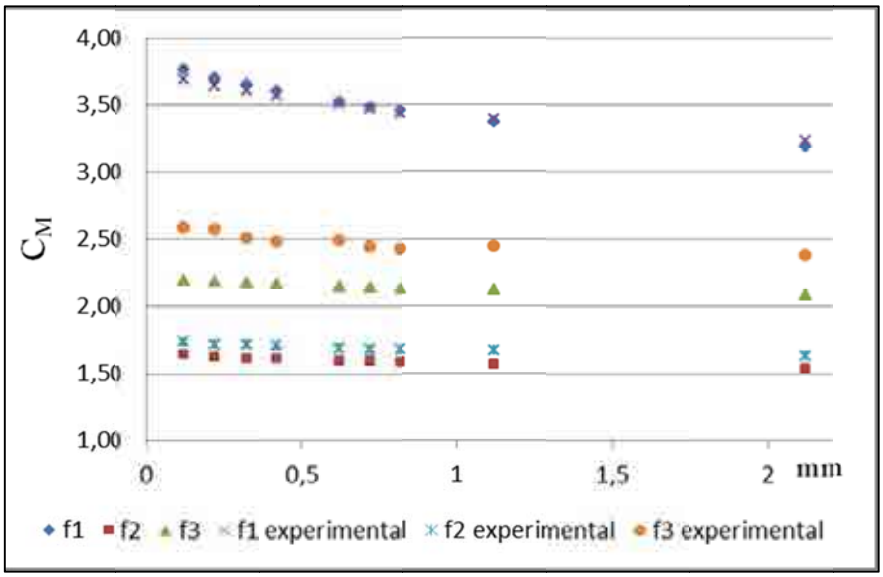

Figure 10.16 - Experimental and numerical C_M values plotted against the gap size.

Figures 10.17 and 10.18 are intended to show the difference in the slope of the trends for the bending and torsion modes. For that reason, f_1 and f_2 are plotted separately. As observed, the bending mode is steeper than the torsion mode, which indicates that it is more significantly affected by the presence of the solid boundary.

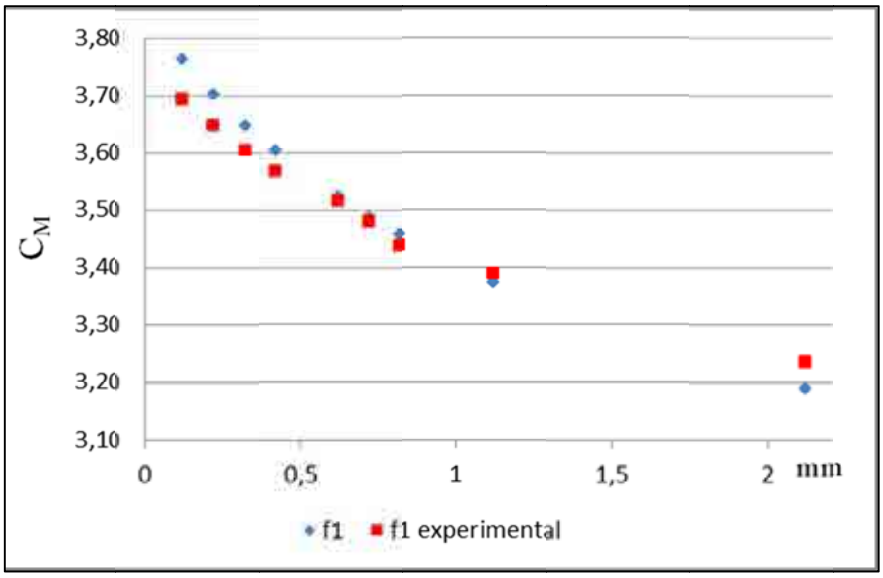

Figure 10.17 - Experimental and numerical C_M values for the first bending mode plotted against the gap size.

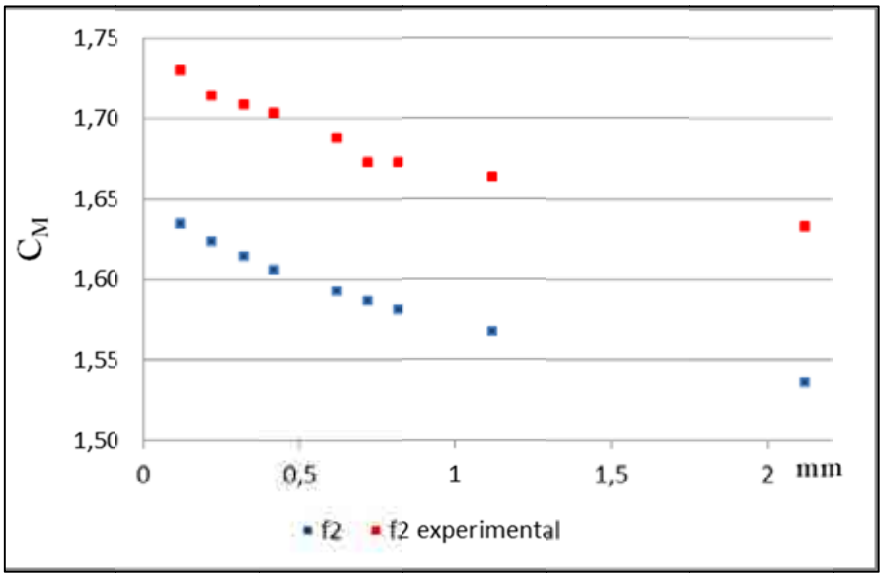

Figure 10.18 - Experimental and numerical C_M values for the first torsion mode plotted against the gap size.

X.IV-Effects of the pressure distribution on the added mass

The results of the modal analyses performed during the tests at different flow velocities and incidence angles without cavitation, as summarized in Table 8.3, are covered in this chapter. Each mode shape is presented separately. Tables E.11, E.12, E.13, E.14 and E.15 of Appendix E contain the corresponding numerical values of all tests that are graphically shown in this section.

The added mass coefficients for each mode shape are plotted as a function of flow velocity and incidence angle in Figures 10.19, 10.20 and 10.21.

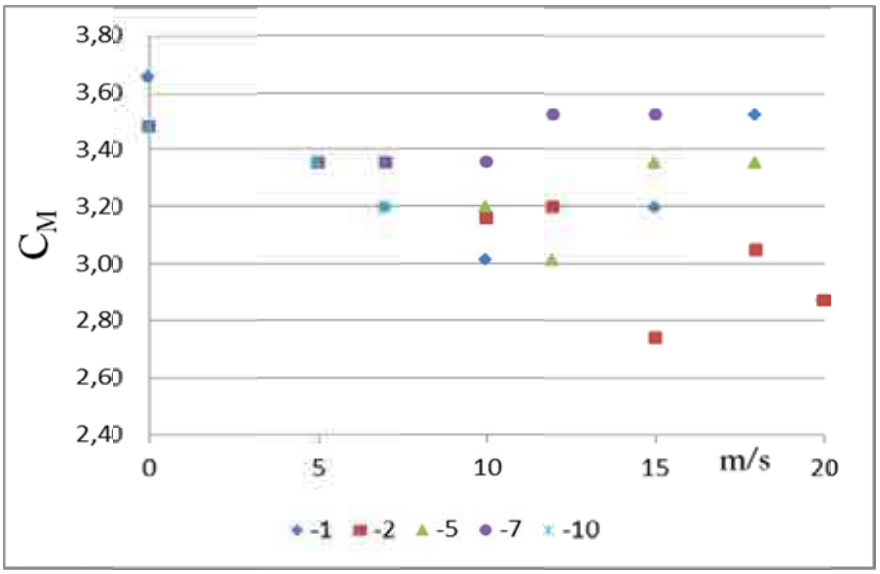

Figure 10.19 - Added mass coefficient for f_1 plotted as a function of the flow velocity for different incidence angles.

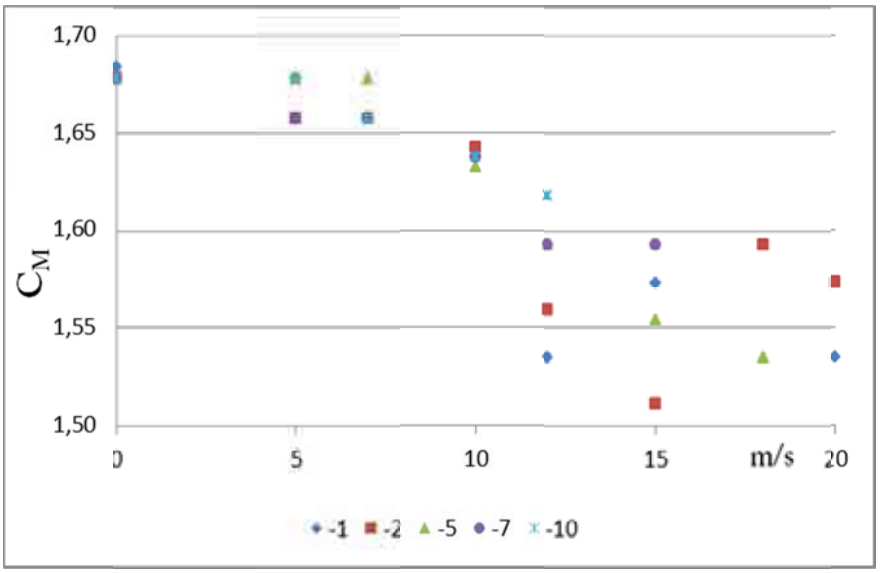

Figure 10.20- Added mass coefficient for f_2 plotted as a function of the flow velocity for different incidence angles.

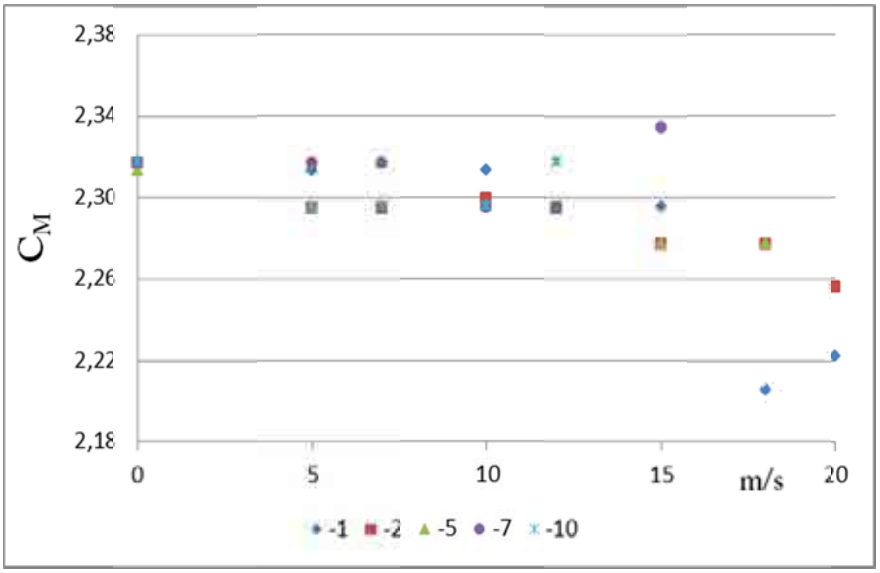

Figure 10.21- Added mass coefficient for f_3 plotted as a function of the flow velocity for different incidence angles.

As observed, no clear trend can be identified among the different modes. Only the torsion mode appears to show a decreasing profile with the flow velocity for all incidence angles under study. However, the large dispersion of these results complicates the analysis.

Discussion and comparison

This chapter discusses the results presented in chapter X to establish a link between them to simplify the comparison and analysis. The effects of cavitation on the added mass and the main influencing factors will be outlined from this analysis.

XI.I-Interpretation of added mass effects under cavitation conditions

The experimental added mass coefficients obtained for the three modes of vibration under conditions of different attached cavities and supercavities (see Table 10.1 and Figures 10.7 and 10.9) prove that the presence of a two-phase flow around the hydrofoil has a significant effect on its dynamic response. Nevertheless, from the observation of the C_M trends as a function of $\sigma/2\alpha$ and/or CSR, it can be concluded that the effects are not fully explained only by these variables.

The added mass is a function of the fluid density and the amplitude and direction of its vibration, among other parameters (Blevins 1979, equation 2.44), which means that it is a function of the fluid density and the mode shape of vibration under study. In our particular test conditions, the relevance of the mode shape is expected to increase because the presence of the cavity acts partially over the structure surfaces. To study this assumption, the experiments of Lindholm et al. (1965) with partially submerged rectangular plates in still fluids could act as a starting point due to their strong analogy with the case of a partial cavity attached to a surface. Therefore, we decided to study these effects with an analogous experiment and a numerical simulation.

Partially submerged hydrofoil

In this section, the results of step-by-step submergence of the profile are presented. Because the profile is not symmetric, a comparison of the hydrofoil is also given depending on the orientation.

The added mass coefficient is plotted against the submergence percentage in Figures 11.1 and 11.2. In the first figure, the profile is oriented with the leading edge (LE) towards the bottom of the tunnel test section, and in the latter, with the trailing edge (TE) towards the bottom of the tunnel test section.

It is clear that as the hydrofoil is submerged, the added mass increases for all modes, but the evolution differs between the bending and torsion modes. For bending modes, a growing trend is observed for any submergence level whereas for the torsion mode, the added mass displays a nearly constant zone between 40% and 60%. In addition, the equations that best fit the experimental results are presented for both bending modes and orientations with high correlation, as observed in Table 11.1 and 11.2.

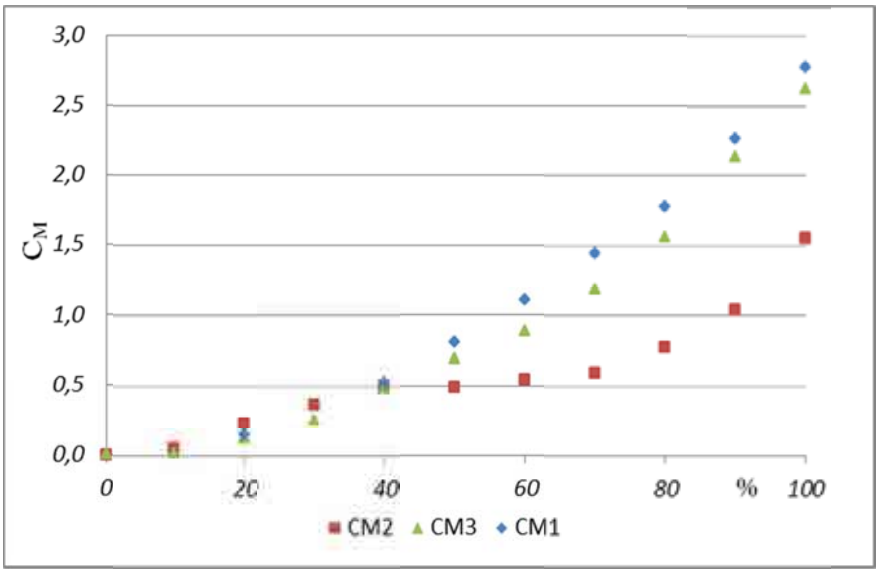

Figure 11.1- Added mass coefficient plotted against the submergence percentage when the profile is vertically oriented with the leading edge at the bottom.

	Trend equation	R^2
C_{M1}	$0.0002x^2 + 0.0052x - 0.0514$	0.9993
C_{M3}	$0.0003x^2 - 0.0008x + 0.0162$	0.9963

Table 11.1 - Obtained equations and correlation coefficient for both bending modes in Figure 11.1; *x* represents the submergence percentage.

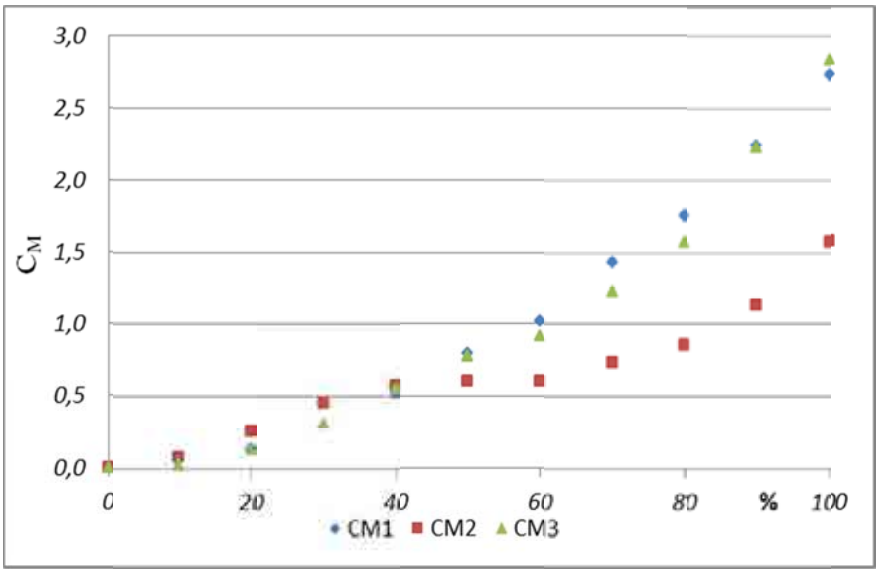

Figure 11.2 - Added mass coefficient plotted against the submergence percentage when the profile is vertically oriented with the trailing edge at the bottom.

	Trend equation	R^2
C_{M1}	$0.0002x^2 + 0.004x - 0.0243$	0.9989
C_{M3}	$0.0003x^2 - 0.0011x + 0.0417$	0.9905

Table 11.2 - Obtained equations and correlation coefficient for both bending modes in Figure 11.2; *x* represents the submergence percentage.

As mentioned previously, the profile is not symmetric with respect to its torsional axis. The results for f_2 when the leading edge or the trailing edge is submerged are compared in Figure 11.3. As shown, the trailing edge orientation experiences greater added mass effects than the leading edge orientation.

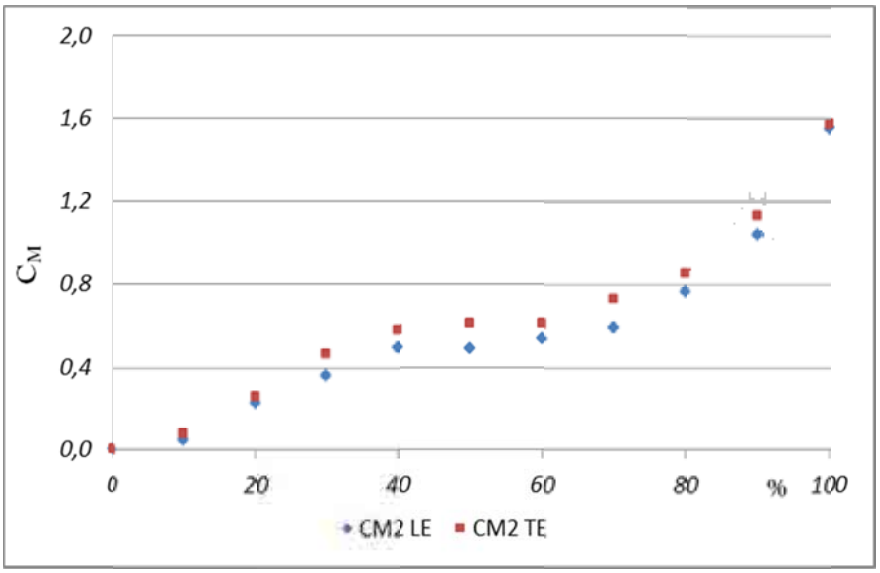

Figure 11.3 - Added mass coefficients for f_2 plotted against the submergence percentage. Orientation comparison.

Numerical simulation

The added mass coefficients obtained from the numerical simulation are compared with the experimental values in Figures 11.4 and 11.5. As shown in the figure, the numerical results are similar to the experimental results, except for the second bending mode in the range of 70% to 100% submergence.

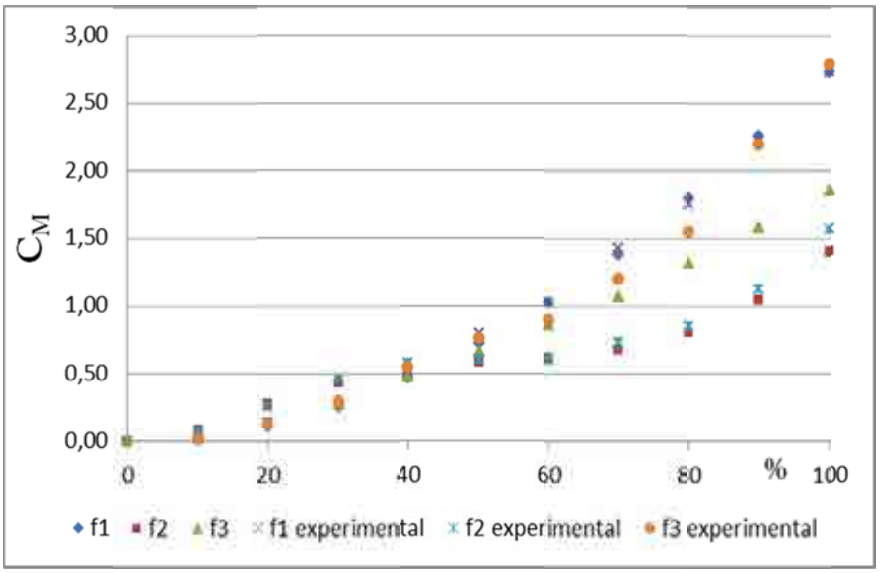

Figure 11.4 - Experimental and numerical C_M values of the hydrofoil partially submerged in water. Orientation of the profile: trailing edge submerged.

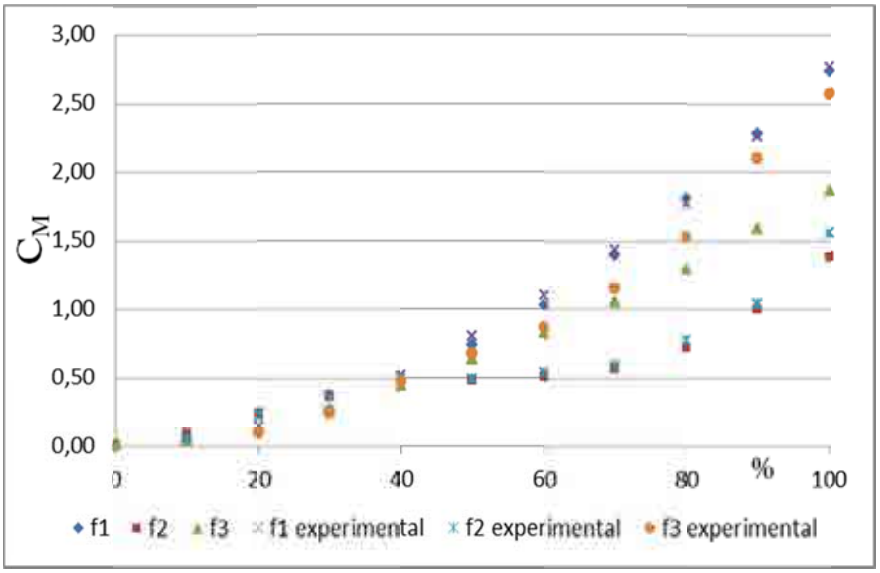

Figure 11.5 - Experimental and numerical C_M values of the hydrofoil partially submerged in water. Orientation: leading edge submerged.

To compare the effects of the profile orientation, f_2 was chosen because this mode shape is expected to enhance these effects. Figure 11.6 shows the comparison between the numerical results for both orientations. As observed in the experimental results (Figure 11.3), the trailing edge orientation experiences a greater added mass.

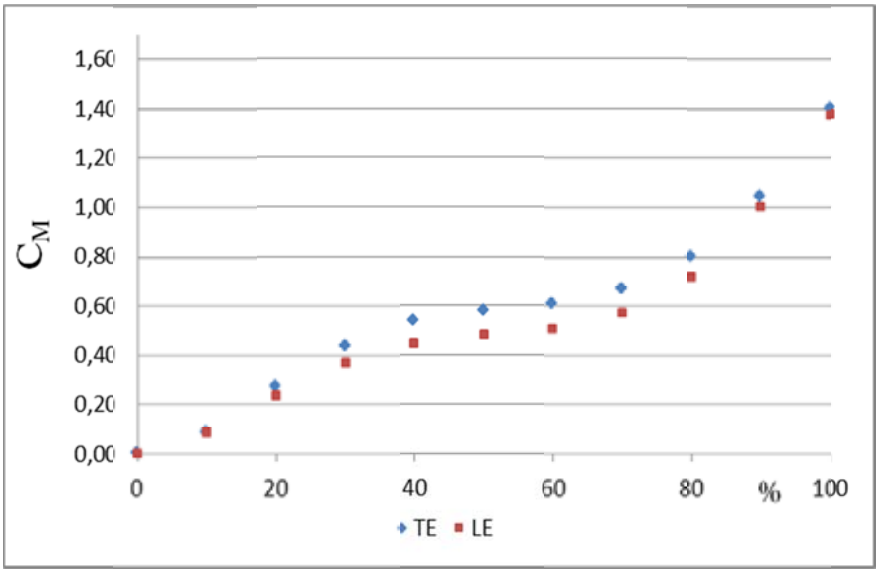

Figure 11.6 - C_M values for f_2 plotted against the submergence percentage. Orientation comparison.

As observed in Figures 11.1, 11.2 and 11.3, the variation of C_M with the submergence level is clearly related to the fluid entrained by the mode shape motion.

In particular, if we focus on the torsion mode, the shape of the C_M results versus the submergence level depicts a plot of the motion itself. The extreme locations where most of the fluid is accelerated produce the most significant increase in the added mass. Meanwhile, the center of the hydrofoil does not entrain much fluid due to the presence of a nodal line parallel to the free surface. Therefore, this zone is represented by a nearly constant C_M line.

Similarly, it would be expected that for bending modes, the variation of C_M is basically constant throughout the process due to the relative position of the hydrofoil. Surprisingly, the effects on the added mass are better captured with a second-order polynomial law (see Tables 11.1 and 11.2). As observed in Figures 11.1 and 11.2, for low submergence levels, the C_M increase is quite weak whereas it is far steeper for high levels.

For the numerical model in general, the trends are well simulated even if f_3 is overestimated (Figures 11.4 and 11.5). In particular, the torsion mode shows its characteristic shape, and the effect of the orientation of the profile is correctly solved (Figure 11.6).

The well-known fact that the added mass effect on a submerged structure depends on the particular mode shape that is excited, as proved by Yadykin et al. (2003), suggests that the hydrofoil deformation plays an important role in the added mass effect as we can also deduce from these results. Therefore, if cavitation occurs, it is not only the extent of surface covered by cavitation, accounted by the CSR, but also its location relative to the hydrofoil deformations that must be considered. Moreover, the mean density of the fluid inside the cavity in contact with the deforming structure should be also relevant. Consequently, the so-called entrained mass (EM) should be computed to better understand how the flow density and its location relative to the hydrofoil displacement influence the added mass effect.

XI.II-Entrained mass (EM)

The EM_i is defined as the total fluid mass, m_i, displaced by the hydrofoil motion relative to the maximum normal surface displacement, $\Delta Y_{\mathrm{max}i}$, and is calculated as shown in equation (11.1) where j is the number of considered flow regions and i indicates the particular mode of vibration. This equation takes into account the mean density, $\bar{\rho}_j$, and

the mean displacement of the contact surface, $\bar{d}_j$, of each type of region that can be obtained after discretization of the fluid domain and the calculation of the local displacements at each node by equation (11.2), where N is the total number of nodes.

$$\mathrm{EM}_i = \frac{m_i}{\Delta Y_{\max i}} = \sum_j \bar{\rho}_j \left(\bar{d}_j \cdot \mathrm{AREA}_j\right) \quad (11.1)$$

$$\bar{d}_j = \sum_k^N \frac{|\Delta Y_k|}{N|\Delta Y_{\max i}|} \quad (11.2)$$

From the cavitation top views (Figure 11.7), the area covered by the whole sheet cavity can be adequately identified and delimited. However, two different cavity morphologies can be distinguished depending on the visual aspect. For instance, on the top view in Figure 11.7, the cavity appears to be quite transparent on both lateral sides while looking foamier in the central region. Increase transparency indicates a high void ratio that could be due to the 3D effects of the tunnel test section lateral walls. These effects suggest that the lateral sides of the cavity closure are not parallel to the spanwise direction, but oblique. Consequently, the reentrant jet direction is inclined towards the center of the leading edge and its component that is parallel to the flow is lower.

Under such conditions, the cavity behavior is expected to exhibit a more stable behavior, and the amount of vapor phase is also increased (Franc and Michel, 2004). Therefore, these zones can be characterized with a higher void ratio. The central area where the cavity appears foamy is composed of the shedding of a mixture of small cavitating vortices/bubbles with water. This zone presents a more heterogeneous flow and a lower void ratio. The portion of the hydrofoil surface downstream of the closure region has been considered to be full of pure water, although some shed vortices can still be observed

on it. In summary, three hydrofoil regions covered by different fluid flow densities were distinguished simply by visual observation of the photographs. One such example is shown on the right side of Figure 11.7, where the transparent cavity is shown in blue, the foamy cavity in green and the no cavitating flow in black. This region identification is consistent with the work performed by Stutz and Reboud (1997) that suggests a cavitating flow pattern composed of different characteristic areas for sheet cavitation in a cavitation tunnel Venturi-type test section. They reported that the reverse flow due to the re-entrant jet decreases the void ratio along the cavity and that the maximum measured void ratios can reach approximately 0.8.

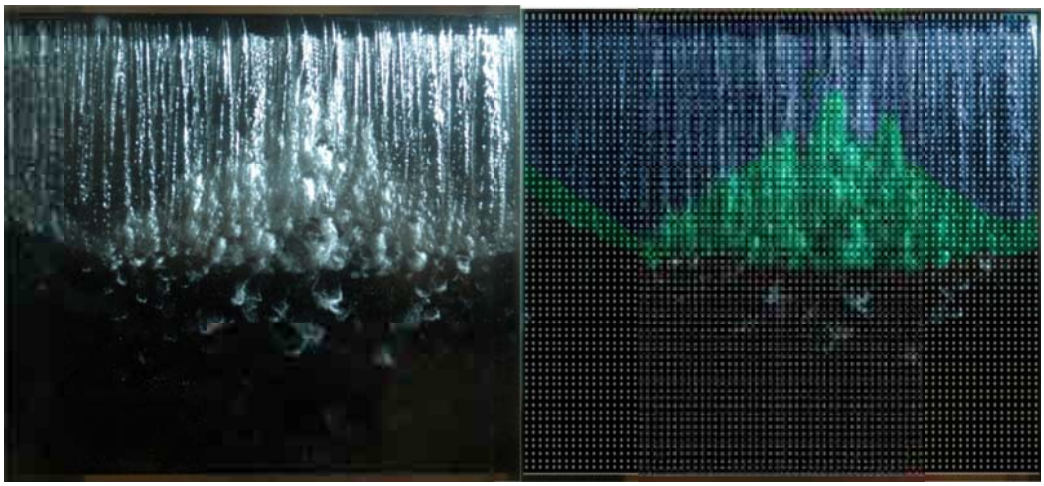

Figure 11.7- Left) Top view photograph of sheet cavitation on the hydrofoil suction side (flow from top to bottom). Right) Example of zone identification with Ansys node discretization superimposed.

For our calculations, cavitation was considered to be a biphasic mixture of water vapor and liquid with a pure water vapor density of $1.74 \cdot 10^{-2}$ kg/m^3 (saturated vapor at 20°C) and a pure liquid water density of 1000 kg/m^3. A void ratio of 0.8 was given to the transparent cavitation regions and a value of 0.3 to the foamy regions. These values were selected to force the linear regressions shown in Figure 11.9 to pass as close as possible to

the origin since the entrained mass is expected to be negligible for the condition in air. Anyhow, these two values are also consistent with the work performed by Stutz and Reboud (1997).

Based on the mode shape visualization results, we assumed that the mode shapes in air were analogous to those under all tested conditions. The numerical model was used to simulate the three mode shapes to obtain a better spatial resolution over the hydrofoil surface, the results of which could be used to perform the subsequent node-region assignation. It must be noted that only 26 measurement points were used in the mode shape visualization, and this number was considered insufficient for an accurate approximation. All of the mode shapes obtained by numerical simulation are shown in Figure 11.8.

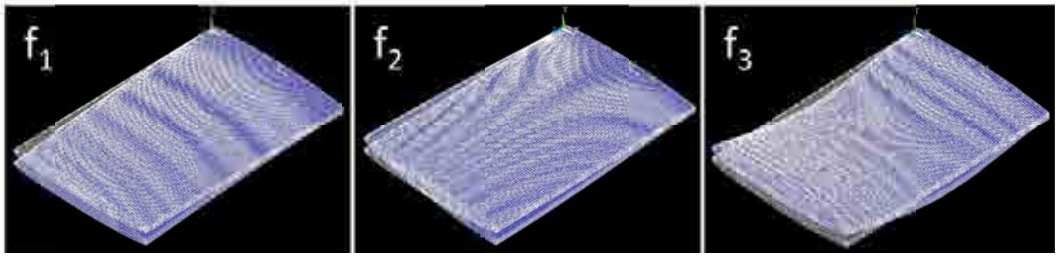

Figure 11.8- Simulated mode shapes for the first bending f_1 (left), torsion f_2 (middle) and second bending f_3 (right) modes.

The normal displacements of the element nodes on the top surface, $|\Delta Y_k|$, were obtained from the FEM solution. Next, taking advantage of the domain discretization, the positions of all element's nodes were superimposed over the top photographs, as shown on the right side of Figure 11.7, such that each point corresponded to a node with a known absolute displacement. For simplicity, the geometry was assumed to be a flat plate. After dividing the total surface into three regions, each element node was assigned to its corresponding area with a given mean density. For each region, all displacements were

averaged and normalized by the maximum normal displacement found for the total hydrofoil surface (Equation 11.2), which avoids the amplitude differences between the air and cavitating conditions. Finally, equation (11.1) was developed to calculate the approximate entrained mass $\mathrm{EM_i}$ by considering the so-called "trans" (for transparent), "foamy" and "water" regions. The first two terms correspond to the cavity and the last corresponds to the flow outside the cavity.

$$\mathrm{EM}_i = \left[\bar{\rho}_i \cdot \bar{d}_i \cdot \mathrm{AREA}\right]_{\mathrm{trans}} + \left[\bar{\rho}_i \cdot \bar{d}_i \cdot \mathrm{AREA}\right]_{\mathrm{foamy}} + \left[\bar{\rho}_i \cdot \bar{d}_i \cdot \mathrm{AREA}\right]_{\mathrm{water}} \qquad (11.3)$$

Finally, only the results for f_2 and f_3 have been considered in the final discussion of the correlation between C_M and EM shown in Figure 11.9. During the tests, it was observed that during f_1 identification, the hydrofoil tip touched the lateral wall of the test section under certain flow conditions.

XI.III-Final considerations

From the results and based on the topics already discussed, the final considerations are separately examined in this section.

XI.III.I-Entrained mass

As previously explained, the added mass depends on several parameters. It was expected that the correlations of the added mass coefficients with σ/2α and CSR shown in Figures 10.7 and 10.9 could not explain the phenomenon in detail. It seems reasonable that as the cavity increases (CSR), the added mass is decreased. The variation in the added mass is unknown because this process must take into account the mode shape, the location of the cavity and its inner morphology. The EM parameter explained previously attempts to take all of these variables into account by assuming an average density of the sheet formed

by different areas and considering the deflection of the structure surface in each mode shape. The C_M as function of the EM for f_2 and f_3 has been plotted in Figure 11.9 with the corresponding equations of the obtained trends.

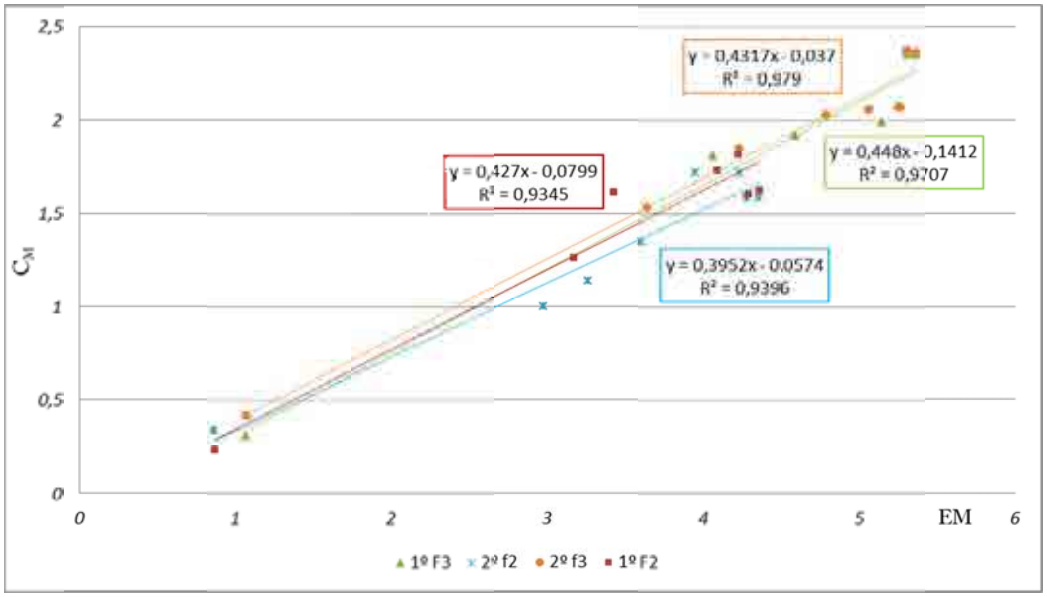

Figure 11.9- Added mass coefficients as a function of entrained mass for f_2 and f_3 at 1° and 2°.

The linear trend shown in Figure 11.9 assists the reader in understanding the added mass phenomenon under cavitation conditions. Moreover, based on the obtained results, a single regression could be presented because the all of the data appear to collapse to the same line. In Table 11.3, the equations presented in Figure 11.9 are indicated along with the average linear regression, which attempts to predict the C_M for any mode of vibration.

	Equation
1º f_2	$C_{M2} = 0.427EM - 0.0799$
1º f_3	$C_{M3} = 0.448EM - 0.1412$
2º f_2	$C_{M2} = 0.3952EM - 0.0574$
2º f_3	$C_{M3} = 0.4317EM - 0.037$
Averaged	$C_{Mi} = 0.4255EM - 0.0789$

Table 11.3- C_M regressions for different mode shapes and the averaged C_M regression.

It seems reasonable that if the added mass is the inertia of the fluid that the structure has to accelerate during its vibration motion; one should know the density properties of such fluid. It makes no difference when dealing with a biphasic fluid. As stated by Blevins (1979) that *the added mass is not the mass of the fluid entrained by the motion of the submerged body* which is true, we can now add: *but they are lineally related*.

Observing Figures 10.7 and 10.9 and comparing f_1 and f_3, the added mass is greater for lower modes, as previously stated by Yadykin et al. (2003). This result is consistent with the EM approach because the lower the mode, the higher the total fluid displacement.

A surprising result is the low value of the added mass for the supercavitation case for all mode shapes, assuming that most of the pressure side of the hydrofoil remains in contact with liquid phase water. In fact, compared with its static analogous situation (*Half wetted*), a reduction of 90% occurs for f_1, 72% for f_2 and 75% for f_3. Such significant differences may be explained by the presence of surface waves in the static case. These surface waves observed during the experimental tests should be seen as an extra added

mass. Assuming that the work performed by the structure is transformed into kinematic energy within the fluid, potential energy also exists in the presence of surface waves, which plays a role in adding additional inertia to the balance. This observation is a possible reason why the increase in the natural frequencies of this case falls below the expected value of $\frac{f_{\text{air}}-f_{\text{water}}}{2}$.

XI.III.II- Gap effect

The effect of the lateral gap has been studied to analyze its behavior and detect any possible effect that could be masked in the results of the main test. The lateral gap, as shown in Figure 10.10, has no significant effect in air. However, under both still and flowing water conditions, it has a measurable effect on the natural frequencies of the hydrofoil (Figures 10.11 and 10.12). This observation can be explained from an energetic point of view; the confined fluid within the gap experiences a greater increase in its velocity (kinematic energy) with respect to an unbounded fluid due to the presence of the wall, and consequently, the C_M also increases. As the solid-wall distance is increased, the situation tends progressively to the unbounded case.

The acceleration of the fluid in the gap is obviously dependent on the relative movement of the structure with respect to the wall (mode-shape-dependent). In our particular situation, the effects of the gap were expected to be low because the movement of the hydrofoil is positioned essentially parallel to the wall for all modes under study. However, we can observe from Figures 10.11 and 10.12 that the bending modes are affected to a greater extent than the torsion modes due to the higher fluid accelerations induced by the motion of the hydrofoil tip. This result is also highlighted by Figures 10.17 and 10.18 in which the slope of the C_M profile is clearly steeper for the bending mode.

The C_M values under flow conditions are slightly lower than those in static conditions (Figures 10.13, 10.14 and 10.15). This result might be explained by the fact that within the gap, the flow velocity could produce a local depression, which may act as an axial load over the hydrofoil and increase its natural frequencies (Parker and Mole Jr., 1991 and Bukaian, 1990). It was verified during the experiments that the test section walls could be deformed by the operating pressure; for this reason, in this particular study, the pressure was maintained as a constant to avoid including additional uncertainties.

If we assume that the natural frequencies of the hydrofoil with a 2.1-mm gap are the same as those of an unbounded hydrofoil, the presence of the solid wall at lower distances increases the added mass for each mode shape, as observed in Table 11.4, in which the C_M *wall effect* denotes the increase of the added mass from the unbounded case. It must be mentioned that the unbounded C_{M1} value under flow conditions seems anomalous because it is too low. This anomaly results in a greater increase of C_M via the effect of the wall.

In summary, it can be concluded that due to the gap effect, the actual C_M-EM profiles of Figure 11.9 for an unbounded hydrofoil would appear as two parallel lines below those represented because the gap effect might also exist during the cavitation conditions.

	f_1			f_2			f_3		
	C_M unbounded	C_M wall effect	ΔC_M (%)	C_M unbounded	C_M wall effect	ΔC_M (%)	C_M unbounded	C_M wall effect	ΔC_M (%)
Still water	3.24	0.45	13.9	1.63	0.1	6.1	2.38	0.2	8.4
9 m/s	2.94	0.71	24.1	1.61	0.09	5.6	2.36	0.14	5.9

Table 11.4- C_M's for unbounded hydrofoil and the effect of the lateral wall on it.

The effect of the gap has not been experimentally tested under cavitating conditions. Nevertheless, no significant differences from the observed effects under noncavitating conditions are expected unless the cavitation also takes place within the gap. This situation may greatly modify the results because the effect of the gap disappears when filled with gas, as shown in Figure 10.10.

XI.III.III- Pressure distribution effect

Because cavitation not only changes the flow field in terms of the phases but also changes the pressure distribution around the structure, we wanted to separate both phenomena and determine if the effects observed on the main test were due to the former effect, the latter effect or a combination of both effects. Moreover, the slight increase in the natural frequencies observed between the *Still water* and non-cavitating conditions of Table 10.1 attracted our attention.

As observed in the behavior of the C_M plotted against the mean flow velocity and incidence angle presented in Figures 10.19, 10.20 and 10.21, it is difficult to identify a general trend. In Figure 10.20, it appears that an increase of velocity induces a decrease of the C_M. However, the dispersion of the results makes it difficult to verify this observation. In contrast, the results are undetermined for both bending modes.

When the flow velocity is increased, both an increase in the added stiffness (Reese 2010) and in the damping (Seeley et al. 2012) could be expected. These two different phenomena produce opposite effects on the natural frequencies of a body, as deduced from equations 2.8 and 2.3, respectively. However, Seeley et al. (2012) previously stated that despite the linear increase of the damping ratio, this situation produced no substantial effect on the natural frequencies. Regarding the increase of stiffness, it has to be taken into account that bending and torsional stiffness are different properties of a body and maybe, due to the position of the hydrofoil with respect to the flow, the torsional stiffness is more affected and hence, we can observe a relationship. For instance, during the mode shape visualization, we were surprised to obtain higher amplitudes for f_2 under flow conditions than in still water. This phenomenon may indicate that the flow could vary the torsional stiffness of the hydrofoil (increasing it, in this case) and therefore, an effect would be observed in the C_M vs. velocity plot shown in Figure 10.20.

PART IV: CONCLUSIONS

In this part, the main conclusions of this study are discussed. Additionally, future research is also proposed to highlight the aspects of this work that should be improved for its logical continuation.

Specific Conclusions

Selected important conclusions can be drawn with respect to different issues that have appeared in the present work.

XII.I-Excitation system

The PZT patch technology has demonstrated reliable performance as both an excitation system and as a sensor device. Their geometry, physical properties and ease of installation make these devices suitable for an onboard solution. Although the excitation produced by the patches was sufficient for the planned tests, a more energetic solution may have been a better choice to produce cleaner results under the inherently noisy environment of the experiments with cavitation.

XII.II-Experiments

XII.II.I-Effects of cavitation on the added mass

The effects of sheet cavitation and supercavitation on the added mass of a hydrofoil have been demonstrated. By measuring the dynamic response, the current work has shown how the natural frequencies of the structure are increased when the cavity size is enlarged. Moreover, a linear relationship has been found between the added mass and the mass of fluid entrained by the hydrofoil motion under vibration.

XII.II.II-Effects of the flow conditions on the structural mode shapes

Mode shape identification, visualization and comparison have been performed under different flow conditions. The results show slight differences, primarily for the torsion and the second bending modes. These differences are related to the position of the nodal lines for the *Air*, *Still water* and *Flowing* conditions without cavitation. However, when an attached cavity of approximately 50% of the chord is present, the f_3 animation resembled a bending-torsion coupled mode. Nevertheless, the expected bending movement still prevailed.

XII.II.III-Effects of boundary conditions on the added mass

The effect of a near solid wall on the added mass has been proven. The natural frequencies of the hydrofoil decreased due to the proximity of the lateral wall. In this context, we could also observe how this decrement depended on the mode shape and hence on the direction of vibration. Those modes that induced acceleration components in the direction perpendicular to the wall (the bending modes, in this case) experienced a steeper decrement in their natural frequencies.

XII.II.IV-Pressure distribution effect on the added mass

The effects of pressure distribution on the added mass are not yet clear. The proposed tests for this study could not clearly explain these results because they most likely involved other effects. However, because this variable is expected to influence the stiffness of the body and consequently the added mass coefficient within the velocity range under study, additional effort should be focused this topic in the future.

XII.III-Numerical simulation

The model developed with Ansys software has demonstrated an ability to calculate the natural frequencies of a hydrofoil submerged in still water. Moreover, it was also able to capture the effects of two different boundary conditions:

- A near solid wall
- A free surface in a partially submerged hydrofoil

For the first case, the proposed model showed good agreement in terms of the added mass trend but significantly under-predicted the second bending mode results.

For the second case, an experimental test was also performed to reproduce the work of Lindholm et al. (1965) but with a partially submerged hydrofoil. In general terms, the numerical-experimental comparison showed good agreement. Nevertheless, for deep submergence levels, the second bending mode accuracy decays. In this case, such differences seem to be provoked by experimental uncertainties, and the numerical values appear more reliable.

XII.IV-Summary results

The most relevant experimental results are quantified in this section.

When the profile is submerged in still water, the maximum C_M value for the hydrofoil is 3.31 for f_1, 1.74 for f_2 and 2.56 for f_3. As the cavitation increases, the C_M decreases. The reduction of C_M (which is also mode-dependent) can reach up to 95% for f_1, 87% for f_2 and 88% for f_3 under supercavitation conditions. However, for the half-wetted case in static flow conditions, the reduction in terms of C_M is 47% for f_1, 53% for f_2 and 51% for f_3.

The linear regression that predicts the C_M in terms of the entrained mass of fluid under cavitation conditions for any mode shape of vibration results in:

$$C_{Mi} = 0.4255EM_i - 0.0789$$

The presence of a nearby solid wall significantly increases the added mass of the structure. For a hydrofoil-wall distance of 0.12 mm, the increase of C_M ranges from 5.6% for the torsion mode to 13.9% for the first bending mode, also depending on the flow conditions.

Prospective

With respect to the obtained results, several issues could be improved to better characterize the different phenomena investigated in the present work. Additionally, a proposal for a future project is also outlined to continue this research line.

XIII.I-Improvements

a) Measure the density of the cavity with precision by means of a densitometer.
b) Measure the actual displacements of the entire hydrofoil surface by means of a scanning vibrometer with a sufficient density of measuring points.
c) Measure the pressure on the hydrofoil surface.
d) Perform a two-way coupled numerical simulation with a CFD tool.
e) Perform a similar study on a 2D hydrofoil clamped on both sides (no gap)

The density of a cavity varies significantly depending on its type, the flow conditions and the structure to which it is attached. Moreover, the local density within a cavity can adopt a wide range of values, according to Stutz and Reboud (1997), Stutz and Legoupil (2003) and Coutier-Delgosha et al. (2006). Although it takes into account the different regions within the cavity, the approximation performed in the present work uses averaged values, which could result in a lack of accuracy. The EM concept requires a well-defined inner structure of the cavity, which is only possible if the local density is known.

In the present work, the (relative) displacements of the hydrofoil surface have been obtained by means of the numerical model. The difficulty of measuring the actual

hydrofoil displacements under cavitating flows has made it unfeasible to produce a sufficiently dense net of measuring points that could be assigned to the different cavity regions. In this context, the use of a multipoint or scanning LDV could be of major interest to obtain the absolute displacement magnitudes of a grid of points. The EM (in kg) could be subsequently calculated.

The consequences of the flow velocity test for different incidence angles have not been determined because the test involves two phenomena that produce contrary effects from a frequency point of view. From one side, the damping is increased with the velocity, which should decrease the natural frequencies of the structure. On the other side, the forces that load the profile can increase its stiffness (bending and torsion) and also increase its natural frequencies. If the pressure distribution were known by means of pressure transducers located onboard, these values could be integrated, and the forces on the profile would be obtained. Structural theory would allow us to calculate the different stiffnesses (transverse and torsional), and hence the natural frequency variations. Moreover, an accurate pressure distribution could assist in proper validation of a future CFD simulation under cavitation conditions.

The basic experimental work presented in this thesis on cavitation should be complemented with an effective numerical model. A more detailed model could be validated with the results presented in this document. A two-way coupled numerical simulation would allow us to approach the problem from an overall perspective. The procedure would first validate the cavitation simulation to obtain reliable loads on the structure. Next, these loads would be transferred to the mechanics module, which would calculate the nodal displacements. Such structural displacements would be sent to the CFD tool to recalculate the flow field and restart the process once again, until a solution is found by convergence. This numerical model could be highly useful when designing a structure that may suffer from cavitation.

The effects of the gap on the natural frequencies of the hydrofoil are measurable both under still and flowing water conditions. Problems may arise when the cavitation takes place within the gap. Under these circumstances, the increase of the added mass that the presence of the wall produces is no longer valid, and the slope of the C_M-EM is expected to change. Because the presence of cavitation within the gap is difficult to detect and measure, an analogous study is proposed with a 2D hydrofoil clamped on both sides of the cavitation tunnel to avoid these problems.

XIII.II- Future work proposal

One of the main objectives of the present work was to develop an excitation and sensing system which could be used onboard and to validate an experimental procedure that allow us identifying the natural frequencies of a structure under different flow conditions-cavitation included-. Since the system performed reliably, the extrapolation to more complex structures seems logical. Therefore, the use of PZT technology on a whole machine or on a more complex system appears as the next step forward in this research line.

Additionally, with the obtained results, a direct extrapolation is proposed that could be of paramount interest for propeller or pump designers. If we expect a structure to suffer from sheet cavitation and seek to predict any potential resonance problems, we may need to identify these new natural frequencies. Therefore, taking the mode shapes of the designed structure as a starting point (obtained experimentally or by means of a FEM tool) and using a CFD simulation of the cavity (which could solve the composition in terms of void ratio), we could compute the EM. Once the EM is calculated, the new natural frequencies of the structure could be predicted using the relationship obtained from the current results using C_M.

APPENDIX A

Cantilever beam

Since the main focus of the present work is on 2D hydrofoils clamped on one side, it is of special interest for us the analogy with the cantilever beam system. The simple geometry and well defined boundary conditions allow us to consider it as a continuous system and treat it analytically. For questions of space and because there are several concepts which lay beyond the scope of the present work, the interested reader could be referenced to Rao (2007) for a more detailed analysis. In Figure A.1 the typical geometry of a cantilever beam has been outlined.

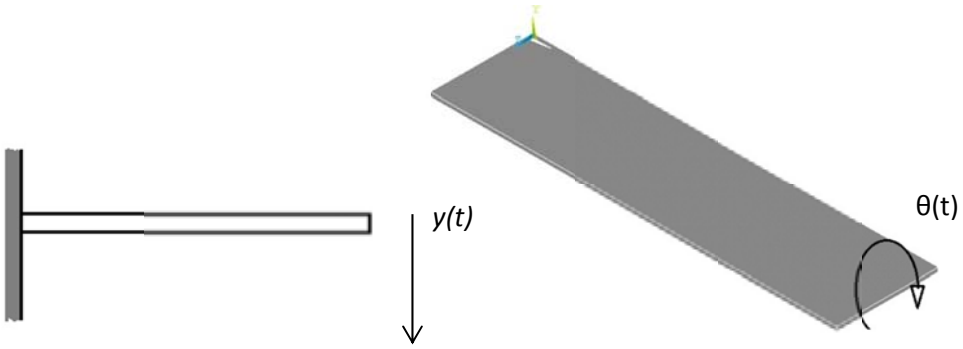

Figure A.1- Cantilever beams under transverse force (left) and torsional moment (right).

Considering the beam long and slender enough, we can derive the equations of motion according to the Euler-Bernouilly theory. The differential equation presented in equation (A.1) represents the transverse vibration of a beam.

$$\frac{\partial^2}{\partial x^2}\left(EI\frac{\partial^2 v}{\partial x^2}\right)+\rho A\frac{\partial^2 v}{\partial t^2}=f(x,t) \qquad (A.1)$$

Where E stands for the Young's modulus, I the area moment of inertia of cross section of the beam, A the cross-sectional area and ρ the mass density.

The boundary conditions, clamped at x=0 and free at x=l, are expressed as:

$$x = 0 \quad v(0,t) = 0 \qquad (A.2)$$

$$\frac{\partial v}{\partial x}(0,t) = 0 \qquad (A.3)$$

$$x = l \quad EI\frac{\partial^2 v}{\partial x^2}(l,t) = 0 \quad (A.4)$$

$$\frac{\partial}{\partial x}\left(EI\frac{\partial^2 v}{\partial x^2}\right)\Big|_{(l,t)} = 0 \quad (A.5)$$

In order to obtain the natural frequencies and mode shapes of a uniform beam it is necessary to use a modal analysis approach. Let us study the free vibration case expressed by equation (A.6).

$$f(x,t) = 0 \quad (A.6)$$

The partial differential equation is transformed to apply the method of separation of variables:

$$v(x,t) = V(x)T(t) \quad (A.7)$$

Where $V(x)$ and $T(t)$ are two generic single variable functions.

Substituting equations (A.6) and (A.7) into equation (A.1) we obtain:

$$\frac{EI}{\rho A}\frac{d^4V(x)}{V(x)dx^4} = -\frac{d^2T(t)}{T(t)dt^2} \qquad (A.8)$$

Both terms of equation (A.7) depend on independent variables (x and t), therefore to accomplish the equation, it results in:

$$\frac{EI}{\rho A}\frac{d^4V(x)}{V(x)dx^4} = -\frac{d^2T(t)}{T(t)dt^2} = a = \omega^2 \quad (A.9)$$

Where *a* is a positive constant. Equation (A.8) is, itself, two different equations:

$$\frac{EI}{\rho A}\frac{d^4V(x)}{dx^4} - \omega^2 V(x) = 0 \quad (A.10)$$

$$\frac{d^2T(t)}{dt^2} + \omega^2 T(t) = 0 \quad (A.11)$$

If we call:

$$\beta^4 = \frac{\omega^2}{\frac{EI}{\rho A}} \quad (A.12)$$

Assuming an exponential solution for equation (A.10) and substituting it, we can find the roots:

$$s_{1,2} = \pm\beta \qquad s_{3,4} = \pm i\beta \quad (A.13)$$

Therefore, the assumed exponential equation solution can now be expressed as:

$$V(x) = C_1 \cos\beta x + C_2 \sin\beta x + C_3 \cosh\beta x + C_4 \sinh\beta x \quad (A.14)$$

Where C_i are constants. As previously stated, V(x) are the mode shapes of vibration. The natural frequencies of the beam are obtained from:

$$\omega = \beta^2 \sqrt{\frac{EI}{\rho A}} \quad (A.15)$$

As can be seen, the previous analytical development is generic, if we want to study the cantilever beam system, we have to apply the boundary conditions to equation (A.14) and solve the mode shapes. Solving equation (A.15) we obtain the natural frequencies.

Equations from (A.2), (A.3), (A.4) to (A.5) can be translated to the new variables as:

$$V(0) = 0 \quad (A.16)$$

$$\frac{dV}{dx}(0) = 0 \quad (A.17)$$

$$\frac{d^2V}{dx^2}(l) = 0 \quad (A.18)$$

$$\frac{d^3V}{dx^3}(l) = 0 \quad (A.19)$$

Replacing equations (A.16) and (A.17) in equation (A.14) we obtain:

$$C_1 = C_3 = 0 \quad (A.20)$$

When replacing equations (A.18) and (A.19) in equation (A.14):

$$\cos\beta l \cosh\beta l = -1 \quad (A.21)$$

In order to obtain a solution for equation (A.21) it is convenient to take into account different aspects of the functions involved. cosh is always positive and greater than 1 with a hyperbolic growing trend. So for a sufficient large value of βl, $\cosh\beta l$ takes a really large value. In order to accomplish the equation (A.21) $\cos\beta l$ has to be small and negative, which in fact means:

$$\beta_n l \sim (2n-1)\frac{\pi}{2} \quad (A.22)$$

The higher the values of the integer *n*, the more accurate equation (A.22) will be. Therefore the natural frequencies of a cantilever beam are expressed by equations (A.15) and (A.22):

$$\omega_n = \left((2n-1)\frac{\pi}{2}\right)^2 \sqrt{\frac{EI}{\rho A L^4}} \quad (A.23)$$

And its corresponding mode shapes are given by:

$$V(x) = (\cos\beta_n x - \cosh\beta_n x) - \frac{\cos\beta_n l + \cosh\beta_n l}{\sin\beta_n l + \sinh\beta_n l}(\sin\beta_n x - \sinh\beta_n x) \qquad (A.24)$$

Similar approach can be used to study torsional vibrations.

Next section shows general equations of the natural frequencies of a cantilever beam with rectangular cross section.

Natural frequencies of a cantilever beam with rectangular cross section

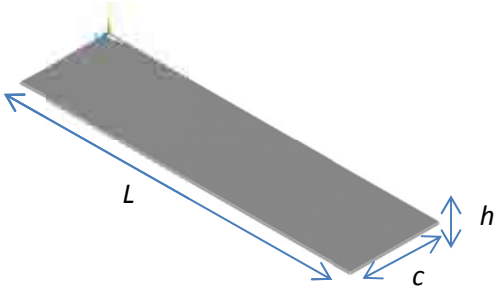

Figure A.2- Cantilever beam sketch with its typical dimensions.

	Bending modes		Torsion modes
Natural frequencies general form	$f_i = \frac{A_i^2}{2\pi L^2}\sqrt{\frac{EI}{\rho hc}}$		$f_i = \frac{A_i}{2\pi L}\sqrt{\frac{C \cdot E\frac{c^3h^3}{c^2+h^2}}{2\rho I_t(1+\nu)}}$
Parameters value	Mode 1	A_1=1.87510407	$A_i = \frac{(2i-1)\pi}{2}$
	Mode 2	A_2=4.69409113	

Table A.1- Theoretical expressions for bending and torsion natural frequencies of a cantilever beam.

Notation:

E=Young modulus

I= Moment of inertia of beam about neutral axis

I_t=Moment of inertia about the torsion axis

v= Poisson modulus

ρ= Beam's density

C= Cross section constant

c/h	**1**	**2**	**4**	∞
C	0.281	0.286	0.299	1/3

Table A.2- Cross section constant as a function of thickness-to-width ratio.

APPENDIX B

Signal processing background

For a more detailed theoretical background the reader is referenced to Bendat and Piersol (1971) and Oppenheim and Schafer (1989).

The Fourier transform ($\mathcal{F}$) of a time signal $x(t)$ is defined as:

$$\mathcal{F}[x(t)] = X(f) = \int_{-\infty}^{\infty} x(t)e^{-2\pi i f t}dt \quad (B.1)$$

where f stands for the oscillation frequency. One can think about Fourier transform as the computation of the frequency content of the initial time signal $x(t)$. An important disadvantage of such transform is that, as can be seen in (62), the integral calls for stationary or infinite (analog) signals which can be analyzed along the whole temporary range. Fourier transform of transient signals produces poor results as some frequency information is lost or hidden. Besides, in our tests, the signals acquired are transient and discrete (digital). The transient nature of the signals acquired can be overcome by using the Discrete Fourier Transform (DFT) which is defined as:

$$\mathcal{F}\{x[n]\} = X\left(e^{j\omega}\right) = \sum_{n=-\infty}^{\infty} x[n]e^{-j\omega n} \quad (B.2)$$

Or for a finite length sequence of length N:

$$\mathcal{F}\{x[n]\} = X\left(e^{j\omega}\right) = \sum_{n=0}^{N-1} x[n]e^{-j\omega n} \quad (B.3)$$

where $x[n]$ is the value of the discrete signal in its nth sample. Again, $X\left(e^{j\omega}\right)$ is an expression which determines how much of each frequency component is required to

recover $x[n]$. In general, as a complex function of frequency, the Fourier transform has a real part (magnitude) and an imaginary part (phase). There are several algorithms to compute the DFT, wide used ones due to their good computation efficiency are those based on the Fast Fourier Transform (FFT) (Cooley et al. 1967). These algorithms basically work factorizing the computation of DFT into smaller DFTs.

It is usually of great interest in signal analysis to evaluate the energy carried by a signal. In terms of energy, the Plancherel theorem (Plancherel 1910) states that the energy comprised in a function is kept constant both in time and frequency domain. This theorem is expressed as:

$$\int_{-\infty}^{\infty} |x(t)|^2 dt = \frac{1}{2\pi} \int_{-\infty}^{\infty} |X(\omega)|^2 d\omega \qquad (B.4)$$

There are also two related measures in this field which must be defined due to their great importance in this field i.e.: cross-correlation and autocorrelation. The former is a measured of similarity between two signals ($x[n]$, $y[n]$). It is expressed as:

$$(x * y)[n] = \sum_{m=-\infty}^{\infty} x^*[m] y[n+m] \qquad (B.5)$$

Where x^* is the complex conjugate of x. Similarly, the autocorrelation is defined as the cross-correlation of the same signal with itself.

As commented above, in order to answer the question "How much of the signal $x[n]$ is at a frequency f?" we need to compute the DFT. More precisely, we need to compute the DFT of the autocorrelation of x[n] which is called the Power Spectrum. In the same way, if one computes the DFT of the cross-correlation of two signals, a Cross Power Spectrum is obtained.

As mention above, the transient nature of some signals does not go really well with the DFT. Usually in these situations, there is a better approach than studying only the frequency domain. A Joint Time Frequency Analysis (JTFA) (Qian and Chen 1996) is particularly suitable when the transient nature of the studied signal provokes that not only the frequency content is interesting but also when each of those frequencies appears. JTFA studies the signal on both time and frequency domain at the same time. A very well-known JTFA is called Short Time Fourier Transform (STFT) where the DFT is applied systematically to short periods of the original signal which are delimited by a sliding window. The frequency content of each "time piece" of the signal is calculated and by repeating this procedure as the window is sweeping the total length of the signal, an estimation of the time-frequency content is obtained. STFT is expressed as:

$$STFT\ \langle x[n]\rangle = \sum_{n=-\infty}^{\infty} x[n]w[n-\tau]e^{-j\omega n} \qquad (B.6)$$

Where w is the applied window translated by τ. As STFT is based in DFT, it is assumed that the signal is stationary in each window. Therefore, one tends to decrease the size of the windows to increase the accuracy. Unfortunately, the resolution in both time and frequency has to obey an uncertainty principle.

APPENDIX C

Labview Routines

Labview is a graphical programming environment which is very flexible and allows users building routines in an easy and logical procedure. Clearly focused on several different fields, its built in purpose libraries such as Signal Processing, Sound and Vibration... helps the user dealing with signal treatment. Here, some examples of routines used during this work.

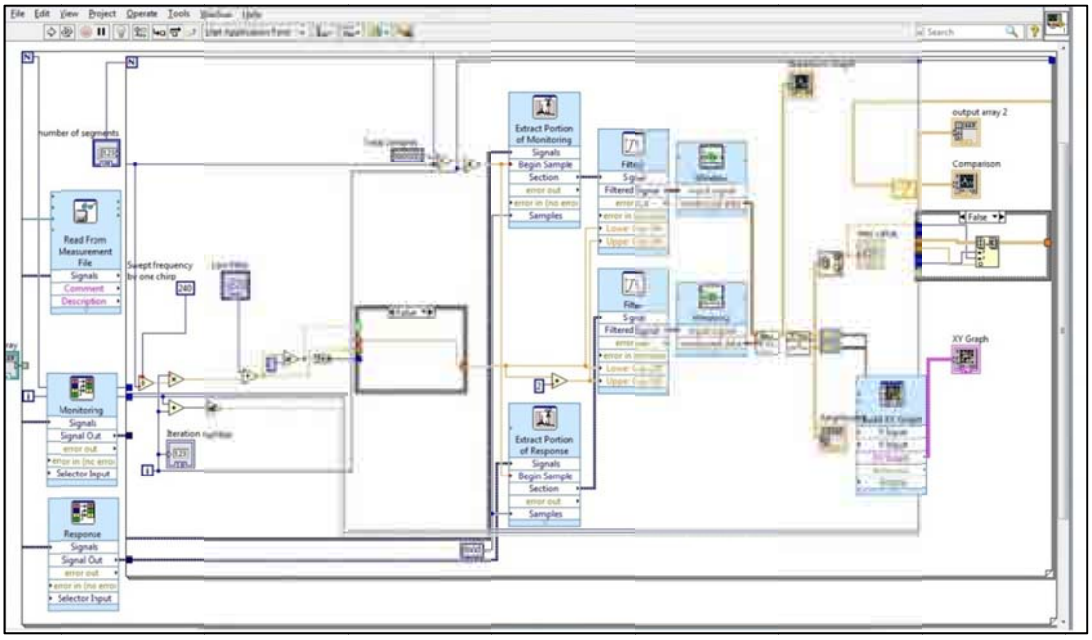

Figure C.1-Post processing example to extract an amplitude vs frequency plot and identify the resonant frequencies.

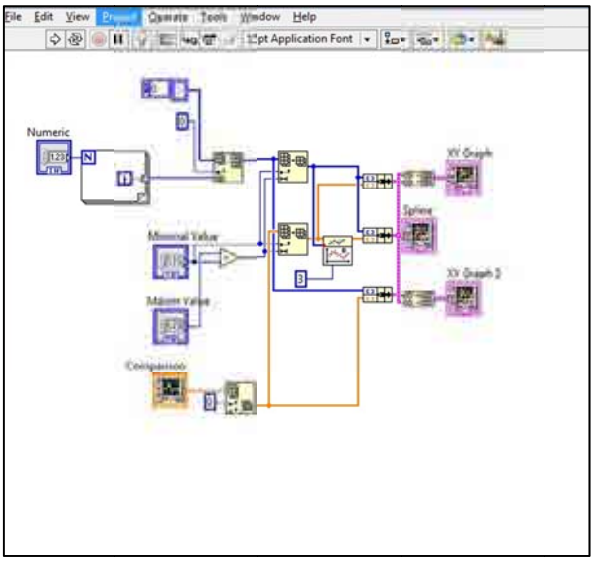

Figure C.2- Curve fitting by means of a spline.

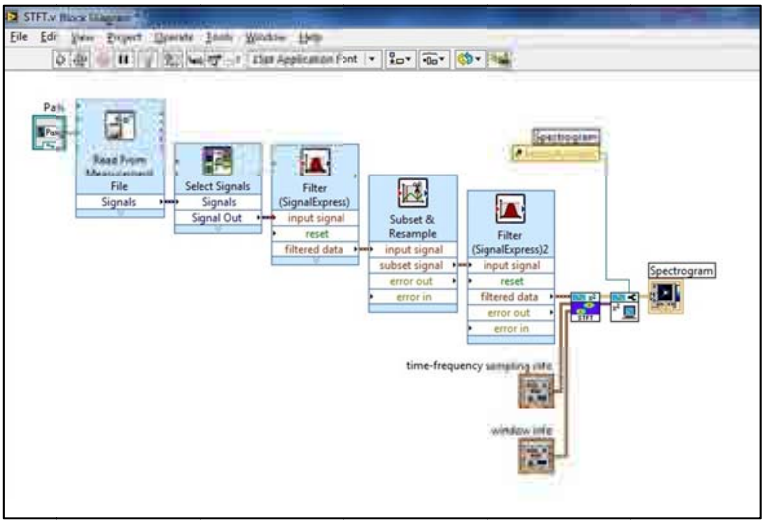

Figure C.3-Second post processing method: STFT Spectogram.

APPENDIX D

Mesh studies

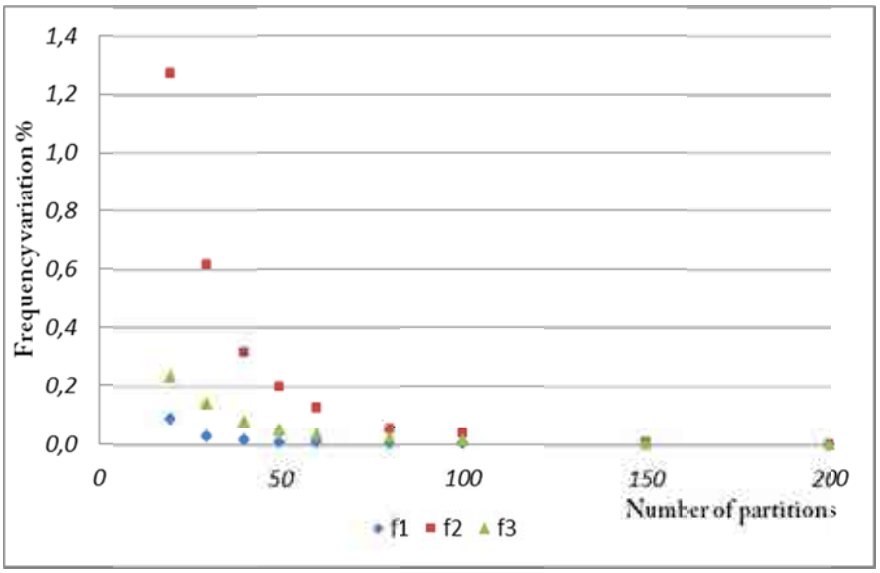

Figure D.1- Natural frequencies variation (%) against the number of partitions in the chord dimension.

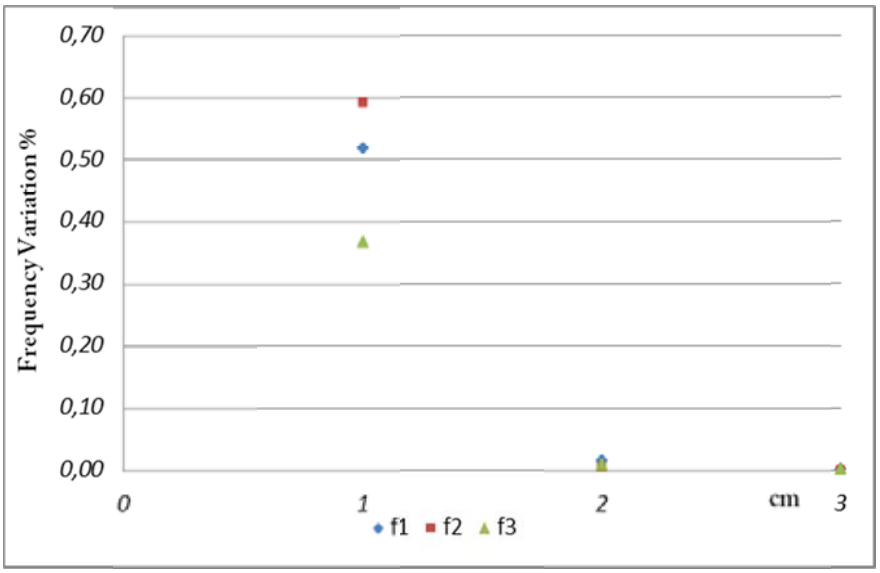

Figure D.2- Natural frequencies variation (%) against the horizontal profile wall distance (cm) when the hydrofoil is horizontally installed.

APPENDIX E

Numerical results

Effects of experimental conditions on mode shapes

Point number	Relative displacement magnitude			Phase (°)		
	f_1	f_2	f_3	f_1	f_2	f_3
1	0.96	1.00	0.03	22.5	-46.3	53.5
2	0.79	0.91	0.51	21.9	-46.8	120.7
3	0.57	0.79	0.88	22.3	-47.1	124.7
4	0.36	0.63	1.00	22.8	-46.8	125.2
5	0.18	0.43	0.80	24.2	-46.5	126.9
6	0.06	0.20	0.39	30.2	-45.8	130.7
7	0.97	0.50	0.10	22.2	-47.5	-42.7
8	0.78	0.46	0.37	21.8	-47.4	121.7
9	0.58	0.41	0.73	22.0	-47.1	123.4
10	0.39	0.33	0.84	22.4	-46.9	123.9
11	1.00	0.02	0.15	22.3	-59.2	-48.5
12	0.80	0.03	0.35	21.7	-54.8	121.2
13	0.59	0.03	0.68	22.3	-53.4	122.3
14	0.39	0.03	0.80	22.7	-57.7	121.4
15	0.22	0.02	0.65	23.7	-67.2	119.4
16	0.09	0.01	0.34	26.3	-67.9	117.6
17	0.96	0.47	0.11	20.3	133.4	-52.1
18	0.77	0.43	0.42	19.4	134.1	123.2
19	0.58	0.36	0.75	20.6	134.3	122.8
20	0.37	0.28	0.85	21.0	135.1	120.4
21	1.00	0.91	0.01	19.6	134.1	-103.9

22	0.80	0.82	0.53	20.0	134.0	125.5
23	0.54	0.71	0.91	21.1	133.9	125.0
24	0.35	0.55	1.00	21.7	133.9	124.7
25	0.19	0.37	0.79	20.5	133.9	124.3
26	0.06	0.18	0.40	22.3	133.4	126.6

Table E.1- Mode shape visualization: Relative displacement magnitude and phase under Air conditions.

Point number	Relative displacement magnitude			Phase (°)		
	f_1	f_2	f_3	f_1	f_2	f_3
1	0.81	0.96	0.48	146.6	-34.4	65.5
2	0.62	0.86	0.16	146.7	-36.5	-103.3
3	0.44	0.71	0.66	146.8	-37.9	-109.4
4	0.29	0.50	0.94	146.9	-41.6	-112.6
5	0.16	0.31	0.82	147.5	-46.3	-113.3
6	0.06	0.14	0.36	149.0	-47.6	-108.7
7	0.70	0.33	0.41	146.4	-41.5	69.4
8	0.55	0.26	0.14	146.5	-44.8	-112.6
9	0.40	0.22	0.57	146.6	-47.2	-113.2
10	0.26	0.17	0.83	146.7	-50.0	-115.0
11	0.99	0.02	0.39	146.5	156.5	73.1
12	0.76	0.01	0.18	146.5	171.8	-119.4
13	0.56	0.02	0.49	146.6	-178.7	-115.3
14	0.37	0.02	0.81	146.8	-129.9	-119.9
15	0.21	0.03	0.71	147.3	-155.3	-124.6
16	0.09	0.03	0.48	148.4	-166.4	-126.3
17	1.00	0.53	0.25	146.4	141.6	75.9
18	0.75	0.43	0.28	146.4	141.5	-117.7
19	0.58	0.35	0.54	146.5	142.1	-114.3

20	0.36	0.28	0.89	146.7	145.7	-121.8
21	0.96	1.00	0.15	146.3	145.3	76.8
22	0.75	0.82	0.22	146.3	143.9	-124.9
23	0.57	0.66	0.75	146.3	142.3	-115.0
24	0.35	0.51	1.00	146.3	141.5	-118.0
25	0.16	0.36	0.89	146.3	141.1	-115.4
26	0.07	0.17	0.48	146.3	140.4	-114.6

Table E.2- Mode shape visualization: Relative displacement magnitude and phase under Still water conditions.

Point number	**Relative displacement magnitude**			**Phase (º)**		
	f_1	f_2	f_3	f_1	f_2	f_3
1	1.00	1.00	0.26	67.2	100.8	18.2
2	0.99	0.88	0.28	67.8	102.0	-136.2
3	0.57	0.76	0.71	65.9	103.1	-146.3
4	0.38	0.62	0.92	65.0	104.0	-148.0
5	0.21	0.39	0.44	64.0	104.5	-147.7
6	0.07	0.00	0.44	60.9	-23.7	-146.2
7	0.97	0.34	0.29	67.8	147.1	26.1
8	0.80	0.41	0.22	67.7	122.9	-139.3
9	0.58	0.26	0.67	67.6	152.6	-148.4
10	0.40	0.22	0.86	67.2	155.2	-148.7
11	1.00	0.04	0.28	68.5	64.0	31.9
12	0.79	0.03	0.24	68.8	65.7	-153.0
13	0.59	0.03	0.63	68.7	62.3	-151.1
14	0.39	0.03	0.82	69.7	50.1	-151.8
15	0.22	0.05	0.37	72.3	58.6	-148.2
16	0.09	0.00	0.22	77.4	-22.9	-151.8
17	1.00	0.31	0.25	68.8	-22.6	37.2

18	0.79	0.29	0.32	69.1	-23.3	-156.4
19	0.59	0.24	0.72	69.6	-21.8	-151.8
20	0.37	0.22	0.90	71.7	-18.2	-153.1
21	0.98	0.78	0.14	69.7	-27.9	52.7
22	0.78	0.67	0.46	69.5	-47.7	-154.9
23	0.65	0.55	0.86	76.0	-35.5	-152.3
24	0.42	0.46	1.00	76.0	-41.1	-153.3
25	0.20	0.35	0.51	76.3	-38.7	-146.0
26	0.08	0.16	0.41	76.4	-38.7	-146.8

Table E.3- Mode shape visualization: Relative displacement magnitude and phase under Flowing conditions.

Point number	**Relative displacement magnitude**			**Phase (°)**		
	f_1	f_2	f_3	f_1	f_2	f_3
1	0.97	0.70	0.35	120.6	121.7	65.6
2	0.79	0.62	0.41	114.0	108.5	-41.5
3	0.53	0.54	1.00	126.8	120.1	-57.3
4	0.39	0.41	0.85	116.4	124.6	-51.6
5	0.21	0.29	0.92	121.1	128.5	-64.3
6	0.07	0.15	0.57	114.9	137.2	-58.5
7	0.94	0.35	0.32	125.7	97.1	99.6
8	0.74	0.33	0.29	121.1	97.4	-57.9
9	0.49	0.28	0.76	124.4	105.7	-65.1
10	0.39	0.23	0.71	127.6	105.1	-66.1
11	0.97	0.06	0.35	127.7	-8.2	122.8
12	0.73	0.06	0.25	115.1	9.6	-92.2
13	0.50	0.08	0.69	118.9	25.9	-80.6
14	0.38	0.10	0.64	125.6	35.0	-90.9
15	0.22	0.11	0.57	124.9	47.5	-103.8

16	0.07	0.08	0.35	132.0	43.5	-114.1
17	1.00	0.45	0.34	120.2	-66.9	136.3
18	0.68	0.40	0.30	119.0	-67.9	-108.8
19	0.53	0.32	0.60	119.9	-61.8	-91.3
20	0.38	0.24	0.64	117.0	-32.4	-99.1
21	0.99	1.00	0.33	120.0	-79.0	149.3
22	0.75	0.85	0.40	121.9	-82.2	-111.1
23	0.60	0.60	0.64	124.8	-72.5	-84.3
24	0.37	0.48	0.80	121.3	-71.3	-80.9
25	0.19	0.32	0.52	121.3	-72.7	-75.6
26	0.06	0.14	0.36	130.1	-66.2	-60.2

Table E.4- Mode shape visualization: Relative displacement magnitude and phase under Cavitating conditions.

Added mass of a cavitating hydrofoil

l/c	σ	CSR	C_{M1}	C_{M2}	C_{M3}
0.02	1.539	0.01	3.23	1.6	2.35
0.054	1.006	0.027		1.82	2.08
0.114	0.79	0.057		1.73	1.99
0.318	0.6	0.159	3.4	1.61	1.92
0.442	0.543	0.221	2.98	1.26	1.81
>1	0.264	0.598	0.18	0.23	0.31

Table E.5- C_M's for different cavity lengths for 1° incidence angle.

l/c	σ	*CSR*	C_{M1}	C_{M2}	C_{M3}
0.02	1.74	0.01	3.15	1.58	2.37
0.054	1.327	0.027	3.4	1.72	2.07
0.156	0.93	0.078	2.85	1.72	2.06

0.314	0.77	0.157	3.13	1.35	2.03
0.526	0.66	0.263	2.42	1.14	1.85
0.754	0.62	0.377	2.62	1	1.53
>1	0.272	0.597	0.32	0.34	0.42

Table E.6- C_M's for different cavity lengths for 2º incidence angle.

Lateral gap analysis

Gap (mm)	f_1 (Hz)	f_2 (Hz)	f_3 (Hz)	C_{M1}	C_{M2}	C_{M3}
0.12	268.4	1020.9	1640.9	0.00	0.00	0.00
0.22	270.2	1017.9	1633.1	-0.01	0.01	0.01
0.32	269.0	1019.1	1637.3	0.00	0.00	0.00
0.42	270.1	1019.7	1631.3	-0.01	0.00	0.01
0.62	270.2	1019.7	1633.1	-0.01	0.00	0.01
0.72	267.6	1020.9	1637.9	0.01	0.00	0.00
0.82	270.2	1020.3	1631.9	-0.01	0.00	0.01
1.12	269.0	1020.3	1633.1	0.00	0.00	0.01
2.12	267.8	1019.7	1632.5	0.00	0.00	0.01

Table E.7- Natural frequencies and C_M's for each gap distance in air conditions.

Gap (mm)	f_1 (Hz)	f_2 (Hz)	f_3 (Hz)	C_{M1}	C_{M2}	C_{M3}
0.12	123.9	617.9	867.0	3.69	1.73	2.58
0.22	124.5	619.7	868.2	3.65	1.71	2.57
0.32	125.1	620.3	875.4	3.60	1.71	2.51
0.42	125.6	620.9	879.6	3.57	1.70	2.48
0.62	126.3	622.7	878.3	3.52	1.69	2.49
0.72	126.8	624.5	884.3	3.48	1.67	2.44
0.82	127.4	624.5	886.1	3.44	1.67	2.43
1.12	128.1	625.6	884.3	3.39	1.66	2.44
2.12	130.4	629.2	892.1	3.24	1.63	2.38

Table E.8- Natural frequencies and C_M's for each gap distance in still water conditions.

Gap (mm)	f_1 (Hz)	f_2 (Hz)	f_3 (Hz)	C_{M1}	C_{M2}	C_{M3}
0.12	124.5	621.5	877.2	3.65	1.70	2.50
0.22	125.1	622.1	876.6	3.60	1.69	2.50
0.32	128.7	624.5	879.5	3.35	1.67	2.48
0.42	128.7	625.0	885.5	3.35	1.67	2.43
0.62	128.1	626.9	886.7	3.39	1.65	2.42

0.72	129.3	627.4	886.7	3.31	1.65	2.42
0.82	130.5	626.9	887.3	3.23	1.65	2.42
1.12	130.5	629.3	893.9	3.23	1.63	2.37
2.12	135.2	632.2	895.0	2.94	1.61	2.36

Table E.9- Natural frequencies and C_M's for each gap distance in 9 m/s conditions.

Gap (mm)	f_1 (Hz)	f_2 (Hz)	f_3 (Hz)	C_{M1}	C_{M2}	C_{M3}
0.12	122.2	621.5	911.1	3.76	1.63	2.20
0.22	123	622.8	912.9	3.70	1.62	2.18
0.32	123.7	623.9	914.4	3.65	1.61	2.17
0.42	124.3	624.9	915.8	3.60	1.61	2.16
0.62	125.4	626.5	918.2	3.52	1.59	2.15
0.72	125.9	627.2	919.2	3.49	1.59	2.14
0.82	126.3	627.9	920.1	3.46	1.58	2.13
1.12	127.5	629.6	922.6	3.38	1.57	2.12
2.12	130.3	633.4	928.2	3.19	1.54	2.08

Table E.10- Natural frequencies and C_M's for each gap distance in still water conditions obtained with Ansys.

Effects of pressure distribution on added mass

-1°	Flow velocity (m/s)							
	0	*5*	*7*	*10*	*12*	*15*	*18*	*20*
C_{M1}	3.66	3.36	3.20	3.01	3.20	3.20	3.52	2.87
C_{M2}	1.68	1.68	1.66	1.64	1.54	1.57	1.59	1.54
C_{M3}	2.32	2.31	2.29	2.31	2.29	2.29	2.20	2.22

Table E.11- Pressure distribution: C_M's for different flow velocities at 1° incidence angle.

-2°	Flow velocity (m/s)							
	0	*5*	*7*	*10*	*12*	*15*	*18*	*20*
C_{M1}	3.48	3.36	3.36	3.16	3.20	2.74	3.05	2.87
C_{M2}	1.68	1.66	1.66	1.64	1.56	1.51	1.59	1.57
C_{M3}	2.32	2.29	2.29	2.30	2.29	2.28	2.28	2.26

Table E.12- Pressure distribution: C_M's for different flow velocities at 2° incidence angle

-5°	Flow velocity (m/s)						
	0	*5*	*7*	*10*	*12*	*15*	*18*
C_{M1}	3.48	3.36	3.36	3.20	3.01	3.36	3.36
C_{M2}	1.68	1.68	1.68	1.63	1.59	1.55	1.54
C_{M3}	2.31	2.29	2.32	2.29	2.29	2.28	2.28

Table E.13- Pressure distribution: C_M's for different flow velocities at 5° incidence angle.

-7°	Flow velocity (m/s)					
	0	*5*	*7*	*10*	*12*	*15*
C_{M1}	3.48	3.36	3.36	3.36	3.52	3.52
C_{M2}	1.68	1.66	1.66	1.64	1.59	1.59
C_{M3}	2.32	2.32	2.32	2.29	2.29	2.33

Table E.14- Pressure distribution: C_M's for different flow velocities at 7° incidence angle.

	Flow velocity (m/s)				
-10°	*0*	*5*	*7*	*10*	*12*
C_{M1}	3.48	3.36	3.32	3.36	3.20
C_{M2}	1.68	1.68	1.66	1.64	1.62
C_{M3}	2.32	2.29	2.29	2.29	2.32

Table E.15- Pressure distribution: C_M's for different flow velocities at 10° incidence angle.

Partially submerged hydrofoil

Submergence (%)	f_1 (Hz)	f_2 (Hz)	f_3 (Hz)	C_{M1}	C_{M2}	C_{M3}
100	139	637.2	843.2	2.73	1.57	2.79
90	149.2	699.8	918.2	2.24	1.13	2.19
80	161.8	750.6	1028.1	1.75	0.85	1.55
70	172	776.4	1105.9	1.44	0.73	1.20
60	188.8	806.2	1190.9	1.02	0.60	0.90
50	200.2	806.2	1236.0	0.80	0.60	0.76
40	217.8	813.6	1320.9	0.52	0.57	0.54
30		844.8	1440.9		0.46	0.30
20	251.4	910.0	1550.4	0.14	0.26	0.12
10		981.8	1627.5		0.08	0.02

0		1021.4	1650.4		0.00	-0.01

Table E.16- Experimental natural frequencies and C_M's for each submergence level. TE orientation.

Submergence (%)	f_1 (Hz)	f_2 (Hz)	f_3 (Hz)	C_{M1}	C_{M2}	C_{M3}
100	138.4	639.6	868.1	2.76	1.55	2.57
90	148.6	715.4	933.2	2.26	1.04	2.09
80	161.2	768.6	1033.2	1.77	0.76	1.52
70	172	809.6	1118.5	1.44	0.59	1.15
60	185.2	824.2	1203.1	1.10	0.53	0.86
50	200.2	837.4	1270.9	0.80	0.49	0.67
40	218.4	836.4	1355.9	0.51	0.49	0.46
30		875.4	1475.4		0.36	0.24
20	251.4	922.0	1565.4	0.14	0.23	0.10
10		996.8	1645.8		0.05	-0.01
0		1022.0	1650.4		0.00	-0.01

Table E.17- Experimental natural frequencies and C_M's for each submergence level. LE orientation.

Submergence (%)	f_1 (Hz)	f_2 (Hz)	f_3 (Hz)	C_{M1}	C_{M2}	C_{M3}
100	138.1	650.2	963.5	2.73	1.41	1.86
90	147.8	705	1013.4	2.26	1.05	1.58
80	159.3	750.8	1069.9	1.80	0.80	1.32
70	172.6	780.2	1130.5	1.39	0.67	1.08
60	187.3	794.6	1193.7	1.03	0.61	0.86
50	203.5	802.3	1263.8	0.72	0.58	0.66
40	219.6	813.4	1339.3	0.47	0.54	0.48
30	237.3	840.7	1433.6	0.26	0.44	0.29
20	252.3	891.8	1526.3	0.12	0.28	0.14
10	263.1	966.6	1602.1	0.03	0.09	0.03
0	266.6	1007.5	1628.2	0.00	0.00	0.00

Table E.18-Natural frequencies and C_M's for each submergence level obtained by Ansys. TE orientation.

Submergence (%)	f_1 (Hz)	f_2 (Hz)	f_3 (Hz)	C_{M1}	C_{M2}	C_{M3}
100	138	654.7	963.9	2.73	1.37	1.86
90	147.3	713.6	1013.1	2.28	1.00	1.58

80	159.3	769.9	1074.2	1.80	0.72	1.30
70	172.3	804.9	1137.1	1.40	0.57	1.05
60	187.3	822.5	1205.4	1.03	0.50	0.83
50	202.7	829.9	1274.9	0.73	0.48	0.63
40	220	839.2	1357.3	0.47	0.44	0.44
30	237.1	861.7	1447	0.27	0.37	0.27
20	252.3	906.8	1535.3	0.12	0.24	0.13
10	262.7	968.7	1601.5	0.03	0.08	0.03
0	266.7	1008.5	1628.7	0.00	0.00	0.00

Table E.19-Natural frequencies and C_M's for each submergence level obtained by Ansys. LE orientation.

REFERENCES

[1] Aeschlimann, V., Barre, S., Legoupil, S., 2011. X-ray attenuation measurements in a cavitating mixing layer for instantaneous two-dimensional void ratio determination. Physics of Fluids 23.

[2] Amabili, M., 1996. Free vibration of partially filled, horizontal cylindrical shell. Journal of Sound and Vibration 191, 757-780.

[3] Amromin, E., Hansberger, J., Wang, H., Wosnik, M., Arndt, R.E.A., 2003. Investigation of a low-drag, partially cavitating hydrofoil. Fifth International Symposium on Cavitation, Osaka.

[4] Amromin, E., Kovinskaya, S., 2000. Vibration of cavitating elastic wing in a periodically perturbed flow: excitation of subharmonics. Journal of Fluids and Structures 14, 735-751.

[5] Ausoni, Ph., Farhat, M., Escaler, X., Egusquiza, E., Avellan, F., 2007, Cavitation influence on von Kármán vortex shedding and induced hydrofoil vibrations. Journal of Fluids Engineering, Volume 129, Issue 8, 966 (8 pages).

[6] Avellan, F., Henry, P., Ryhming, I.L., 1987. A new high speed cavitation tunnel. ASME Winter Annual Meeting, Boston 57, 49-60.

[7] Axisa, F., Antunes, J., 2007. Modelling of mechanical systems. Volume 3, Fluid-structure interaction. London, Kogan Page Science.

[8] Benaouicha, M., Astolfi, J.A., 2012. Analysis of added mass in cavitating flow. Journal of Fluids and Structures 31, 30-48.

[9] Bendat, J., Piersol, A,. 1971. Random data: Analysis and measurement procedures. Wiley-Interscience, John Wiley,

[10] Blevins, R.D.,1979. Formulas for natural frequency and mode shape. Krieger, Malabar.

[11] Brennen, C.E., 1982. A review of added mass and fluid inertial forces. A review of added mass and fluid inertial forces. Naval Civil Engineering Laboratory.

[12] Brennen, C.E., 1995. Cavitation and Bubble Dynamics. Oxford University Press.

[13] Bukaian, A., 1990. Natural frequencies of beams under tensile axial loads. Journal of Sound and Vibration 142, 481-498.

[14] Chung, J.S., 1994. Added Mass and Damping on an Oscillating Surface-Piercing Circular Column with a Circular Footing. International Journal of Offshore and Polar Engineering, Vol 4.

[15] Conca, C., Osses, A., Planchard, J., 1997. Added mass and damping in fluid-structure interaction. Computer Methods in Applied Mechanics and Engineering 146, 387-405.

[16] Cooley, J.W., Lewis, P.A.W., Welch, P.D., 1967. Historical Notes on the Fast Fourier Transform. IEEE Trans. Audio Electroacoustics, Vol AU-15, pp 76-79.

[17] Coutier-Delgosha, O., Devillers, J.F., Pichon, T., Vabre, A., Woo, R., and Legoupil, S., 2006. Internal structure and dynamics of sheet cavitation. Physics of Fluids, 18: 017103.

[18] Den Hartog, J.P., 1985. Mechanical Vibrations. Dover

[19] Dopazo García, C., 2008. ¿Cavitar o no cavitar? La inevitable ubicuidad de las burbujas. Real Academia de Ingeniería. Madrid.

[20] Ducoin, A., Astolfi, J.A., Gobert, M.L., 2010, An experimental study of boundary-layer transition induced vibrations on a hydrofoil, FEDSM-ICNM2010, Montreal.

[21] Ducoin, A., Young, Y.L., Sigrist, J.F., 2010. Hydroelastic responses of a flexible hydrofoil in turbulent, cavitating flow. FEDSM-ICNM2010, Montreal.

[22] Ducoin, A., Astolfi, J.A., Sigrist, J.F., 2012. An experimental analysis of fluid structure interaction on a flexible hydrofoil in various flow regimes including cavitating flow. European Journal of Mechanics B/Fluids, 36, 63-74.

[23] Escaler, X., Farhat, M., Egusquiza, E., Avellan, F., 2007. Dynamics and Intensity of Erosive Partial Cavitation. Journal of Fluids and Structures 129, 886-893.

[24] Fine, N.E, Uhlman, J. S. and Kring, D. C., 2001. Calculation of the Added Mass and Damping Forces on Supercavitating Bodies. CAV 2001: Fourth International Symposium on Cavitation, June 20-23, 2001, California Institute of Technology, Pasadena, CA USA.

[25] Franc, J.P, Michel, J.M., 2004. Fundamentals of cavitation. Kluwer Academic Publishers, Dordrecht.

[26] Frank, W., 1967. Oscillation of cylinders in or below the free surface of deep fluids. Naval Ship Research and Development Center, Report 2375.

[27] Gupta, K.K., Meek, J.L., 1996. A brief history of the beginning of the finite element method. International Journal for Numerical Methods in Engineering, Vol 39, pp 3761-3774.

[28] Ishii, M., 1975. Thermo-Fluid Dynamic Theory of Two-Phase Flow. Eyrolles, Paris.

[29] Jeffrey, D.J., 1973. Conduction through a random suspension of spheres. Proc. Roy. Soc. A 335, 355.

[30] Kaplan, P., and Kotik, J., 1963. Report on a seminar on the hydrodynamic theory associated with ship motion in waves. Office of Naval Research, Washington.

[31] Kennard, E.H., 1967. Irrotational flow of frictionless fluids, mostly of invariable density. David Taylor Model Basin, Washington. Report 2299.

[32] Kimber, M., Lonergan, R., Garimella, S.V., 2009. Experimental study of aerodynamic damping in arrays of vibrating cantilevers. Journal of Fluids and Structures 25, 1334-1347.

[33] Kirchhoff, G., 1869. Ueber die Bewegung eines Rotationskörpers in einer Flüssigkeit. Journal für die reine und angewandte Mathematik.

[34] Knapp, R.T., Daily, J.W., Hammit, F.G., 1970. Cavitation. McGraw-Hill, New York.

[35] Kramer, M.R., Liu, Z., Young, Y.L., 2013. Free vibration of cantilevered composite plates in air and in water. Composites Structures 95, pp. 254-263.

[36] Lamb, H., 1945. Hydrodynamics. Dover publications. New York.

[37] Liang, Q.W, Rodriguez, C.G, Egusquiza, E., Escaler, X., Farhat, M., Avellan, F., 2007, Numerical simulation of fluid added mass effect on a Francis turbine runner. Computer & Fluids 36, 1106-1118.

[38] Lindholm, U.S., Kana, D.D., Chu, W.-C., Abramson, H.N., 1965. Elastic vibration characteristics of cantilever plates in water. Journal of Ship Research 9, 11-22.

[39] Milne-Thomson, L.M., 1968. Theoretical Hydrodynamics, 5th ed. Dover, New York, pp. 515–541.

[40] Moliner, P.R., 1995. Vibraciones. Barcelona, CPDA.

[41] Motley, M.R., Matthew, R.K., Young, Y.L., 2013. Free surface and solid boundary effects on the free vibration of cantilevered composites plates. Composite structures 96, pp. 365-375.

[42] Moussou, P., 2005. A kinematic method for the computation of the natural modes of Fluid-Structure Interaction Systems. Journal of Fluids and Structures 20, 643-658.

[43] Münch, C., Ausoni, P., Braun, O., Farhat, M., Avellan, F., 2010. Fluid-structure coupling for an oscillating hydrofoil. Journal of Fluids and Structures 26, 1018-1033.

[44] Ogilvie, T.F., 1964. Recent progress toward the understanding and prediction of ship motions. 5th Symp. Naval Hydrodynamics, Bergen, Norway.

[45] Olofsson, N., Force and flow characteristics of a partially submerged propeller, Ph.D. Thesis, Department of Naval Architecture and Ocean Engineering, Chalmers University of Technology, Gothenburg, Sweden, 1996

[46] Oppenheim, A.V., Schafer, R.W., 1989. Discrete-Time Signal Processing. Englewood Cliffs : Prentice-Hall International.

[47] Parker, R.G., Mote JR, C.D., 1991. Tuning of the natural frequency spectrum of a circular plate by in-plane stress. Journal of Sound and Vibration 145, 95-110.

[48] Patton, K.T., 1965. Table of hydrodynamic mass factors for translational motion. ASME Paper, 65-WA/UNT-2.

[49] Plancherel, M.,1910. Contribution à l'étude de la représentation d'une fonction arbitraire par les intégrales définies", Rendiconti del Circolo Matematico di Palermo 30, pp 289–335.

[50] Porter, W.R., 1960. "Pressure Distributions, Added-Mass, and Damping Coefficients for Cylinders Oscillating in a Free Surface", University of California, , Series No. 82, Issue No. 16.

[51] Qian S., Chen D., 1996. Joint time-frequency analysis: Methods and applications. Prentice Hall

[52]Ragazzo, C.G., 2002. Dynamics of many bodies in a liquid: Added-mass tensor of compounded bodies and systems with a fast oscillating body. Phys. Fluids 14, 1590.

[53] Rao, S.S., 2007. Vibration of continuous systems. John Wiley & Sons, New Jersey.

[54] Reese, M.C. , 2010. Vibration and damping of hydrofoils in uniform flow, Master Thesis,Pennsylvania State University.

[55] Rodriguez, C.G., Egusquiza, E., Escaler, X., Liang, Q.W., Avellan, F., 2006, Experimental investigation of added mass effects on a Francis turbine runner in still water. Journal of Fluids and Structures 22, pp. 699-712.

[56] Salvesen,N., Tuck, E. O., and Faltinsen, O., 1970. Ship motions and sea loads. Trans. SNAME, Vol. 78 pp. 250-287

[57] Schiller, F.C., 1971. Wave Forces on a Submerged Horizontal Cylinder. M.S Thesis, Naval Postgraduate School, Monterey, California.

[58] Seeley, C., Coutu, A., Monette, C., Nennemann, B., Marmont, H., 2012. Characterization of hydrofoil damping due to fluid-structure interaction using piezocomposites actuators. Smart Materials and Structures 21.

[59] Sewall, J.L., Miserentino, R., Pappa, R.S., 1983. Vibration studies of a lightweight three-sided membrane suitable for space application. NASA Technical Paper 2095.

[60] Stutz, B., Legoupil, S., 2003. X-ray measurements within unsteady cavitation. Experiments in Fluids, 35:130-138.

[61] Stutz, B., Reboud J.-L., 1997. Two-phase flow structure of sheet cavitation. Physics of Fluids, Vol. 9, No. 12.

[62] Ursell, F., 1949. On the heaving motion of a circular cylinder on the surface of a fluid. Quart. J. Mechanics and Applied Math., 2, p. 218-231.

[63] Ursell, F., 1949. On the rolling motion of cylinders in the surface of a fluid. Quart. J. Mechanics and Applied Math., 2, p. 335-353.

[64] Ursell, F., 1953. Short surface waves due to an oscillating immersed body. Proceedings of the Royal Society of London. Series A. Mathematical and Physical Sciences 220 (1140), 90-103.

[65] Van Wijngaarden, L., 1976. Hydrodynamic interaction between gas bubbles in liquid. J. Fluid Mech.Vol 77, part 1, 27-44.

[66] White, F.M., 1994. Fluid mechanics. McGraw-Hill

[67] Yadykin, Y., Tenetov, V., Levin, D., 2003. The added mass of a flexible plate oscillating in a fluid. Journal of fluids and structures 17, 115-123.

[68] Yamamoto, T., Nath, J.H., Slotta, L.S.,1973. Yet Another Report on Cylinder Drag or Wave Forces on Horizontal Cylinders. Bulletin 47, Engineering Experiment Station, Oregon State University.

[69]Yang, F.-L., 2010. A formula for the wall-amplified added mass coefficient for a solid sphere in normal approach to a wall and its application for such motion at low Reynolds number. Physics of Fluids. Volume 22, Issue 12.

[70] Young, Y.L., 2007. Time-dependent hydroelastic analysis of cavitating propulsors. Journal of Fluids and Structures 23, 269-295.

[71] Young, Y.L. and Savander, B.R., 2011. Numerical Analysis of Large-Scale Surface-Piercing Propellers, Ocean Engineering, 38: 1368-1381.

[72] Zienkiewicz, O.C., Taylor, R.L., 2000. The Finite Element Method. Volume I: The Basis. Butterworth-Heinemann.

[73] Zobeiri, A., 2012. Effect of hydrofoil trailing edge geometry on the wake dynamics. PHD Thesis, École Polytechnique Fédérale de Lausanne.

List of Publications

Conference Papers

de la Torre, O., Escaler,X.,Egusquiza, E., Farhat, M.,2012. "The Effect of Cavitation on the Natural Frequencies of a Hydrofoil". 8th International Symposium on Cavitation, Singapore.

ABSTRACT

The objective of the present paper is to show the effect of cavitation on the natural frequencies of a NACA0009 hydrofoil. The existence of large portions of the hydrofoil surface covered by vapor is expected to reduce the added mass effects of the surrounding flowing water. For that, a specific excitation and measuring system based on piezoelectric patches has been developed and validated. With this experimental setup, the three first natural frequencies of an aluminum NACA0009 truncated hydrofoil have been determined in various conditions. The hydrofoil has been tested with partial cavitation and with supercavitation at 14 m/s and two incidence angles of 1° and 2°. Analogous tests have been carried out with the hydrofoil in air and surrounded by still water. The comparison of all the results has confirmed the significant role that cavitation plays in the modal response of the hydrofoil.

Journal Articles

de la Torre, O., Escaler,X.,Egusquiza, E., Farhat, M.,2012."Experimental investigation of added mass effects on a hydrofoil under cavitation conditions". Journal of Fluids and Structures. Accepted for publication.

ABSTRACT

The influence of leading edge sheet cavitation and supercavitation on the added mass effects experienced by a 2-D NACA0009 truncated hydrofoil has been experimentally

investigated in a hydrodynamic tunnel. A non-intrusive excitation and measuring system based on piezoelectric patches mounted on the hydrofoil surface was used to determine the natural frequencies of the fluid-structure system. The appropriate hydrodynamic conditions were selected to generate a range of stable partial cavities of various sizes and also to minimize the effects of other sources of flow noise and vibrations. The main tests were performed for different sigma values under a constant flow velocity of 14 m/s and for incidence angles of both 1° and 2°. Additionally, a series of experiments in which the hydrofoil was submerged in air, partially and completely submerged in still water and without cavitation at 7 and 14 m/s were also performed. The maximum added mass effect occurs with still water. When cavitation appears, the added mass decreases because the cavity length is increased, and the added mass is at a minimum for supercavitation. A linear correlation is found between the added mass coefficients and the entrained mass that accounts for the mean density of the cavity, its dimensions and its location relative to the specific mode shape deformation.